Multi-Photon Spectroscopic Studies of Molecule/Metal Interfaces and Graphene

Sung Young Hong

Submitted in partial fulfillment of the
requirements for the degree of
Doctor of Philosophy
in the Graduate School of Arts and Sciences

COLUMBIA UNIVERSITY
2014

ABSTRACT

Multi-Photon Spectroscopic Studies of Molecule/Metal Interfaces and Graphene

Sung Young Hong

This dissertation presents multi-photon spectroscopic studies on molecule/metal interfaces and graphene. Two different aspects of these ultrathin molecular or atomic materials were investigated: (1) the electronic structure of molecule/metal interfaces and (2) nonlinear optical properties of graphene.

For the case (1), two-photon photoemission (TPPE) using a femotosecond laser was employed to investigate occupied and unoccupied electronic states of molecule/metal interfaces. Here we selected two specific examples of interfaces, benzenethiols on Cu(111) and hexa-cata-hexabenzocoronene (HBC) on Cu(111), which are important model systems for an organic / electrode interface of organic semiconductor devices. Although the same copper substrate was used for all the experiments, the nature of interfaces was strongly affected by the interaction between molecular adlayers and metal substrate.

Our TPPE measurements on two benzenthiol species, thiophenol and p-fluorothiophenol, on Cu(111) focus on the role of adsorbates in shifting surface polarization and effecting surface electron confinement. As the coverage of each molecule increases, their photoemission-measured work functions exhibit nearly identical behavior up to 0.4-0.5 ML, at which point their behavior diverges; this behavior can be fit to an interfacial bond model for the surface dipole. In addition, our results show the emergence of an interfacial electronic state 0.1-0.2 eV below the Fermi

level. This electronic state is attributed to quantum-mechanical-confinement shifting of the Cu(111) surface state by the molecular adsorbates.

Another TPPE study of ours was carried out on an organic semiconductor, HBC, deposited on Cu(111). An increase of HBC coverage continuously shifts the vacuum level of the Cu substrate until a coverage of 2 ML is reached. In the same range of coverage, the Shockley state and the image potential states are quenched while new unoccupied states develop. The momentum- and polarization-resolved photoemission spectra reveal that the new states are originated from a Cu image state. Electron localization is discussed with respect to the structural evolution of HBC.

For the case (2), nonlinear optical scanning microscopy was designed to study third-harmonic generation (THG) from micron-scale graphene crystals on glass substrate. The polarization-, thickness-, and orientation- dependence of THG signals from the graphene were measured and compared to theoretical prediction using the nonlinear optical slab model of Bloembergen and Pershan. The results revealed in-plane isotropy and out-of-plane anisotropy of the THG signals and sub-quadratic dependence of the layer number. Due to the strong THG signal, background-free imaging of graphene crystal was carried out. This result implies the potential application of THG for imaging graphene on arbitrary substrates.

Table of Contents

List of Figures

Acknowledgement

During my PhD program, I have greatly benefited from many individual around me. Without their helps and supports, this dissertation would not have been finished.

Foremost, I would like to express my sincere gratitude to my advisor Prof. Richard Osgood Jr. who has supported me throughout my dissertation research with patience, enthusiasm and, encouragement. Under his guidance, I not only learned scientific knowledge and skills indispensable for my future career but also gain a positive and constructive attitude to persevere difficult problems. I was really fortunate to have him as my advisor.

I am deeply indebted to Prof. George Flynn who has served as a co-advisor. His generous support and encouragement was a great help to me. I would like to show my deep appreciation to Prof. Louis Brus who served as another thesis committee member. His insightful questions and comments in the 4th-year oral exam were invaluable to me. I also acknowledge my defense committee, Prof. David Reichman and Prof. Abhay Pasupathy.

In Osgood group, I have met many wonderful colleagues. Among them, I have owed a very important debt to Dr. Jerry I. Dadap who mentored me in all the research projects of mine. He helped me to build laser setups and gave me many suggestions when I analyzed the data. Also I deeply appreciate his proofreading for my dissertation. I am indebted to Dr. Denis Potapenko for helping me build a new sample holder and Nader for giving me his cobalt evaporator to be modified. I would like to thank to Figo (or Po-Chun Yeh) for his collaboration and dedication. I would like to thank Stan (or Hsu-Cheng Huang) for sharing his interests in science and other field. Also I would like to thank to other group members and vistors including Zhisheng Li or "Z-man" who was my delightful officemate, Wencan Jin, Alex Meng, Richard Grote, Jeffrey

Driscoll, Brian Souhan, Dr. Ophir Gaathon, Dr. Kevin Knox, Dr. Xiaoping Liu, Nick Choi, Ida Delač, Eugene Cho, Yang Lou, and Ilkyu Lee for many assistances and suggestions. Also I would like to express my special thanks to our lab administrator, Svitlana Samoilina.

I would like to express my appreciation to my collaborators. Prof. James Hone and Nick Petron for provided CVD-graphene samples and shared many valuable ideas. Also Prof. Colin Nuckolls and Jaeeun Yu provided their HBC compounds for TPPE experiments.

I would like to appreciate my former group members, Prof. Kenneth Eisenthal, Dr. Yi Rao, Dr. Eric McArthur, Dr. Mahamud Subir, Dr. Man Xu, Dr. Kalyanasis Sahu, Dr. Soohwan Sul, Dr. Louis Haber, Monica Semeraro, and Sheldon Kwok. Also I would like to express my special thanks to the program coordinator, Alix Lamia, for many assistances and Dr. Kwang-taeg Rim for many advices for UHV instrumentations.

I would like to thank to my friends, fellows, and relatives. In particular, I wish health and happiness to my cousin and her family.

I would like to express my deepest gratitude to my mother and brother. My mother have nurtured and cared me since I was born. Without her endless love and sacrifice, I would not be here now. My brother also have supported and encouraged me for a long time. I miss them so much.

Last, but not at the least, I would like to express my thanks and love to my family, my wife, Heeun, and our son, Lenny. They have inspired and invigorated me when I was tired and frustrated. My life is so much better because they are with me.

To my wife, our son, and Mom

Chapter 1

Introduction

Solid interfaces are defined as a few atomic or molecular layers forming at a boundary between two solid materials. The simplest interface is the solid-vacuum interface. In the vicinity of the surface, the electronic wave function is very different from the Bloch waves in the bulk materials because of the discontinuity and broken symmetry at the interface. There are electronic wave functions that extend from the bulk and decay to the vacuum side while some wave functions (surface states) are localized at the surface but propagate along the plane of the interface. The electronic structure of solid-solid interfaces is even more complex because of the participation of another solid material. Among the solid interfaces, the molecule/metal interface is of particular interest in this dissertation. In this particular type of interfaces, their interaction leads to many peculiar results including energy level alignment, surface state modification, and the broadening of molecular states, and the appearance of new states.

The electronic behavior of the molecule/metal interface is closely related to many technological advances. One example is heterogeneous catalytic reaction, where the elementary processes including adsorption, diffusion, desorption, and dissociation are involved in the electronic interaction between metal substrate and reactant molecules. Also the recent progress in organic optoelectronic devices has lead to considerable interests in organic/organic and organic/metal interfaces in the scientific community since typical organic devices consist of one or several organic materials sandwiched between two electrodes. The performance of devices relies on the charge transfer processes across the interfaces as well as transport processes through the bulk materials. The scattering and trapping of charges at interfaces can set the limit for the performance of devices, for instance, the operating voltage in organic light-emitting diode and conversion efficiency in organic solar cell. Precise and detailed account of interfacial electronic structure and dynamics can guide the design of organic semiconductor materials, choice of substrates, and condition control of fabrication processes.

Elucidation of electronic structure at surfaces and interfaces is a challenging task with conventional spectroscopic techniques adapted for bulk material studies. Since the signals of the bulk materials easily overwhelm those of the interface, surface/interface-sensitive spectroscopic techniques are required. Among several experimental techniques, two-photon photoemission (TPPE) combined with the ultrahigh vacuum (UHV) system has been particularly successful. As a low-energy electron spectroscopy, TPPE has a strong surface sensitivity. In addition, UHV technology enables the preparation of clean surface and the precise control of adsorbate thickness. In contrast to conventional photoemission techniques (ultraviolet photoemission and inverse photoemission), TPPE probes both occupied and unoccupied electronic states with high energy- and momentum-resolution. Finally, interfacial ultrafast dynamical processes can be tracked by the femtosecond pump-probe TPPE technique.

Graphene, a single sheet of sp2-bonded carbon atoms, is the first two-dimensional material to be discovered. Its extraordinary electronic structure, which is represented by the linear relation of mass and momentum near its K-point, results in its extremely high mobility and flat absorption band in visible wavelength. In addition to its remarkable electronic and optical properties, graphene has attracted considerable interest in its application to a nonlinear optics. Based on the its ultrabroad-band resonance, the large optical susceptibility of graphene has been predicted theoretically and proven in several experiments. Recent progress of graphene in nonlinear optical application includes mode-lock laser medium as a saturable absorber, broadband optical limiter, and four-wave mixing. Majority of applications of graphene as a nonlinear medium is based on its strong third-order nonlinear response.

This dissertation investigates the interfacial electronic structure of organic/metal interfaces and the third-order harmonic generation (THG) of graphene. This chapter (Chapter 1) serves on the introduction of the systems in interests. Chapter 2 provides the general background about 1) the electronic structure of bare metal surface and organic/metal interfaces and 2) nonlinear optics with emphasis on the third-harmonic process. Chapter 3 describes the experimental setups for TPPE and THG as well as the sample preparation. This chapter also includes some background of TPPE. Chapter 4 and 5 present the TPPE studies on the selected model systems of organic/metal interfaces: benzenethiols/Cu(111) and hexa-cata-hexabenzocoronene/Cu(111). Chapter 6 presents THG imaging of graphene. Chapter 5, 6, and 7 includes specific introduction and experimental methods for each research project as well as results and discussion. Chapter 7 presents the summary and future direction of the dissertation research.

Chapter 2

Background

2.1 Electronic Structure of Molecule/Metal Interfaces

2.1.1 Work Function of a Bare Metal Surface[1, 2]

Work function in metals corresponds to the difference of energy between the Fermi level and the vacuum level. It is also the minimum energy needed to remove an electron from the metal surface to the vacuum at 0 K. In contrast to the Fermi level, the vacuum level depends on the surface chosen. As shown in Figure 2.1, we can consider two vacuum levels: the one near the surface of a metal and another at the infinite distance from the metal. The vacuum level involved in photoemission measurement is the energy of electron at rest just outside of the solid.

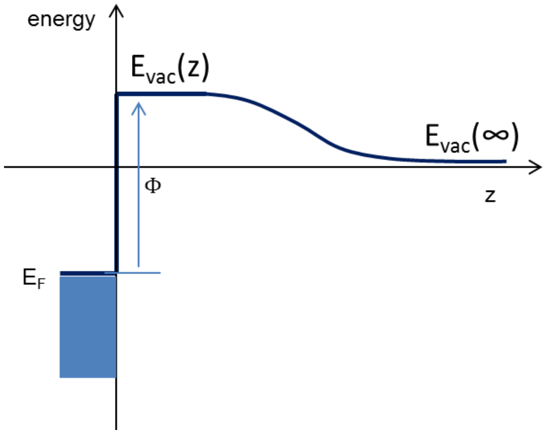

Figure 2.1 Schematic diagram for the vacuum levels at the surface (Evac (z)) and the infinite distance (Evac(∞))

The work function(Φ) of a metal depends on electrostatic potential barrier across the metal surface ($\Delta\phi$) and chemical potential of substrate materials ($\bar{\mu}$).

$$\Phi = \Delta\phi - \bar{\mu} \tag{2.1}$$

The surface potential is originated from electron “leak” or “spill-out” out into the vacuum from the metal. Jellium model was used to describe this tail of electron cloud of metal into the vacuum. Figure 2.2 shows that negative charge density from electrons changes smoothly across the surface while the positive charge density from nuclei drops like a step function. The difference in gradient of the two charge densities creates electron-density excess outside the surface and electron-density deficiency inside the surface. As a result, a surface dipole forms in an orientation toward the metal and the work function increases.

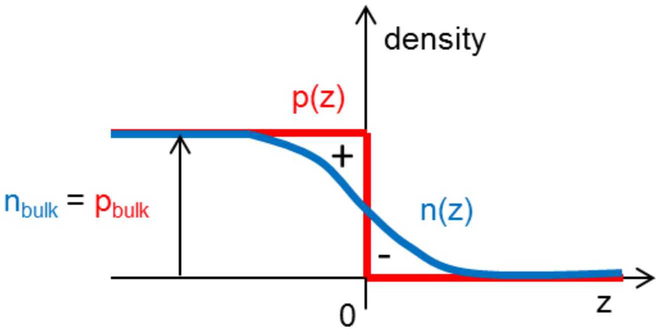

Figure 2.2 Charge distribution density around the metal surface

The smoothing effect of electron cloud is also found in the anisotropy of the work function[3]. The work function of densely-packed surface (i.e., Cu(111), Φ ~ 4.9 eV) of metal is higher than that of loosely-packed surface (i.e., Cu(100), Φ ~ 4.6 eV).

2.1.2 Molecule/Metal Interfaces and Interface Dipole Formation [3-5]

The adsorption of molecules on metal surfaces modifies their work function. These changes give rise to “interface dipole” (See Figure 2.3). There are several mechanisms of the interfacial dipole formation: push-back effect, charge transfer, chemical-bond formation, surface reconstructing, permanent molecular dipole, etc. In particular, “push-back” effect means that adsorbates push back the spill-out of surface electrons (see the previous section) to the metal side, reducing the surface dipole and work function. This effect is known as a prevailing mechanism for the lowered work function in many organic/metal interfaces if there is no charge transfer or chemical interaction at the interface.

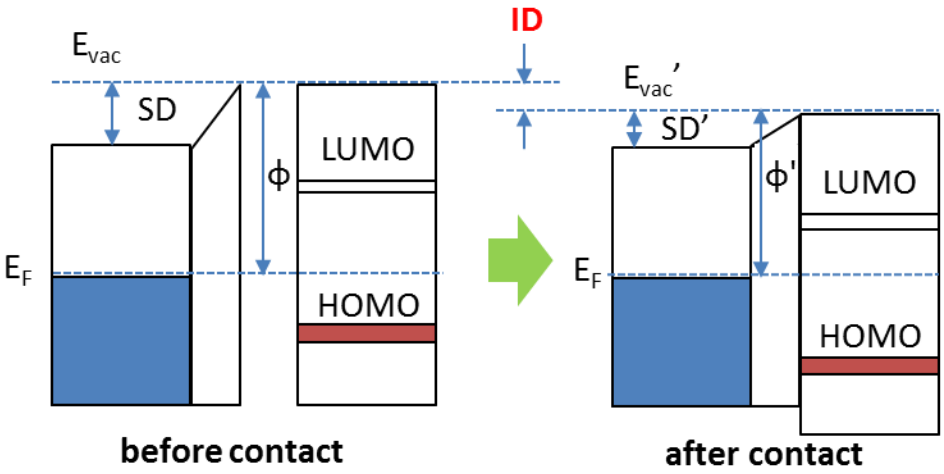

Figure 2.3 Energy level alignment at an organic/metal interface. ID is the interface dipole and SD and SD’ are surface dipole before and after the contact.

The origin of interface dipole is closely related to the strength of interaction between molecules and metal determines. Braun et al. classified five different cases: (1) physisorption without charge transfer (noble gas or hydrocarbon on clean metal surfaces), (2) physisorption with integer charge transfer (conjugated molecule on passivated metal surfaces), (3) weak chemisorption with partial charge transfer (conjugated molecules on non-reactive clean metal surfaces), (4) strong chemisorption with covalent bonding (molecules on reactive clean metal surfaces), (5) strong chemisorption with covalent bonding at a specific site of molecules and metal (molecules with intrinsic dipole and anchoring group on clean metal surfaces). This classification is a useful guide for understanding of interface energetics. Among the models, (3) and (5) are of interest in this dissertation.

For case (3), weakly hybridized molecule-metal system, the induced density of interface states (IDIS) model is employed. This model describes the alignment tendency of charge neutrality level (CNL) to the Fermi level of metal. The concept of CNL is closely related to Pauling's electronegativity of atom, $\frac{I+A}{2}$, where I is ionization energy and A is electron affinity. While the electronegativity is related to HOMO and LUMO only, CNL is determined by integrating the total induced density of states at the interface as shown in Figure 2.4. In the IDIS model, the direction of charge flow at the interface is determined by the sign of misalignment, CNL$-E_{Fi}$, where E_{Fi} is the initial Fermi level of the metal surface before contact. This charge transfer induces the screening potential and then this potential shifts the molecular level with regard to the Fermi level. This effect is incorporated in the IDIS model by the screening parameter S, which is between 0 and 1. A lower value of S (close to zero) indicates the Fermi level pinning (or strong organic-metal coupling) while a higher value of S (close to one) indicates the vacuum level alignment (or weak organic-metal coupling). The interface potential, Δ (or interface dipole) is determined by two terms: CNL$-E_{Fi}$ and S.

$$\Delta = (1 - S)(E_{Fi} - CNL) \tag{2.2}$$

The IDIS model itself does not include the push-back effect but its effect on this type of interfaces can be significant. There is a unified IDIS model incorporating the push-back effect.

$$\begin{aligned}\Delta &= eV_0^P + (1-S)(CNL - E_{Fi} - eV_0^P) \\ &= (1-S)(CNL - E_{Fi}) + SeV_0^P\end{aligned} \tag{2.3}$$

where V_0^P is the potential shift due to the push-back effect. Equation 2-3 indicates that $\Delta = eV_0^P$ if S=1 (no screening) while $\Delta = CNL - E_{Fi}eV_0^P$ if S=0

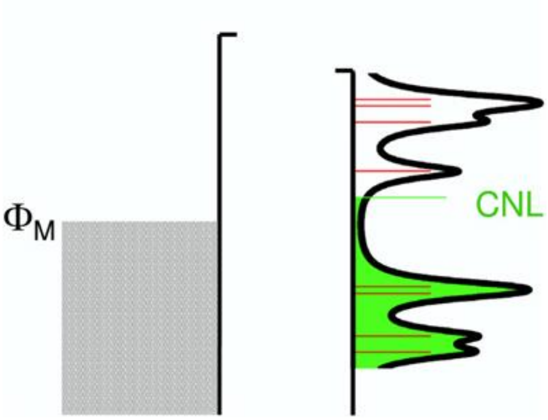

Figure 2.4 Schematic illustration of charge neutrality level at the organic/metal interface reproduced from [6]

A representative example of (5) is a self-assembled monolayer (SAM) with an anchoring group on metal substrate. Recently a series of DFT studies analyzed the energetics of SAM interfaces in details and revealed the nature of charge rearrangement at the SAM/metal interface. The total change of work function ($\Delta\Phi_{\mathrm{SAM/sub}}$) in this interface can be approximated by the summation of the potentials created by the molecular dipole and bond dipole

$$\Delta\Phi_{\mathrm{SAM/sub}} = \Delta V_{vac} + \mathrm{BD} \tag{2.4}$$

where ΔV_{vac} and BD are an additive potential step across SAM/vacuum and bond dipole, respectively. The main contributions of bond dipole are conceptually (1) push-back effect and (2) charge rearrangement due to the formation of chemical bond between anchoring group and metal substrate. The DFT simulation gives quantitative picture of electrostatics in SAM/metal interface. In case of thiol-SAM/metal interface, the total rearrangement of charge density, $\Delta\rho$, is

$$\Delta\rho = \rho - \left((\rho_{mol} - \rho_H) + \rho_{sub}\right) \tag{2.5}$$

where ρ is the final charge density of thiol SAM/metal and ρ_{mol}, ρ_H, and ρ_{sub} are the charge density of thiol molecule, H atom, and metal substrate, respectively. The interfacial potential can be obtained by integrating the charge density along the surface normal (z).

$$\frac{d^2V(z)}{d^2z} = -\frac{1}{\epsilon_0}\rho(z) \tag{2.6}$$

The DFT studies of thiol-SAM/Au(111) interfaces revealed that there is alternating accumulation and depletion of charge density along the thiol-Au bond axis. This oscillation of charge density is equivalent to a series of dipoles aligned in the same direction so that a large potential drop (~1.2 eV) is created.

Another potential step, ΔV_{vac}, at the SAM/vacuum interface is created by the permanent molecular dipole. Note that the projection of dipole along the surface normal contributes the potential step

$$\Delta V_{vac} \simeq \frac{e\mu_z}{\epsilon_0 A} \tag{2.7}$$

where μ_z is the projected molecular dipole moment, A is the unit cell surface area. Since molecules are polarizable, the depolarization effect should be taken into account for high density dipolar SAMs. In this case, an effective dielectric constant can be inserted in the denominator of the Equation 2-7.

2.1.3 Shockley Surface State and Its Adsorbate-Induced Modification[7-10]

Electronic states of an infinite periodic solid are described by three-dimensional Bloch states, which have certain translational-symmetry based on their structures. For a real solid, their symmetries are broken due to the finite sizes of materials. The broken symmetry causes the formation of new electronic states confined only at the surface region; Their wave function decay exponentially into both bulk of the solid and vacuum region. There are two types of surface state. The surface states derived from the nearly-free electron model is called the "Shockley" surface state while another type of surface states derived from the tightly-bound electron model is "Tamm" state. In this section, we narrow our interests in the Shockley surface states of metals.

The wave function of Shockley states can be derived from Schrodinger equation of semi-infinite periodic solid model. The details of the derivation are introduced in the reference. The basic strategy is to separately find wave functions in each crystal and vacuum side and then find well-behaved wave function in both sides using the boundary condition. For the crystal side, the one-dimensional nearly-free electron ("two-band") approximation is used. In this model, the crystal potential is described as a simple cosine potential,

$$V(z) = 2V_g \cos\frac{2\pi}{a}z \tag{2.8}$$

where a is the lattice constant and V_g is the amplitude of oscillating crystal potential. Conventionally, the sign of V_g is set to negative and the origin z = 0 is between ion cores. This case is called "Shockley-inverted gap" because the s state at an ion core (cosine function) is energetically higher than the p state between ion cores (sine function). After some calculations, the wave functions in the crystal side has a form

$$\psi = Ae^{-qz}\cos(\frac{\pi}{a}z + \delta) \tag{2.9}$$

where A is a normalization constant, q is the imaginary part of the wave vector in the $+z$-direction, and δ is a phase factor which depends on the sign of V_g. This amplitude of wave function decays in the crystal side (z > 0) with sinusoidal oscillation. In the vacuum side (z < 0), the wave function should have a form decaying exponentially,

$$\psi = Be^{+qz} \tag{2.10}$$

where B is a normalization constant. The coefficients A and B can be obtained by using the boundary conditions for ψ and $\frac{d\psi}{dz}$ at z=0. In particular, ψ and $\frac{d\psi}{dz}$ are continuous at z=0. The surface states exist only for V_g < 0. In case of V_g > 0, there is no possible solution to satisfy the boundary condition.

Shockley surface states of metals either contribute the properties of metal surfaces or can be used as a monitor for surface phenomena including reconstruction, adsorbate diffusion, and the potential and kinetics of adsorption processes. Among them, the effect of Shockley states on physisorption and chemisorption is of particular interest in this dissertation. The physisorption potential is mainly composed of van der Waals interaction and Pauli repulsion. The electron density from the occupied surface states can strengthen the Pauli repulsion and then destabilize the molecule-metal physisorption bond. For instance, Pt(111) and Pd(111) are analogous transition metal surfaces but the adsorption enthalpies for Xe on Pt(111) (280meV/Xe atom) and Pd(111) (360meV/Xe atom) are very different. Also, the bond length of Xe-Pt is 1Å longer than Xe-Pd. The adsorption enthalpies and bond lengths are correlated well with the fact that the Shockely state in Pt(111) is partially occupied while that of Pd(111) is unoccupied. The interaction of Xe with the occupied surface state of Pt(111) results in the upshift of the surface state energy. The pre-treatment of Pt(111) with oxygen depopulates the Shockley states and strengthens the physisorption bond of Xe-Pt. The modification of the physisorption potential is also important for the kinetics of chemisorption. The potential barrier in a transition from physisorption to chemisorption species is determined by the intersection region of their potential surfaces. The occupancy of surface states raises the physisorption potential resulting in an increase of the potential barrier and thus a decrease in the rate of chemisorption.

In addition to the Pauli interaction with adsorbate, the upshift of Shockley surface state can be induced by the lateral scattering of electrons with adsorbates. The scattering of surface electrons have been an important topic as a model system of two-dimensional quantum confinement phenomena. Hormandinger et al[10] gave a detailed theoretical description of quantum confinement of surface electron by periodic arrays of Fe, Cu, S, and C. Depending on the nature of interaction, attraction (d-element) or repulsion (p-element), the properties of a surface state (the energy shift, peak broadening, and dispersion) were investigated. Recently there have been several STM studies that show surface-electron confinement in nanoscale pattern consisting of organic molecules [11, 12].

2.1.4 Image Potential State[13-16]

Image potential states are originated from the Coulombic interaction of electron with the positive image charge in the metal. Figure 2.5 illustrates image charge formation in the presence of an electron on metal surface. Note that the image charge is located at the same distance from the surface boundary as the electron is.

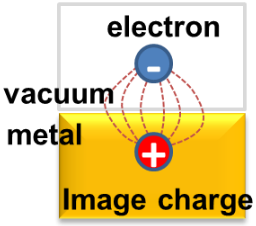

Figure 2.5 Schematic illustration of interaction between an electron and image charge

The image potential states are confined between crystal and image potential barrier leads but freely move parallel to the surface. Its wavefunction and binding energy can be obtained from a one-dimensional hydrogen atom model. In this model, the crystal and the image potential barrier are defined as the infinite step potential wall and Coulombic potential $V(z)$, respectively.

$$V(z) = E_{vac} - \frac{e^2}{4z} \tag{2.11}$$

where z is the distance of electron from the metal surface and E_{vac} is the energy of vacuum level. The solution of Schrodinger equation including $V(z)$ is a Rydberg series

$$E = E_{vac} - \frac{Ry}{16}\frac{1}{n^2} = E_{vac} - \frac{0.85}{n^2} \tag{2.12}$$

where Ry is 13.6 eV and n is the principle quantum number. The binding energy of image states n=1, 2, and 3 are 0.85eV, 0.21eV, and 0.094eV, respectively. Figure 2.6 shows the numerical solution of the image states from MATLAB program. Note that n=1 state is just 2 - 3 Å above the surface but n=2, 3 states are farther away from the surface. The lifetime of high-energy image states are usually longer than low-energy ones because of the decoupling of the image state from substrate.

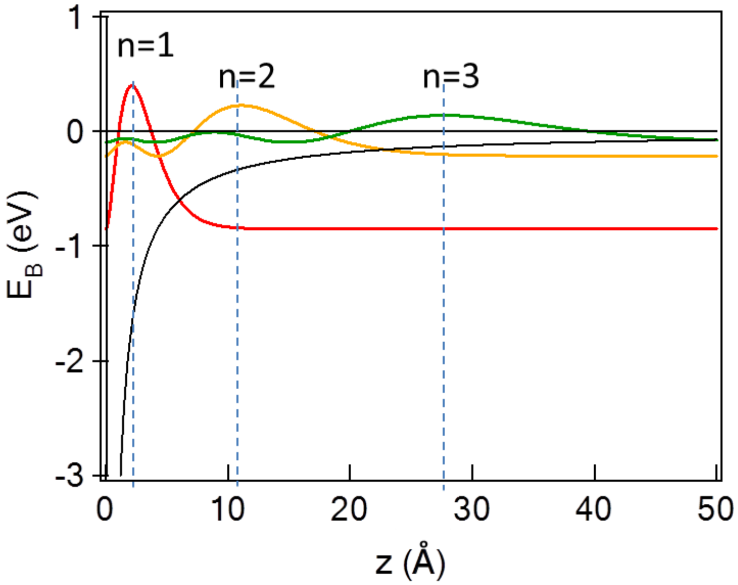

Figure 2.6 Numerical solutions of the Schrodinger equation with an image potential $V(z)$. Three image states (n=1, 2, 3) are represented by red, orange, and green lines. The dashed lines indicate the most probable position of electron from the metal surface.

The simple hydrogenic model described in the above is useful to understand the basic physics of image states. However the infinite potential wall in the crystal side is not an accurate assumption. In fact, the image electron wavefunction can penetrate into the bulk and be coupled with the bulk electronic states by photoexcitation. Multiple reflection theory combined with nearly-free electron model[17] can treat the image state in a quantitatively accurate way. In this treatment, the binding energy of image state is

$$E = E_{vac} - \frac{Ry}{16}\frac{1}{(n+a)^2} \tag{2.13}$$

where a is a quantum defect parameter that depends on the phase change of wave function by the reflection on the crystal potential.

Image potential states have been an important subject in two-photon photoemission studies on bare and atom- or molecule-adsorbed metal surface. Image states are easily observed by photoemission probe and possess well-defined properties such as binding energy and lifetime. Thus image states often serve on the model system to study excited electronic states on surfaces. In addition, image states can be used as a sensitive surface probe mainly because these states are located few to few tens of Ås above the surface. Atomic or molecular adsorbates modify the image potential, resulting in the change of the spectral feature of image states, their dispersion, and relaxation dynamics. Finally, the image potential may actively contribute to the charge transfer at molecule-metal interface and stabilize the charged product of surface photochemistry. Understanding of image state could be important to predict or control the device performance and surface chemistry.

The effects of adsorbates on image potential states can be described by Dielectric Continuum Model (DCM). DCM approximates the adsorbate as a structureless dielectric layer which screen or enhance Coulombic interaction of image electrons. Although this model was successful to explain image states from insulator/metal interface, there is no report for organic semiconductor interface. This is because this model does not include the electronic structure of adsorbates and does not consider the structure of adsorbates. There was an effort to make a new model including the electronic nature of organic semiconductor in the DCM model using a two-band model but this model was not further studied or applied after this work. Here I reproduced Lingle's treatment of DCM model[16] to depict how dielectric layer act on image states in either repulsive or attractive interactions. This model successfully demonstrates how alkane adsorbate layers modify the binding energy of image states depending on their thickness and electron affinity. The model potential is divided into the potential inside (V_{in}) and outside (V_{out}) of the adlayer.

$$V_{out}(z,d) = \frac{-\beta e^2}{4(z-d)} + \frac{(1-\beta^2)e^2}{4\beta}\sum_{j=1}^{\infty}\frac{(-\beta)^j}{z-d+jd} \qquad z > d \tag{2.14a}$$

$$V_{in}(z) = -\frac{e}{4\epsilon z} + V_0 \qquad 0 < z < d \tag{2.14b}$$

where z is the distance from the metal surface, d is the thickness of adlayer, ϵ is the dielectric constant, $\beta = (\epsilon - 1)/(\epsilon + 1)$, and $-V_0$ is the electron affinity. In the right-hand side of equation 2-14a, the first term is the image potential outside an infinite dielectric slab and the second term is the interaction of electron with the metal through the finite dielectric slab. Equation 2-14b is the simple image potential plus electron affinity. Figure 2.7 shows the DCM model of 2ML *n*-octane/Ag(111). the important parameters, ϵ, V_0, and d are set to 2, +0.2 eV, and 4 Å, respectively, In order to remove the singularity of potential, two cutoff parameters are employed around z=0 and z=d.

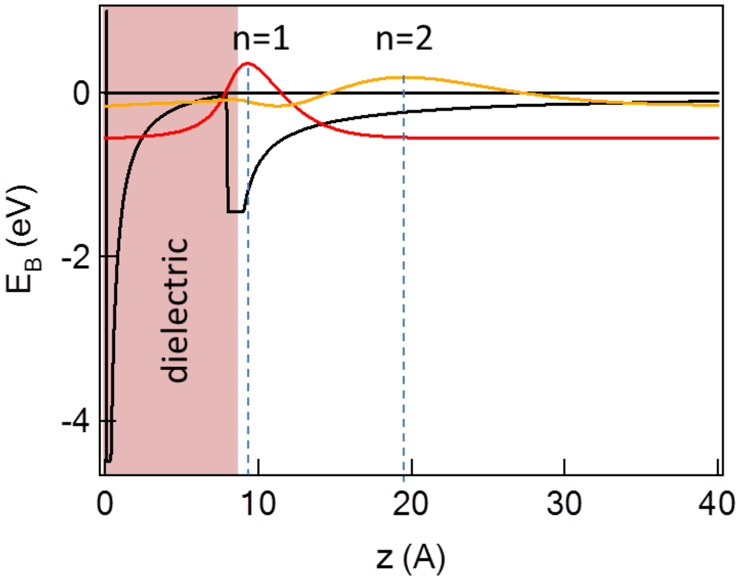

Figure 2.7 The DCM model for 2ML n-octane/Ag(111) and wavefunctions for n=1 and 2 image state from the model potential

In this model, the maximum probable positions of image-state wavefunctions are ~9 Å and ~19, which are farther away from the surface than with bare Ag surface. Their binding energies, 0.55 eV (n=1) and 0.16 eV (n=2) are lower than those of the bare Ag (0.75eV for n=1 and 0.20eV for n=2). The smaller binding energy of image electrons is due to the formation of a repulsive barrier by alkane adlayer. This result agrees well with the fact that alkanes possess large HOMO-LUMO gap and negative electron affinity. If V_0 is set to −0.4 eV, the binding energy of n=1 and n=2 states are 0.75 eV and 0.34 eV, respectively. While the binding energy of n=1 state is similar to that of bare Ag, the binding energy of n=2 state is much lower. The dielectric layer with positive electron affinity may form a quantum well where electrons are trapped and stabilized.

2.1.5 Chemisorption and molecule-metal hybridized states[15]

Chemisorption involves the chemical interaction or reaction between adsorbates and substrate. The chemical interaction of adsorbate-metal can be approximated to the problem of how a single electronic state interacts with a broad continuum state. In the weak chemisorption limit, where the interaction energy is much smaller than the bandwidth of continuum state, the chemisorption leads to a broadening of the resonant electronic state. On the other hand, in the strong chemisorption limit, the result of interaction leads to two separate electronic states. The former is often observed in the *sp*-band of metal and the latter is relevant to *d*-band of metal.

.

2.2 Nonlinear Optics of Materials

2.2.1 Linear Polarization[18]

The propagation of light through optical medium can be described by the wave equation derived from Maxwell equation. The wave equation has the following form,

$$-\nabla\tilde{E}^2+\frac{1}{c^2}\frac{\partial^2\tilde{E}}{\partial^2 t}=-\frac{4\pi}{c^2}\frac{\partial^2\tilde{P}}{\partial^2 t} \tag{2.15}$$

where $\tilde{E}$ and $\tilde{P}$ are electric field and polarization, respectively. The tilde "~" on E and P denotes a quantity varying rapidly in time. The polarization of medium on the right-hand side acts as a source term of electric field. For example, when an object is illuminated by an electromagnetic wave, it becomes polarized and radiates an electromagnetic wave (Rayleigh scattering).

Polarization is the response of medium to the applied electric field and is usually described by the relationship,

$$\tilde{P}(t) = \chi \tilde{E}(t) \tag{2.16}$$

The second-rank tensor, χ, is linear electric susceptibility. The susceptibility is a macroscopic property. In order to describe the polarization or induced dipole of single units such as atoms (or molecules), we use polarizability α, which is related to electric susceptibility by the relationship,

$$\chi = N\alpha \tag{2.17}$$

if the local-field effect is ignored and all the atomic dipoles are aligned in the same orientation. With the local-field effect correction, the resulting equation is

$$\chi = \frac{N\alpha}{1 - \frac{4}{3}\pi N\alpha} \tag{2.18}$$

Polarizability is approximately proportional to the volume of an atom. This relationship can be simply proven by considering the force equilibrium of the external electric field and the induced electric field.

$$\alpha \sim R^3 \tag{2.19}$$

where R is an atomic radius.

2.2.2 Higher- Order Polarization[18]

Higher-order susceptibilities are introduced to describe the polarization of an optical medium under a strong laser field. The polarization is expressed in a power series in electric field, given by

$$\tilde{P}(t) = \chi^{(1)}\tilde{E}(t) + \chi^{(2)}\tilde{E}^{2}(t) + \chi^{(3)}\tilde{E}^{3}(t) + \cdots \tag{2.20}$$

where $\chi^{(2)}$ and $\chi^{(3)}$ are second- and third-order electric susceptibilities, respectively. The wave equation involved in nonlinear polarization is obtained by a replacement of the polarization term in Equation 2-15.

$$-\nabla\tilde{E}^{2} + \frac{1}{c^{2}}\frac{\partial^{2}\tilde{E}}{\partial^{2}t} = -\frac{4\pi}{c^{2}}\frac{\partial^{2}\tilde{P}^{NL}}{\partial^{2}t} \tag{2.21}$$

where $\tilde{P}^{NL}$ is the nonlinear polarization. Higher-order polarization under strong field can be explained in a model treating atoms as a classical anharmonic oscillator model. This model is extended from Lorentz model by adding nonlinear responses, e.g., the quadratic or cubic dependence on the displacement of electrons of the potential. The solution of the differential equation may include doubled- or tripled-frequency of electron oscillation relative to the oscillating electric field. The power of these higher-order frequency responses depend quadratic ally or cubically on the fundamental power. This classical treatment is very intuitive but does not yield the complicated resonance nature of optical nonlinearity. The complete description of optical nonlinearity requires quantum mechanical treatments.

2.2.3 Third-Harmonic Generation (THG)

THG is the third-order nonlinear optical process that three photons of frequency ω are destroyed and one photon of frequency 3ω is created. Figure 2.8 gives the energy-level description of THG process.

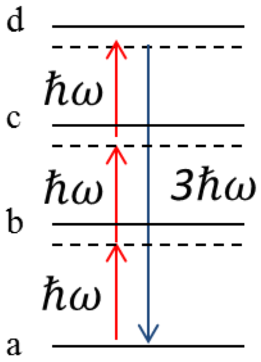

Figure 2.8 THG with resonance energy levels

The polarization of THG can be represented as

$$\tilde{P}(t) = P(3\omega)e^{-i3\omega t} + c.c \tag{2.22}$$

$$P(3\omega) = \chi^{(3)}(3\omega)EEE \tag{2.23}$$

The third-order susceptibility $\chi^{(3)}$ for THG is given by

$$\chi^{(3)}_{ijkh}(3\omega,\omega,\omega,\omega) = \frac{N}{\hbar^3}\frac{\mu^k_{ad}\mu^j_{dc}\mu^i_{cb}\mu^h_{ba}}{[(\omega_{da}-3\omega)-i\gamma_{da}][(\omega_{ca}-2\omega)-i\gamma_{ca}][(\omega_{ba}-\omega)-i\gamma_{ba}]} \tag{2.24}$$

where ω is the frequency of fundamental wave; 3ω is the THG frequency; N is the number density of atoms; the indices $abcd$ are referred to the energy levels of the atom; the indices $ijkh$

are the Cartesian components (*x*, *y*, *z*) of field; $\mu_{mn}^{h} =< m|\mu|n >$ with the field in h-direction; $\gamma_{mn}$is the damping or decay rate of coherence term between *m* and *n* states. Equation 2-24 shows the enhancement of THG field in resonance with the atomic levels indicated in Figure 2.8.

2.2.4 Spatial Symmetry Consideration for Third-Order Susceptibility[18, 19]

The third-order susceptibility $\chi_{ijkh}^{(3)}$ consists of 3^4 = 81 Cartesian components. The number of components in $\chi_{ijkh}^{(3)}$ can be reduced by considering the spatial symmetry of the crystal. For example, isotropic crystals have only 21 nonzero elements of $\chi_{ijkh}^{(3)}$. Among these elements, only 3 are independent. Here we show how symmetry operations reduce the number of elements. For examples, the reflection on *yz* plane leads to

$$x \rightarrow -x$$

$$y \rightarrow y$$

$$z \rightarrow z$$

If $\chi_{pqrs}^{(3)}$ includes an odd number of *x* in its indices (e.g., $\chi_{zxxx}^{(3)}$), the *yz* reflection change the sign of $\chi_{pqrs}^{(3)}$. However, the crystal possesses isotropic symmetry and thus the sign of $\chi_{pqrs}^{(3)}$ must be conserved after reflection. In order to satisfy two contradictory conditions, the $\chi_{pqrs}^{(3)}$ must vanish. The same rule is applied to the elements with an odd number of *y* and *z*. All the elements with an odd *x*, *y*, or *z* should vanish. The number of the remaining elements is thus 21. Further consideration of the isotropic symmetry reduces the independent number of nonzero elements of $\chi_{ijkh}^{(3)}$. The table of crystal symmetry and fourth-rank tensor can be found in the reference[18].

2.2.5 Hyperpolarizabilities and Their Scaling Law[18]

The nonlinear optical susceptibilities, $\chi^{(3)}$ are related to the microscopic property of materials: third-order hyperpolarizability γ. Without local-field correction, their relationships can be expressed as

$$\chi^{(3)} = N\gamma \tag{2.25}$$

In section 2.4.1, atomic polarizability can be approximated to be proportional to the atomic volume. A similar relationship was derived for the hyperpolarizability γ from the model of hydrogen atom.

$$\gamma \cong V^{7/3} \tag{2.26}$$

Similar but more generally valid models were also proposed by Wang[20].

$$\chi^{(3)} = \frac{g'}{N_{eff}\hbar\omega_0}(\chi^{(1)})^2 \tag{2.27}$$

where N_{eff} is the product of molecular number density with oscillator strength, $\omega_0$is an average transition frequency, and g' is a dimensionless constant. Based on Wang's formula, the hyperpolarizability γ is

$$\gamma = \frac{g}{\hbar\omega_0}\alpha^2 \tag{2.28}$$

where g is a constant.

2.2.6 Nonlinear Optical Properties of Conjugated System[18]

According to the table[18] of bond polarizability, the C=C bond has roughly 3~4 times stronger polarizabilty than the C-C bond. The strong polarization property of the C=C bond is related to the fact that the π bond electrons are less tightly bound than σ bond and tend to delocalize through the molecule. As shown in 2.4.4, the hyperpolarizability is directly related to the linear polarizability. Thus the nature of bonds in molecules or materials may determine the strength of hyperpolarizability.

Conjugated polymers, whose molecular structure consists of alternating single and double bonds, have extremely large nonlinear optical response. For example, polydiacetylene possesses two-order-of-magnitude larger third-order nonlinear susceptibility than carbon disulfide. Such huge optical nonlinearity is attributed to the polarizability of conjugated system. Since the electrons are regarded to freely move through the conjugated polymer, this polymer can be approximated as a square well with length L. In this approximation, linear polarizability α and third-order hyperpolarizability γ are proportional to L^3 and L^5, respectively, where L is the polymer chain length. Although systematic experimental studies were only carried out for polymer systems, large nonlinear optical susceptibility is expected in other highly conjugated systems.

References

1. Cahen, D.; Kahn, A., Electron Energetics at Surfaces and Interfaces: Concepts and Experiments. *Adv. Mater.* 2003, 15, 271-277.

2. Kiejna, A.; Wojciechowski, K. F., *Metal surface electron physics*. Elsevier: 1996.

3. Koch, N.; Ueno, N.; Wee, A. T. S., *The Molecule-metal Interface*. Wiley. com: 2013.

4. Braun, S.; Salaneck, W. R.; Fahlman, M., Energy-Level Alignment at Organic/Metal and Organic/Organic Interfaces. *Adv. Mater.* 2009, 21, 1450-1472.

5. Koch, N., Organic Electronic Devices and Their Functional Interfaces. *ChemPhysChem* 2007, 8, 1438-1455.

6. Vázquez, H.; Flores, F.; Kahn, A., Induced Density of States model for weakly-interacting organic semiconductor interfaces. *Org. Electron.* 2007, 8, 241-248.

7. Lüth, H., *Solid surfaces, interfaces and thin films*. Springer: 2010; Vol. 8431.

8. Hűfner, S., *Photoelectron Spectroscopy: principles and applications*. Springer: 2003.

9. Memmel, N., Monitoring and modifying properties of metal surfaces by electronic surface states. *Surf. Sci. Rep.* 1998, 32, 91-163.

10. Hörmandinger, G.; Pendry, J. B., Interaction of surface states with rows of adsorbed atoms and other one-dimensional scatterers. *Phys. Rev. B* 1994, 50, 18607-18620.

11. Lobo-Checa, J.; Matena, M.; Müller, K.; Dil, J. H.; Meier, F.; Gade, L. H.; Jung, T. A.; Stöhr, M., Band Formation from Coupled Quantum Dots Formed by a Nanoporous Network on a Copper Surface. *Science* 2009, 325, 300-303.

12. Cheng, Z.; Wyrick, J.; Luo, M.; Sun, D.; Kim, D.; Zhu, Y.; Lu, W.; Kim, K.; Einstein, T. L.; Bartels, L., Adsorbates in a Box: Titration of Substrate Electronic States. *Phys. Rev. Lett.* 2010, 105, 066104.

13. Osgood Jr, R. M.; Wang, X., Image States on Single-Crystal Metal Surface. In *Solid State Phys.*, Henry, E.; Frans, S., Eds. Academic Press: 1997; Vol. Volume 51, pp 1-80.

14. Szymanski, P.; Garrett-Roe, S.; Harris, C. B., Time- and angle-resolved two-photon photoemission studies of electron localization and solvation at interfaces. *Prog. Surf. Sci.* 2005, 78, 1-39.

15. Zhu, X. Y., Electronic structure and electron dynamics at molecule–metal interfaces: implications for molecule-based electronics. *Surf. Sci. Rep.* 2004, 56, 1-83.

16. Lingle Jr, R. L.; Ge, N. H.; Jordan, R. E.; McNeill, J. D.; Harris, C. B., Femtosecond studies of electron tunneling at metal-dielectric interfaces. *Chem. Phys.* 1996, 205, 191-203.

17. Smith, N. V., Phase analysis of image states and surface states associated with nearly-free-electron band gaps. *Phys. Rev. B* 1985, 32, 3549-3555.

18. Boyd, R. W., *Nonlinear optics*. Academic press: 2003.

19. Nye, J. F., *Physical Properties of Crystals: Their Representation by Tensors and Matrices*. Oxford University Press: 1985.

20. Wang, C. C., Empirical Relation between the Linear and the Third-Order Nonlinear Optical Susceptibilities. *Phys. Rev. B* 1970, 2, 2045-2048.

Chapter 3

Experimental Methods

3.1 Two-Photon Photoemission Spectroscopy

3.1.1 Background for two-photon photoemission

TPPE is a pump-probe photoelectron spectroscopy to investigate both occupied states and unoccupied states of the system in interest. An occupied state is probed by the coherent two-photon ionization mechanism where the initial occupied state $|0>$ is coupled to a continuum final state $|2>$ above the vacuum level (E_{vac}). An intermediate state $|1>$ between the Fermi (E_F) and the vacuum level (E_{vac}) is probed by the initial excitation to $|1>$ followed by the photoionization to a continuum final state. If there is a narrow-band final state, $|2>$, like a molecular state, they can be also probed by the resonance with the final state. The probing mechanism of initial (occupied), intermediate (bound and unoccupied), and final (unbound and unoccupied) states are summarized in Figure 3.1.

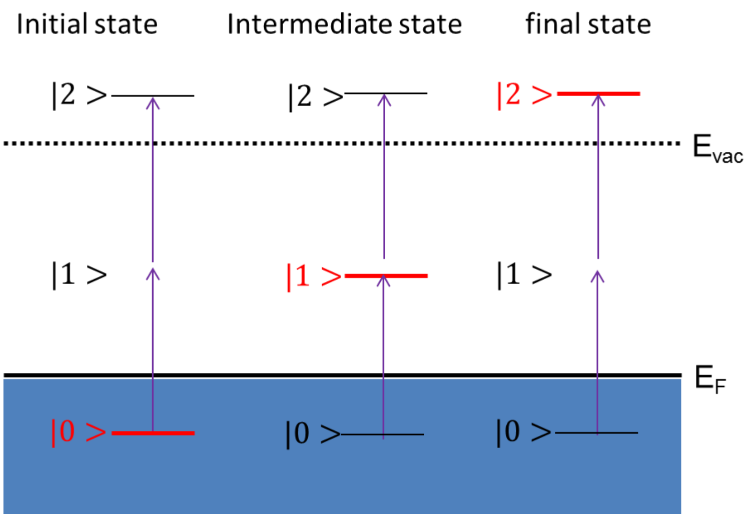

Figure 3.1 Typical resonance excitation pathways of TPPES. Resonance states are indicated by red color. For initial state (left) and final state (right) resonance, there is no resonant intermediate state.

To discriminate between occupied and unoccupied states requires a measurement of a series of TPPE data, each with different photon energy at normal emission angle and the same surface properties. A comparison of the peak shift with photon energy allows determination of the nature of state being examined. Thus for an occupied state, the peak shift is twice the photon-energy difference. For an intermediate state, the peak shift is equal to the photon-energy difference. For a final state, which is above the vacuum level, there is no shift with a change in the photon energy. Figure 3.2 shows how occupied and unoccupied states are identified by photon energy versus peak shift.

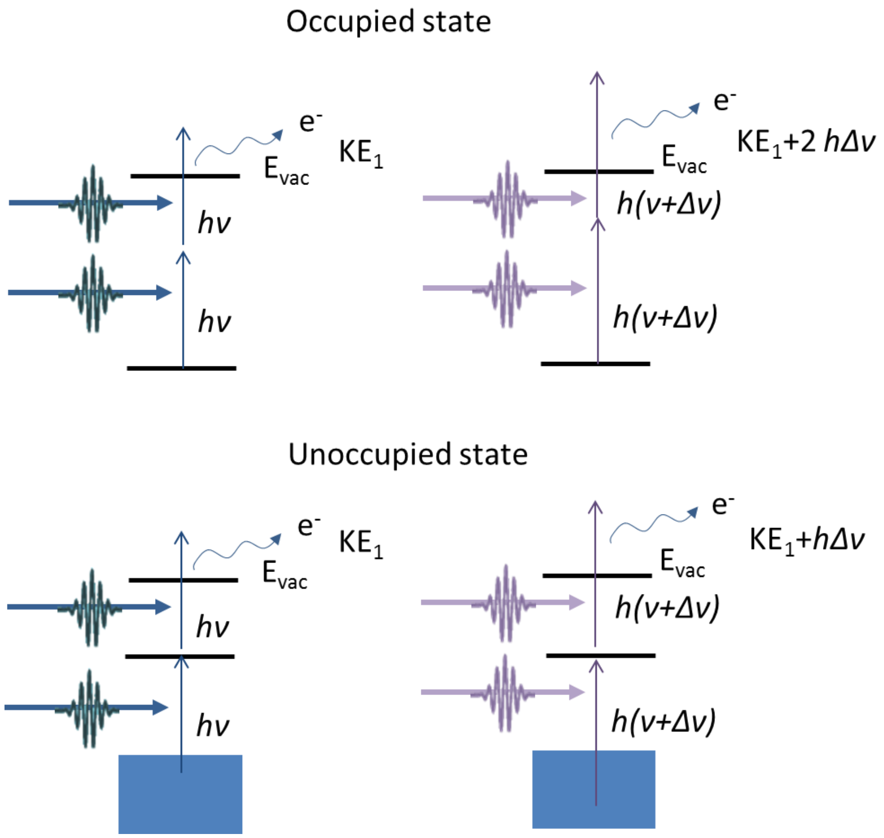

Figure 3.2 Photon energy versus peak shift for occupied (top) and unoccupied (bottom) states

3.1.2 *Work function measurements using two-photon photoemission*

The work function of metal is defined as the difference between the Fermi and vacuum energy levels. The full TPPE spectrum include the lowest energy cutoff (or secondary electron energy cutoff) and the highest energy cutoff (or Fermi edge) as shown in Figure 3.3. The measurement of both cutoff energies enables one to calculate the work function using the relation, $\Phi = 2h\nu-(E_F-E_{LC})$, where E_F and E_{LC} are the Fermi edge and the secondary electron energy cutoff in the TPPE spectra, respectively.

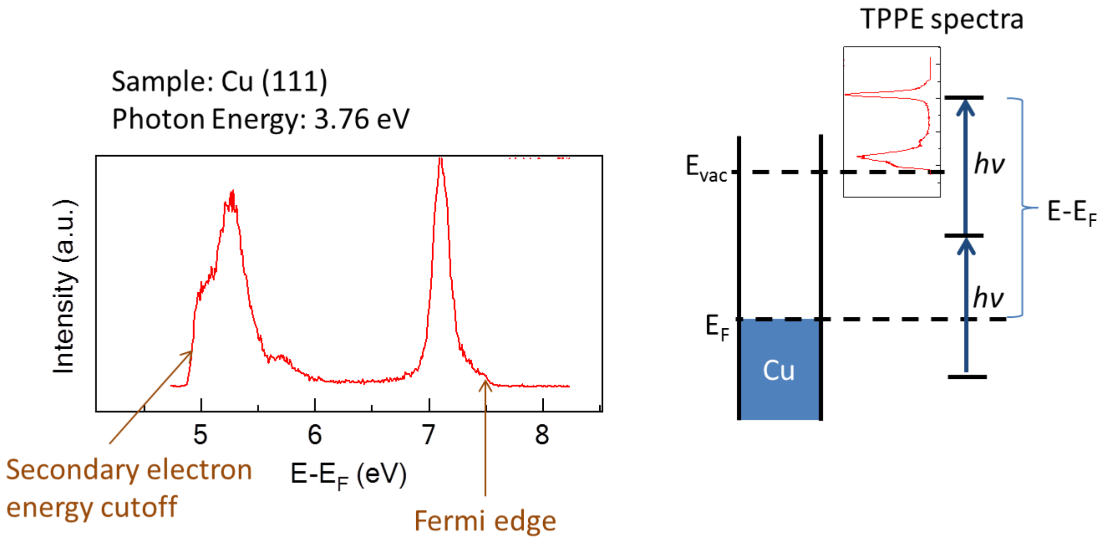

Figure 3.3 A typical example of TPPE spectrum of clean Cu (111) sample. Secondary electron energy cutoff and Fermi edge are indicated. In the right-hand side, the definition of E−E$_F$ (x-axis in TPPE spectrum is shown).

3.1.3 *Calibration of Two-Photon Photoemission Spectra*

In order to determine the kinetic energy of photoelectrons, the electrons need to arrive at a detector, for example, multichannel plate (MCP). The work function of the detector is different from the sample so that there exists a contact potential ($\Phi_{sample} - \Phi_{detector}$). In addition, there is a negative bias, −4 V, typically applied to the sample to increase the kinetic energy of photoelectrons created from the sample in our experiments. This bias helps to separate the photoemission spectra from the secondary electrons created from the detector itself. All those additive potentials, contact potential and bias, increase the measured kinetic energies. Determination of the kinetic energy on the sample surface requires the following calibration procedure:

(1) Find both the lowest and highest cutoff energy of full TPPE spectra.

(2) Calculate work function using the relation, $\Phi = 2h\nu - (E_F - E_{LC})$

(3) Calibrate the measured kinetic energies to fit the lowest cutoff into work function.

This procedure converts the measured energies of photoelectrons into the final-state energies referred to the Fermi level, $E - E_F$.

3.1.4 Determination of effective mass

The concept of effective mass (m^*) is introduced to describe the electron dynamics in the semiclassical model of transport in the solid crystal. It is also common to assess the delocalization of an electronic state by calculating the $m^*$of the state. An effective mass of a state is related to E_{kin} and $k_{||}$ in the dispersion of the state.

$$E_{kin} = \frac{\hbar^2 {k_{||}}^2}{2m^*} + E_0 \tag{3.1}$$

where $\hbar$ is Planck's constant and E_0 is the kinetic energy of electron in the direction of surface normal. The $k_{||}$ is

$$k_{||} = \frac{\sqrt{2m_e E_{kin}}}{\hbar^2} \sin\theta_e \tag{3.2}$$

where m_e is the electron mass and θ_e is an emission angle of photoelectron from the sample. Since the motion of the electrons is influenced by the presence of electric field, The θ_e is not equivalent to the manipulator angle θ_m of the detector (the angle between the entrance of analyzer and the surface normal of the sample). The angle correction, $\theta_x = \theta_e - \theta_m$, is a function of the bias voltage (*U*), photoelectron kinetic energy on the sample (E_{kin}), and θ_m;θ_e and is derived in a simple electrostatic model by Hengsberger et al. The model is shown in Figure 3.4. The analytic solution of the approximate model is given by

$$\tan\theta_x = \sqrt{\frac{eU\left(1-\frac{\sin\theta_m}{\theta_m}\right)}{E_{kin}-eU\left(1-\frac{\sin\theta_m}{\theta_m}\right)}} \tag{3.3}$$

The relative error is less than 1% at the manipulator angle below 15˚. In our experiments, the bias voltage is –4 eV. For monochromatic TPPE experiments, the E_{kin} ranges from 0.5 to 3.5 eV. Figure 3.5 shows θ_x and the resulting $k_{||}$ as a function of θ_m at various E_{kin} and a fixed bias, –4 eV.

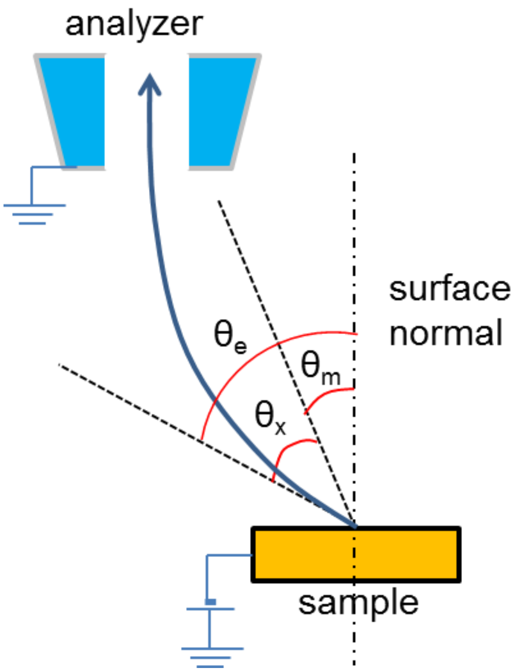

Figure 3.4 Schematic diagrams for calibration of angle-resolved photoemission

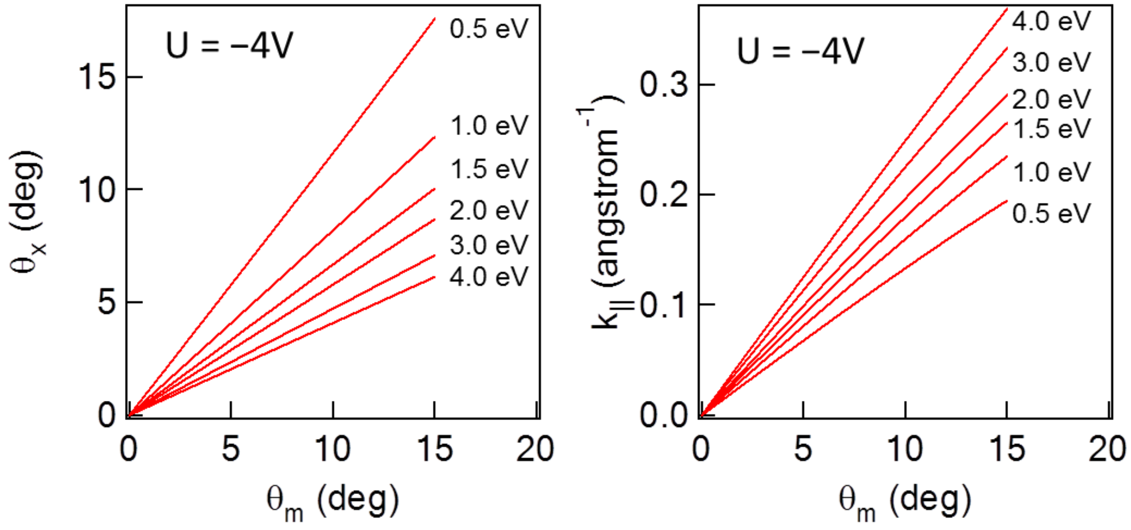

Figure 3.5 Angle correction θ_x and electron wavevector parallel to the surface k|| as a function of manipulator angle (θ_m) various E_{kin}s and a fixed bias, –4 eV

3.2 Two-Photon Photoemission Experimental Setup

3.2.1 Basic Requirements for Two-Photon Photoemission Experiments

TPPE experiments require an ultrashort-pulse laser-excitation source with sufficient photon energies to access the electronic states of interest. The high intensity of ultrashort laser pulses leads to photoionization of electrons in occupied and unoccupied states. In order to differentiate between occupied and unoccupied states, the capability of wavelength tuning is required. There are various sources of tunable radiation: frequency doubler/tripler, optical parametric amplifier (OPA), and optical parametric oscillator (OPO). In order to study ultrafast dynamics occurring at interfaces, the pulse duration should be shorter than ~100 femtoseconds.

All TPPE experiments need to be carried out under ultrahigh vacuum (UHV) environment (10^{-9} ~ 10^{-11} torr). Since the electron penetration depth is just few Å to few nm according to the kinetic energy of electron, it is very important to maintain the surface condition for a sufficient time frame. In an atmospheric pressure, the collision rate of molecule on the surface reaches 3×10^{23} cm^{-2}s^{-1}. This collision rate means that it takes only 3 ns to form a monolayer if the sticking coefficient is unity. For a base pressure of 10^{-9} torr, the monolayer formation time is about 1 hour. Since the sticking coefficients of common residual gases are less than 1, the estimated time for monolayer formation is generally longer.

TPPE experiments also require various in-situ surface instruments equipped on the UHV chamber: low-energy electron diffraction (LEED) instrument, residual gas analyzer (RGA), ion-sputter gun, UHV gas doser, and UHV organic evaporator, etc. These in-situ instruments allow the preparation and characterization of the surface.

3.2.2 Femtosecond Laser Setup

The major light source for our TPPE system is a tunable optical parametric amplifier (Coherent OPA 9400) driven by regeneratively amplified Ti:Sapphire laser pulses (Coherent Rega 9000, 250 KHz repetition rate). The visible output pulses from the OPA are compressed by a Brewster-angle prism pair (material: SF10) and then frequency-doubled in a 1 mm type I BBO crystal, producing a train of wavelength-tunable UV, ~ 90 fs pulses. The UV pulses are again compressed by another prism pair (material: UV-grade silica) before arriving at the sample in the UHV chamber. The photon energies of our UV sources ranges from ~ 3.6 to 4.8 eV. The laser was focused on the sample at a typical maximum fluence of ~10 μJ/cm^2 and at a fixed incidence angle of 70°. Most of the monochromatic TPPE measurements were carried out using this tunable UV laser. For certain TPPE experiments, the remnant ~400nm laser from OPA is used as a light source instead of the UV laser.

For bichromatic TPPE measurements, the fundamental laser pulse (λ ~ 800nm) is divided by a beam splitter into two pulses. The more energetic pulse is directed to the OPA. Since the energy of the split laser is just 2 ~ 3% of the total output power of the amplifier, the OPA output is not significantly affected by the beam splitting. The split near-infrared (NIR) laser pulse is compressed by a prism pair (material: SF10). The pulse duration of the NIR pulse is ~ 50 fs after the compression from our autocorrelation measurements. This NIR pulse is directed to a retroreflector set of mirrors on a motorized translational stage (Newport UTM100CC.1DD, minimum step size: 0.1 μm) for time-delay control. This stage is connected to a computer with Windows XP operating system via MM2000 GPIB interface and computer-controlled by a custom Labview software program. These NIR laser pulses are temporally and spatially overlapped on the sample with the UV laser pulses to run the bichromatic experiments. Before combining the two pulses (UV and NIR) by a dichroic mirror, the beam size of the NIR pulses is optimized by a telescope consisting of a lens pair. The overlap of UV and NIR pulses was initially found by a cross-correlation setup built with another type-I BBO crystal for difference-frequency mixing. A neutral density filter is installed to control the intensity of UV pulse in order to minimize the effect of monochromatic TPPE associated with UV pulse.

The laser setup described the above is shown in Figure 3.1.1 and 3.1.2. The technical details of the Ti: Sapphire laser, optical parametric amplifier, and prism pairs are explained well in the references.

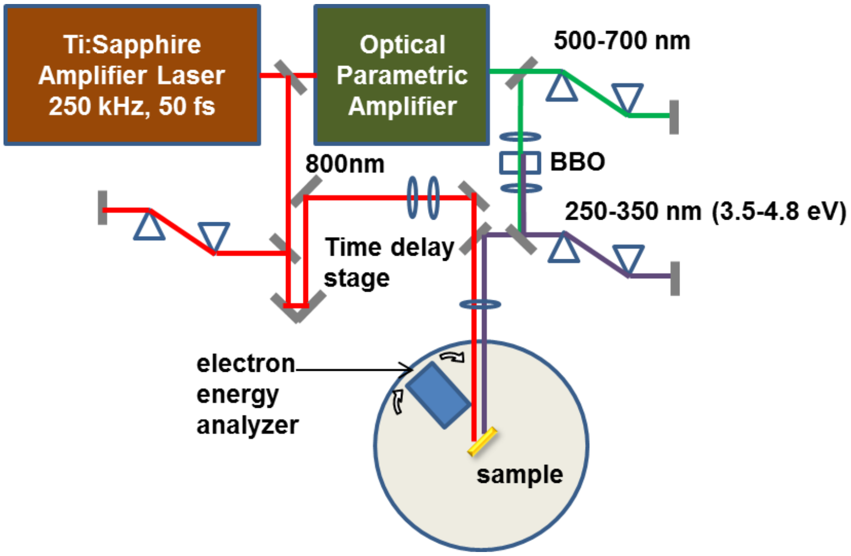

Figure 3.6 Schematic diagram of TPPE laser setup

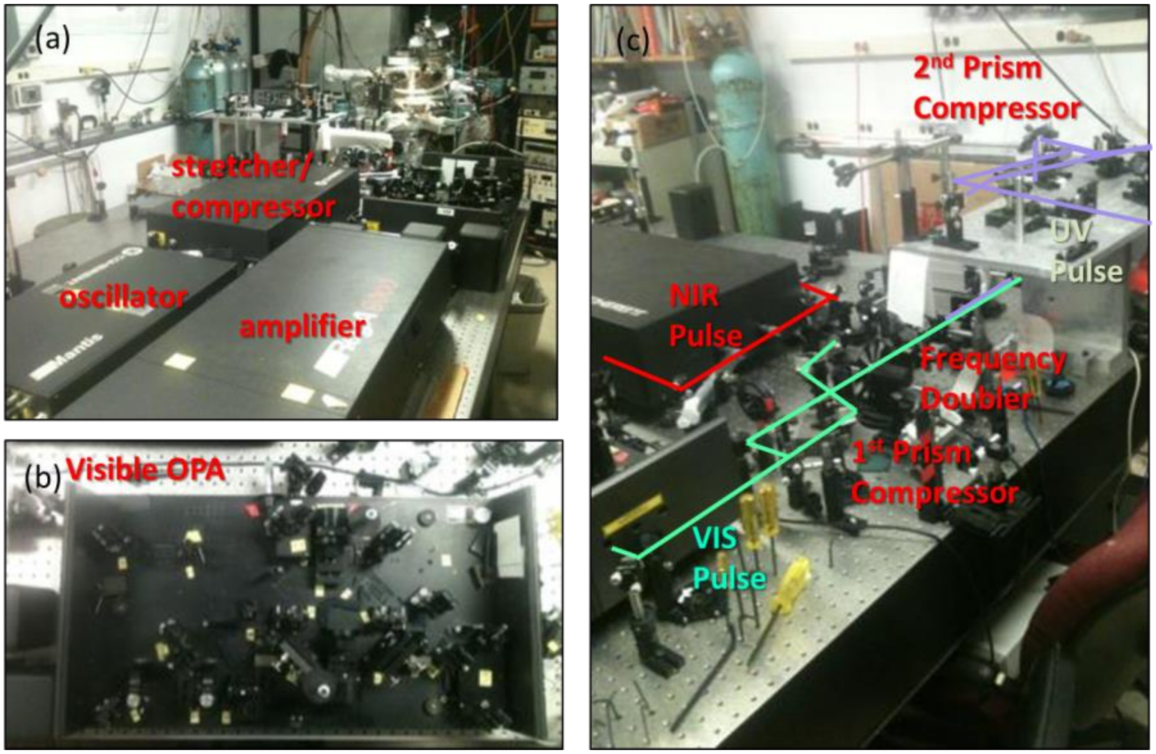

Figure 3.7 Photograph of (a) Ti:Sapphire femtosecond laser amplifier system (b) Visible OPA (b) Laser setup with prism compressors and frequency doubler for UV pulse generation.

3.2.3 Photoelectron Detection System

Photoemitted electrons are collected using a spherical-sector energy analyzer (Comstock ES-101) with a microchannel plate (MCP). The energy analyzer has a momentum resolution of $\delta k_{||} = 0.03$ Å^{-1} and a energy resolution set to ~60 meV. A high voltage supply (Bertan Associates Inc.'s model 215) is connected to the MCP. As shown in Figure 3.8, the detector (energy analyzer plus MCP) is fixed on the rotatable stage and the sample holder is also rotatable independently. The detector was rotated about the fixed sample so as to collect angle-resolved TPPE data along the $\overline{\mathrm{M}}-\overline{\Gamma}-\overline{\mathrm{M}}$ direction of the Cu(111) surface Brillouin zone. In order to find the orientation of the sample, an indicator laser (Uniphase He-Ne laser) was used. The sample was biased at −4 V by a DC power supply (Tektronix PS 280) to reduce the effects of stray electric fields in the vicinity of sample. The photoelectron signal detected by MCP via the energy analyzer is further amplified by a pre-amplifier (EG&G Ortec VT120) and then delivered to the electron energy analyzer controller (Comstock ES-101 electron analyzer power supply). This controller is connected to a desktop computer via a data acquisition card (BNC-2081). The counts of the measured photoelectrons are monitored and recorded by a custom Labview software program.

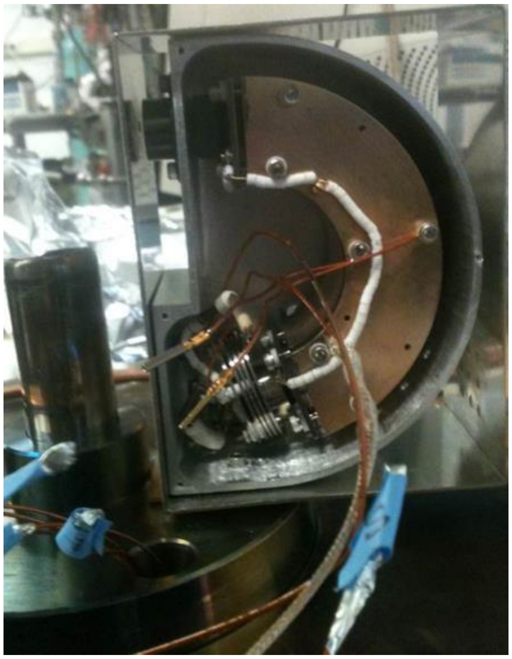

Figure 3.8 Photograph of electron energy analyzer with MCP for photoelectron detection

3.3 Ultrahigh Vacuum (UHV) System

3.3.1 Basic Instrumentation for the UHV system

The base pressure of our UHV chamber, 10^{-9} torr, is maintained by a turbo-molecular pump (Varian, Turbo-V81) and an ion pump. The top differential stage of the chamber and the gas manifold lines are pumped by another turbo-molecular pump. In order to reduce the base pressure after sputtering-annealing cycle, bake-out, or molecular deposition, titanium sublimation pump was operated. Ion sputter gun and LEED instrument (Omicron, SPECTRALEED) allow in-situ cleaning and probing of substrate surface. Residual gas analyzer (Inficon Quadrex 200) indicates the partial pressures of gases in the chamber and was used to monitor small molecules whose masses are below 300 molecular mass. In addition to these basic instruments, a custom molecular gas doser and a custom organic evaporator were added to create molecule-metal interfaces of interest in this dissertation. Figure 3.2.1 showed the UHV chamber and the instrumentation for surface science experiments.

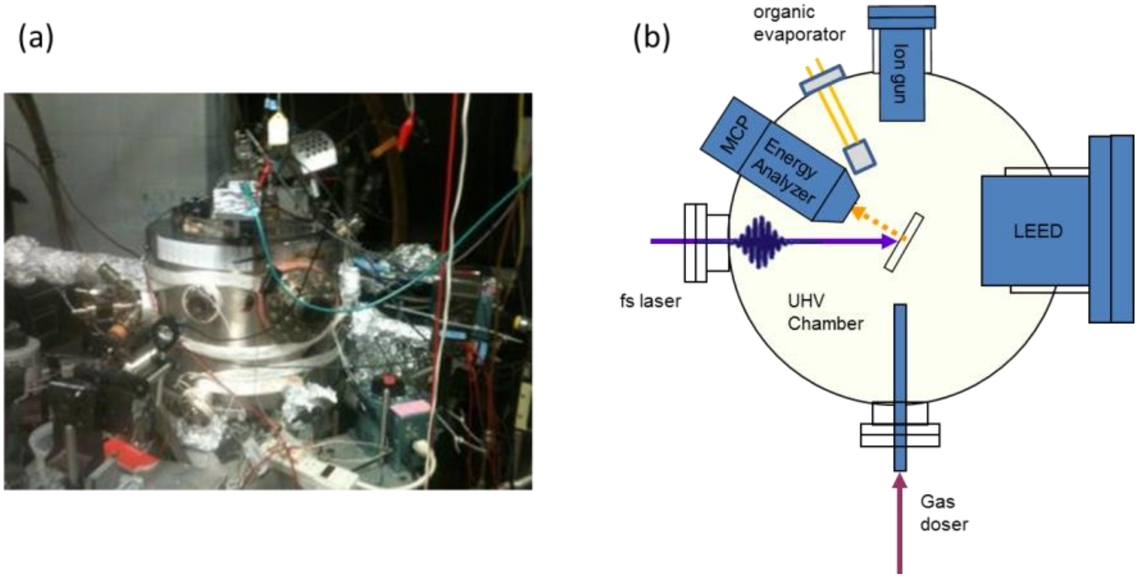

Figure 3.9 (a) Photograph of the UHV chamber for TPPE experiments (b) schematic illustration of the UHV chamber

3.3.2 *Substrate Preparation Setup*

The substrate is a high-purity (99.999% purity) single-crystal Cu(111) disk of 1.2-cm diameter. This Cu disk is held on a pair of electrodes by a Ta wire (Omega, 0.01″) that is welded on the electrodes. The electrode pair is connected to the power supply for resistive heating of the sample. In order to measure the sample temperature, a K-type thermocouple (Omega, 0.003″ chromel and alumel) is attached on the side of Cu substrate with UHV-compatible ceramic glue. The thermocouple is affixed to another pair of electrode so that the sample temperature is monitored in real time by a thermometer.

The sample is prepared typically by Ar^+-sputtering at 1.5 keV for 20 min. and subsequent annealing to 500 ~ 700 ℃. Each sample-preparation cycle is repeated until sharp LEED spots from Cu(111) are observed. The surface condition is also corroborated by a work function measurement using TPPE.

3.3.3 Deposition of Small Molecules on the Substrate Surface

A custom UHV gas doser is designed to dose volatile molecular species directly on the Cu substrate. The molecular sample is contained in a sealed glass tube and low-vapor-pressure impurities are removed by a series of freeze-thaw cycles with dry ice. The pressure inside the doser is measured in real time by a pressure meter. A 5 μm orifice is installed between two final valves to prevent the overflow of molecular gas into the chamber. The nozzle is located 5 cm from the substrate surface to reduce the contamination of chamber. Figure 3.10 and 3.11 showed photographs and an illustration of the gas doser.

A calibrated exposure of the surface is carried out by filling a known volume in the doser with a predetermined pressure of molecular species; this calibrated reservoir is then opened to expose the sample. For the experiments of thiophenol/Cu(111), the pressure of 0.5 torr in the doser is achieved by opening the valve to the glass tube for a minute. The amount of thiol gas in the doser is sufficient to make a saturated coverage of Cu. The following is a general procedure about how to dose a molecular gas by using this instrument.

1) Close all the valves (V1 ~ V6)
2) Open V1, V2, and V6
3) Wait until the pressure reading is steady

4) Close V1 and wait until the pressure reading is steady
5) Open V5 and wait until the predetermined time. Check the pressure changes in the doser and the UHV chamber
6) Close V6 and turn on the mechanical pump
7) Open V3 and wait until the pressure reading is steady
8) Close V3, Open V4, and wait until the pressure reading is steady
9) Close V5
10) Shortly open and close V6 to remove trapped gas between V5 and V6. Repeat this procedure until the trapped gas is completely removed. Before conducting this procedure, move the Cu sample away from the nozzle

The index number of each valve (V1 ~ V6) is shown in Figure 3.11. All surface dosing procedures are carried out on a clean surface in UHV and at room temperature. Further, surface exposure is carried out *via* additional dosing of the previously dosed surface.

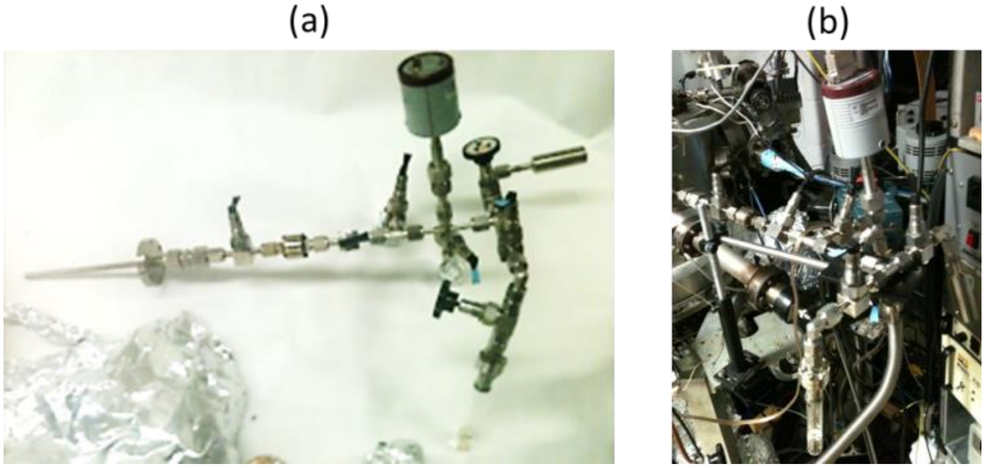

Figure 3.10 Photograph of the custom-made molecular gas doser (a) before and (b) after installation on the UHV chamber.

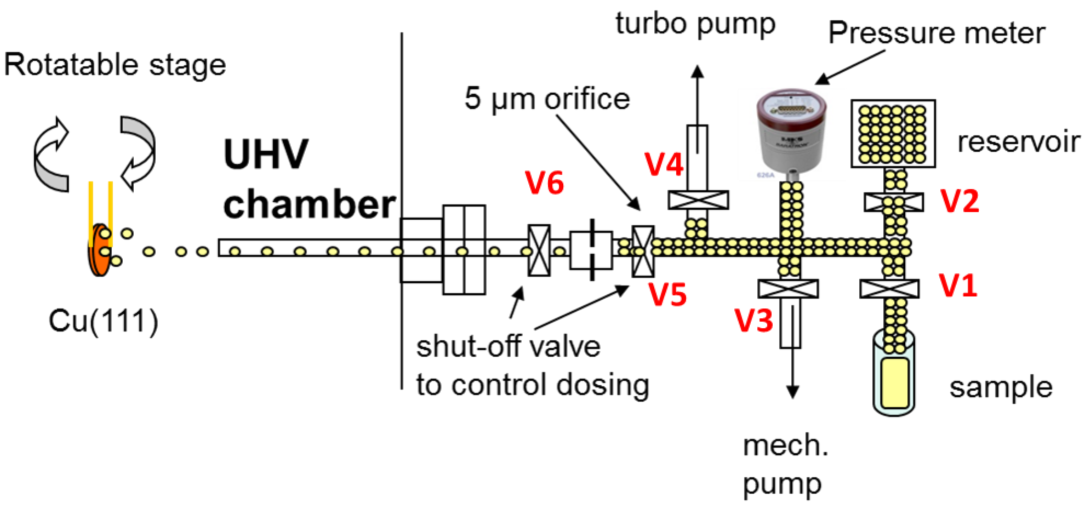

Figure 3.11 Schematic illustration of molecular gas doser

3.3.4 *Deposition of Organic Semiconductor Materials on the Substrate Surface*

A custom organic evaporator is fabricated and used to prepare the organic semiconductor/Cu interface. The crucible is located 10 cm from the sample surface and affixed on the upper part of a pair of copper electrodes A powder of an organic solid is contained in the crucible and can be evaporated by heating the crucible. The crucible is made up of Cerabond 571 (UHV-compatible ceramic materials) and 0.016 ″ tungsten (W) wire and fixed to the upper part of a pair of copper electrodes. The W wire is an indirect heater for the crucible. When there is a current flow through the wire, the wire becomes hot and conducts the heat to the crucible. The temperature of the crucible is monitored in real time with K-type thermo-couple (0.01″ chromel and alumel) attached on the side during the evaporation processes. Both the thermo-couple and the copper electrodes are covered with non-porous alumina spacer to insulate them from the UHV chamber.

Deposition of an organic solid on the surface is carried out by heating the crucible to a predetermined temperature and aligning and rotating the sample toward the crucible. The chamber pressure was monitored by a vacuum gauge and a residual gas analyzer during the preparation. After finishing the interface preparation, the sample was rotated to face away from the dosing source and the crucible was cooled. All deposition processes were carried out on a clean surface or previously dosed sample in UHV at room temperature. Figure 3.12 and 3.13 shows the photographs and the illustration of the evaporator.

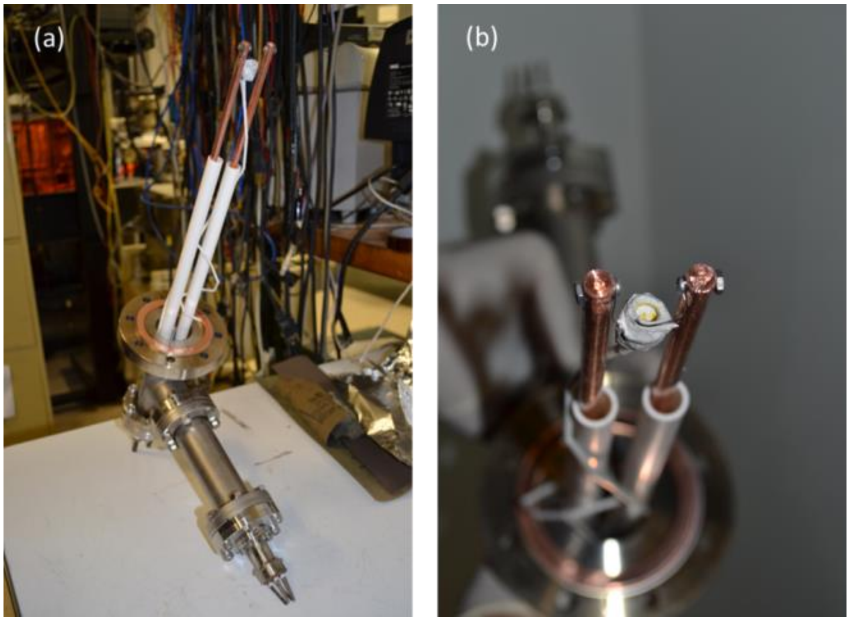

Figure 3.12 (a) Photograph of home-made organic evaporator (b) Close-up photograph of ceramic crucible with a powder of an organic material (hexa-*cata*-hexabenzocoronene)

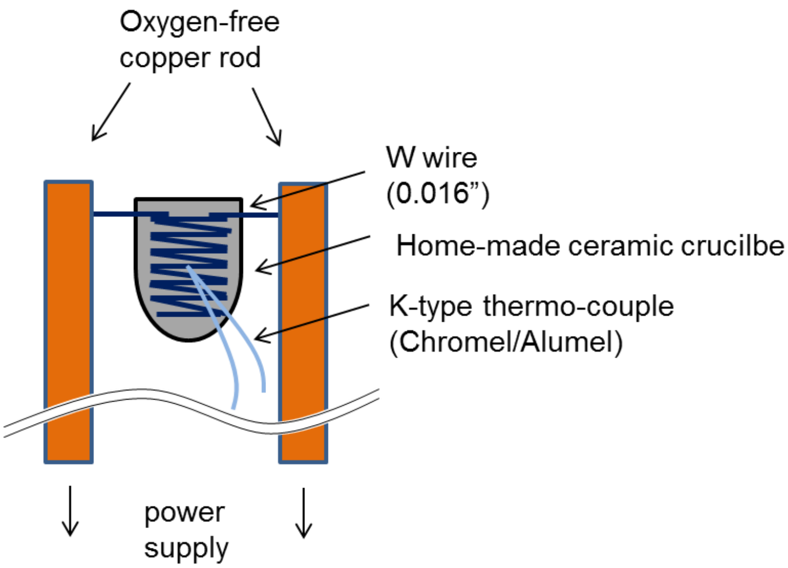

Figure 3.13 (a) Basic design of organic evaporator around the ceramic crucible

3.4 Nonlinear Optical Scanning Microscopy

3.4.1 Femtosecond Laser Setup

Our nonlinear optical microscopy setup (see Figure 3.14) uses a 76MHz train of 789 nm pulses from a Ti:sapphire laser (Coherent Mira). The intensity of laser pulses is adjusted by a variable neutral density filter and the pulse width is compressed to 50 fs by a Brewster-angle prism pair. After passing through a half-wave plate (Eksma), a polarizer (Thorlab, Glan-laser polarizer), and a red filter, the laser is focused by a lens (*f*=50mm) onto the sample with a typical average power of 100 mW at a 60° incidence angle. The sample is mounted on a mated orthogonal-translation (Klinger) and rotation stage (Thorlab, CR1-Z7), which permitted 2D scanning as well as measurements of the rotational anisotropy of the signals from the sample. The reflected signal is collected by a collimating lens and passes through a UV-compatible analyzer polarizer and then a Pellin-Broca prism (Thorlab, material: UV-grade silica) to filter out the fundamental beam and a monochromator, before being detected by a photomultiplier tube (Hamamatsu). The Pellin-Broca prism is mounted on a rotatable stage so that one can select a wavelength to be detected. The monochromator, whose throughput is approximately 10% due to its small bandwidth window, reduces background signal significantly to the level of the dark count.

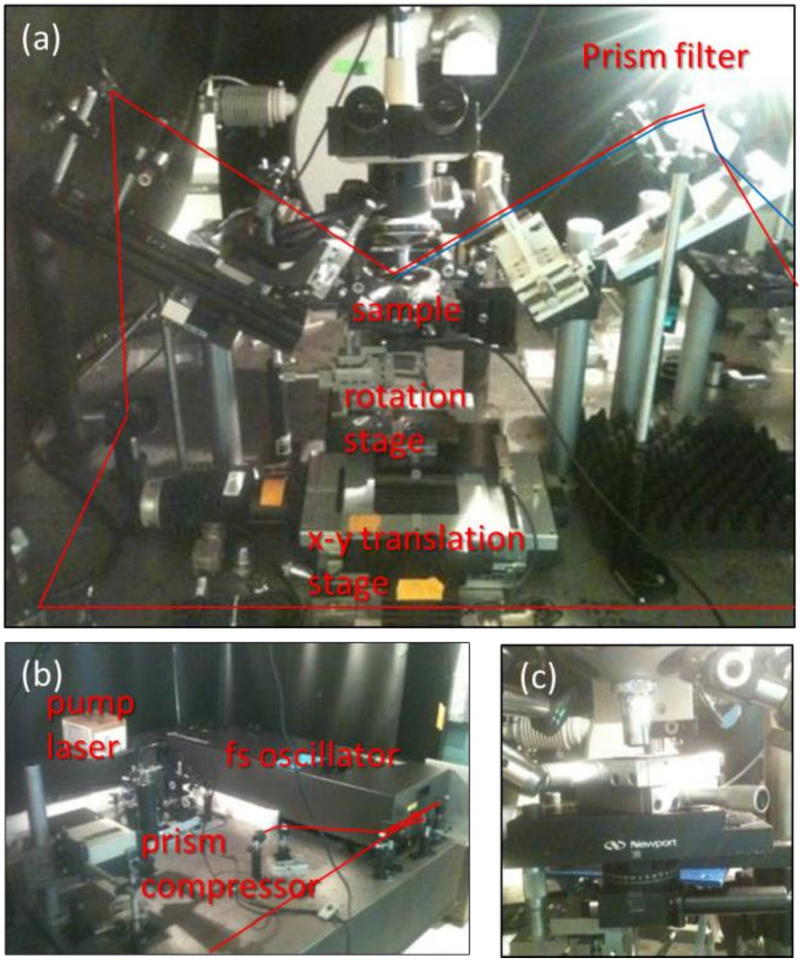

Figure 3.14 Photograph of (a) a custom nonlinear optical scanning microscope for SHG, THG, and photoluminescence imaging experiments (b) Ti:Sapphire femtosecond laser oscillator system with prism compressor (c) Close-up photograph for sample and motorized rotation state.

3.4.2 Optical Microscope Setup

An optical microscope (Nikon) near the sample mount (see Figure 3.14) allows an optical imaging of micron-scale samples such as a graphene crystal. At the top of the microscope, a CCD camera (Dino-Lite) is installed to transfer image data to a computer.

3.4.3 Sample Preparation

Single crystals of graphene were grown by chemical vapor deposition (CVD) and subsequently transferred onto glass substrates. The details of the procedures are described in the reference. Briefly, graphene was grown at 1030℃ on 25-µm-thick copper-foil, following low-pressure, encapsulated-growth methods, so as to yield spatially-isolated single crystals with characteristic overall dimensions of approximately 200 µm. The graphene was subsequently transferred onto glass substrates (~1 mm thick), which had been first cleaned in a solution of sulfuric acid and hydrogen peroxide (3:1), utilizing a dry-transfer procedure with PMMA to support the graphene crystals throughout the transfer process.

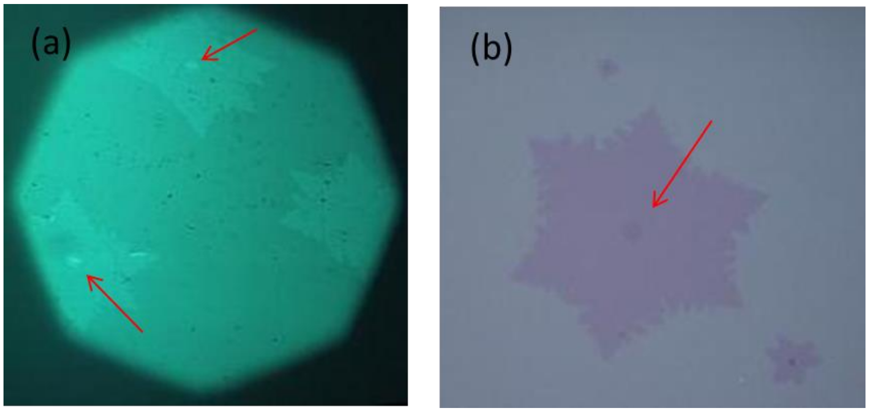

Figure 3.15 Optical image of single-crystal CVD graphene on (a) glass and (b) 300nm SiO_2/Si(001). Red arrow indicates either brighter or dark spot at the center of graphene crystal.

3.4.4 Software for Micron-Scale Scanning System

Motorized 2D-scanning-translational and rotational stages are key equipment to image a nonlinear optical response from a micron-sized sample. Full automation of both motorized stages and a photon counter speeds up the rate of data collection and improves the accuracy and reproducibility. In order to control the stages and provide user-friendly interface, a Labview software program was developed. In this section, the basic operation of the software in the scanning system is briefly reviewed.

Figure 3.3.2 shows “area scan” mode of the program. The other modes, “single spot scan”, “line scan”, and “time scan” are also included in this program. By simply clicking the tab button, one can access each scanning mode. In the “single spot scan” mode, the translation stage is fixed and the rotation stage is moved. This mode is used to collect rotation anisotropy data without imaging the sample. In the “line scan” mode, only a single direction (X or Y) is scanned. In the “time scan” mode, no state is moved but a continuous data collection is conducted. This mode is used to study the stability of sample to the laser exposure.

In the “area scan” mode, one can scan an area of the sample and change the orientation. “X-Start”, “X-End”, “Y-Start”, and “Y-End” determine the area for scan. “X-interval” and “Y-interval” determine the scanning resolution. For example, the parameters in Figure 3.3.2 are set to scan an area of ~1 mm × 1 mm with 10 μm resolution. In the “rotational stage control” panel, “del(angle)” and “times” determine the discrete orientations where image scans are conducted; The first orientation for image-scanning is determined by the value of “initial angle”. After an image-scan, the rotation stage changes the sample orientation as the value of “del(angle)” and the translation stages are then initialized for the next scan. This process is repeated until the rotation stage reaches at the angle of “del(angle)” × “times”. All the other parameters, “Disc level”, "dwell time", and "integration time" are related to the photon counter control. There are also parameters to record external information such as "beam power", "pol", "Sample", etc. This information is recorded in first several lines in the data file. Collected data file are further processed by a MATLAB program to produce an image.

The scanning for high-resolution or large area takes several hours to more than a day. The integration time for TH measurement of graphene monolayer is 0.5s in the optimized setup. In order to collect 1 mm × 1 mm data with 10 μm resolution, it takes 4 ~ 5 hours because there is a waiting time for each stage movement, ~1s.

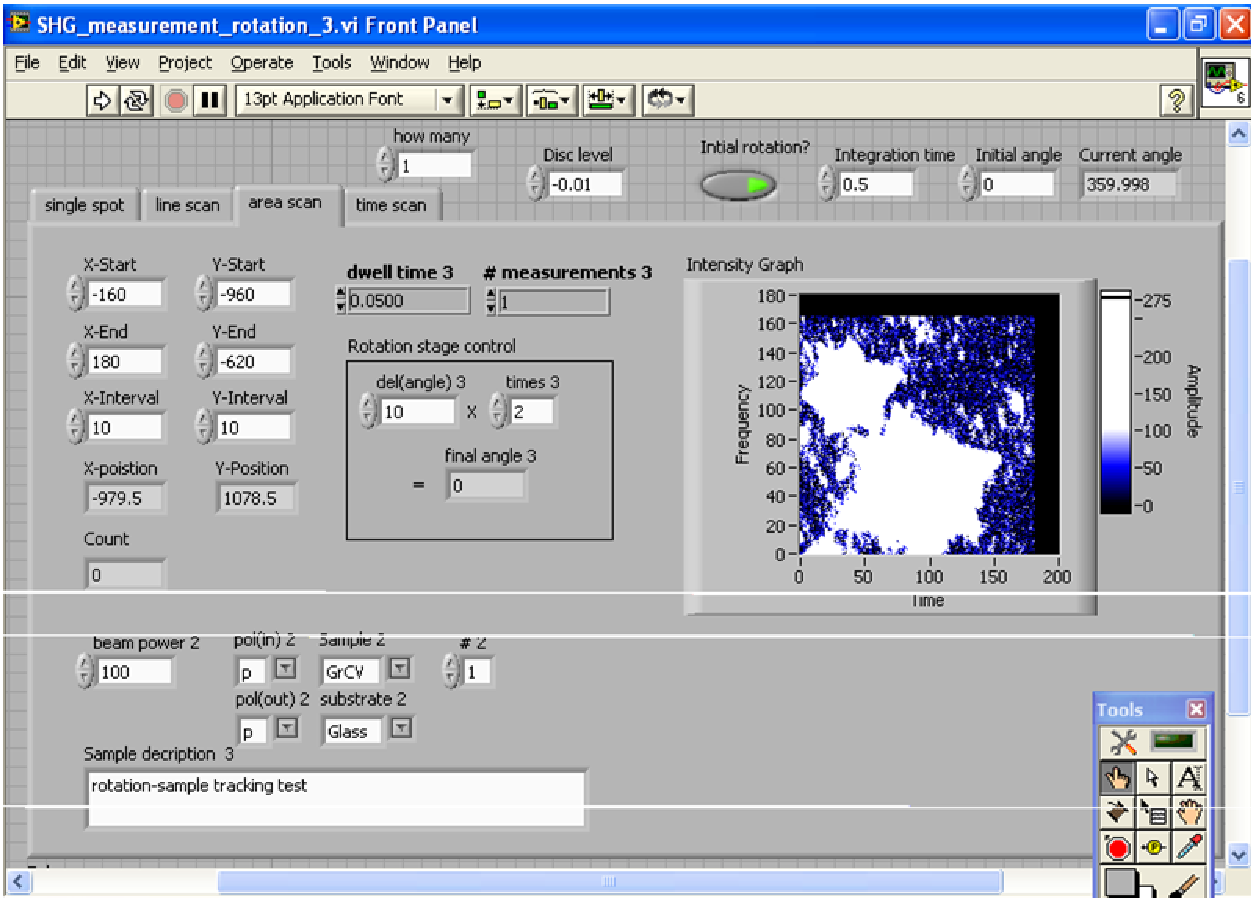

how many 1

Disc level -0.01

Intial rotation?

Integration time 0.5

Initial angle 0

Current angle 359.998

X-Start -160

Y-Start -960

X-End 180

Y-End -620

X-Interval 10

Y-Interval 10

X-poistion -979.5

Y-Position 1078.5

Count 0

dwell time 3 0.0500

 # measurements 3 1

Rotation stage control

del(angle) 3 10 x times 3 2

final angle 3 = 0

beam power 2 100

pol(in) 2 p

Sample 2 GrCV

2 1

pol(out) 2 p

substrate 2 Glass

Sample decription 3

rotation-sample tracking test

Figure 3.16 Labview program for nonlinear optical scanning microscope

Chapter 4

Interfacial Dipole Formation and Surface-Electron Confinement in Low-Coverage Self-Assembled Thiol Layers: Thiophenol and p-Fluorothiophenol on Cu(111)

Model systems of organic self-assembled monolayers (SAMs) are important in achieving full atomic-scale understanding of molecular-electronic interfaces as well as the details of their charge transfer physics. Here we use two-photon photoemission (TPPE) to measure the evolving unoccupied and occupied interfacial electronic structure of two thiolate species, thiophenol and p-fluorothiophenol, adsorbed on Cu(111) as a function of molecular coverage. Our measurements focus on the role of adsorbates in shifting surface polarization and effecting surface electron confinement. As the coverage of each molecule increases, their photoemission-measured work functions exhibit nearly identical behavior up to 0.4-0.5 ML, at which point their behavior diverges; this behavior can be fit to an interfacial bond model for the surface dipole. In addition, our results show the emergence of an interfacial electronic state 0.1-0.2 eV below the Fermi level. This electronic state is attributed to quantum-mechanical-confinement shifting of the Cu(111) surface state by the molecular adsorbates.

4.1 Introduction

Organic-materials-based electronics are of increasing interest because this materials system can be lightweight, thin, flexible and exhibit new functionalities.[1] In most cases understanding interfacial electronic structure is a key factor in solving many of the chemical and electronic issues[1, 2] in these devices; it also gives rise to a series of important fundamental questions,[1-6] including the nature of interface polarization, the height and thickness of interfacial energy barriers and level alignment, interfacial molecular control and its chemical state, interfacial abruptness, and local charge density; these experiments have used samples prepares under either ambient or UHV conditions. UHV conditions enable the use of high resolution proximal and electron spectroscopies, as well as well characterized initial substrate surfaces.

Thus, thiols, in particular, have been of interest to the organic electronics community both as a model molecular class as well as being useful for a series of practical applications including tunable nanoscale contacts and controllable thin film morphologies and interfaces.[3, 7] In some cases, thiols interact with the surface and other adsorbates, either with or without loss of hydrogen at the head group, to form a self-assembled monolayer (SAM) of the intact thiol or as thiolates, respectively, on a variety of surfaces.[7-13] In addition, the selection of thiol functional groups is useful for work function tuning.[3]

Thiol films or layers have a coverage-dependent phase transition.[14] Thus at low coverage, the film structure is loosely packed and in a supine or “lying-down” geometry, while at high coverage, a phase transition occurs and the film structure becomes densely packed with the molecules adopting a “standing-up” geometry. This structural difference has, in fact, been shown to change the work function and electronic structure of thin films structure, on which the thiol has adsorbed.[15-18]

One class of thiols, which has received much attention, is that of aromatic thiols. These materials can be organic semiconductors, which allow close chemical contact with a substrate. Their high conductivities have been verified by single-molecule transport measurements and DFT studies.[19] These results are consistent with reports demonstrating that organic field effect transistors, whose electrodes are treated by aromatic thiols, have better performance than the ones treated by alkanethiols.[20] In addition, recent STM studies showed that selection of chemical moiety and control of surface density can lead to the formation of patterned islands or layers on metal surfaces.[21-23] This surface patterning has potential applications in molecular electronics and gas sensing.

In this chapter, we use two-photon photoemission (TPPE) to make a comparative examination of thiophenol and p-fluorothiophenol (see Fig. 1) adsorbed on a Cu(111) surface as a function of coverage, *i.e.*, 0 - 1ML, with emphasis on values < ~0.5ML. Characterization of the absorbed layers of each of these molecules on Cu(111) dosed under UHV conditions has been reported in the literature for STM and XPS probes.[23, 24] The central difference between the two molecules is that in the latter, the para-positioned hydrogen is replaced by fluorine. This replacement leads to nearly opposite dipole orientations but with comparable magnitudes, *i.e.*, $|\mu_0|$ = 1.24 D for thiophenol (TP) and $|\mu_0|$ = 1.11 D for 4-fluorothiophenol (p-FTP), based on a MP2 calculations.[25] Thus the dipole of thiophenol points away from thiol group but that of 4-flurothiophenol points toward it. In our experiments, we use gas dosing within a UHV system to deposit thiol films of controllable coverage on a Cu(111) surface at room temperature. Our TPPE experiments measure a marked difference in the interfacial dipoles of the two molecules and show how the interaction of the adsorbed molecule with the surface electron leads to a new electronic-state structure due to confinement of the surface electron and, in addition, we are able to observe the consequences of this change in the molecular orientation, hence, surface polarization, as a function of coverage.

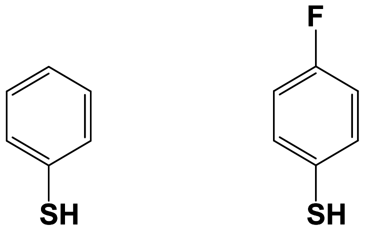

TP **p-FTP**

Figure 4.1 Thiophenol (TP) and p-flurothiophoenol (p-FTP).

4.2 Experimental Section

Our experiments use a high-purity (99.999% purity) single-crystal Cu(111) sample of 1.2-cm diameter. The sample is placed in a UHV chamber ($<2\times10^{-9}$ Torr) equipped with an ion-sputtering gun, a low energy electron diffraction (LEED) instrument, a quadrupole mass spectrometer, and a spherical-sector electron-energy analyzer. The sample is prepared by Ar^+-sputtering at 1.5 keV for 20 min. and subsequent annealing to 500°C. Each sample-preparation cycle is repeated until sharp LEED spots are observed. A UHV dosing system is used to prepare the molecule/Cu interface with its nozzle located 5 cm from the sample surface. A calibrated exposure of the surface is carried out by filling a known volume in the doser with a predetermined pressure of the thiol species; this calibrated reservoir is then opened to expose the sample. Thus all surface dosing is carried out on a clean surface in UHV and at room temperature. Further, surface exposure is carried out *via* additional dosing of the previously dosed surface. After each experimental run of ~10 doses the surface is again cleaned and prepared by sputter annealing.

Our electronic structure and surface polarization experiments make use of angle-resolved TPPE. In order to obtain high signal-to-noise ratio while minimizing space-charge effects, our TPPE system uses a tunable ultrafast optical parametric amplifier driven by regeneratively amplified Ti:Sapphire laser pulses. The visible output pulses are then frequency-doubled in a nonlinear crystal, producing a train of wavelength-tunable UV, 90 fs pulses at 250 KHz repetition rate. The photon energies used ranged from ~ 3.6 to 4 eV. The laser was focused on the sample at a typical maximum fluence of ~10 μJ/cm^2 and at a fixed incidence angle of 70°.

Photoemitted electrons are collected using a spherical-sector energy analyzer having a momentum resolution of $\delta k_{||} = 0.03$ Å^{-1} and the energy resolution set to ~60 meV. The detector was rotated about the fixed sample so as to collect data along the $\overline{\mathrm{M}}$ - $\overline{\Gamma}$ - $\overline{\mathrm{M}}$ direction of the Cu(111) surface Brillouin zone. Our sample was biased at −4 V to reduce the effects of stray electric fields in the vicinity of sample. The resulting data were corrected for both the additional kinetic energy and change in the parallel momentum $k_{||}$ of the electrons due to this accelerating voltage using the method described in a literature.[26]

To discriminate between occupied and unoccupied states requires a measurement of a series of TPPE data, each with different photon energy at normal emission angle and the same surface properties. A comparison of the peak shift with photon energy allows determination of the nature of state being examined. Thus for an occupied state, the peak shift is twice the photon-energy difference. For an intermediate state, the peak shift is equal to photon-energy difference. For a final state, which is above vacuum level, there is no shift with a change in the photon energy. With regard to the angle-resolved capability, the measured angle θ of the detector and the measured kinetic energy E_k are related to the parallel momentum $k_{||}$ of the emitted electron *via* the well-known expression:

$$k_{\parallel} = \frac{\sqrt{2m_e E_k}}{\hbar}\sin\theta . \tag{4.1}$$

Finally note that a measurement of the dispersion curved of a specific spectral f, is well known to allow determination of the degree of the localization of the state.

Finally we emphasize that our LEED observations of the bare surface together with our occupied-state photoemission capability enable us to fully characterize our UHV prepared Cu surface. In addition, our QMS capability also enables full characterization of the adsorbate molecule prior to adsorption.

4.3 Results

4.3.1. TPPE Spectroscopy at low coverage of TP and p-FTP.

Our experiment consisted of exposing a bare surface to a calibrated dose of either of the two molecular species. The TPPE electron energy distribution curve (EDC) was then recorded at different photon energies. Each measurement consisted of a ~1 s exposure at a specific angle setting. Care was taken to ensure that the adsorbate surface was not photochemically altered during the irradiation period by the UV laser.

A representative set of data, taken at normal incidence and $E_{h\nu} = 3.76$ eV (TP) and 3.88 eV (p-FTP) for a series of doses, where $E_{h\nu}$ is the photon energy, is shown in Fig. 4.2. Prior to any exposure, measurements were made on the pristine Cu (111) surface, which in each case exhibited a sharp LEED pattern. As seen in Feature A, on the clean surface, an EDC from a clearly resolved Shockley surface state was obtained at the well-known binding energy of ~ 0.4 eV.[26] When the surface was exposed to TP, the signal from the Shockley surface state decreased with each increasing exposure and a new state, labeled B, grew with the coverage. This peak was located at an energy −0.16 eV with respect to the Fermi level. In addition, as the exposure increased, the low-kinetic-energy cutoff decreased in energy monotonically; this decrease originates from a decrease in the surface work function, as will be discussed below. Also note that as the exposure increased to beyond 50s, state B decreased in amplitude. Finally low-coverage data were also taken for p-FTP and a similar new state located at −0.14 eV appeared and grew as the coverage increased. However, note that for the p-FTP data shown in Fig. 4.2, the decrease in the low energy cutoff and the increase in the corresponding secondary (low energy threshold) electron counts ceased for an exposure above ~90 s; after that exposure, the cutoff then increased and the corresponding secondary electron signal decreased as the exposure was further increased.

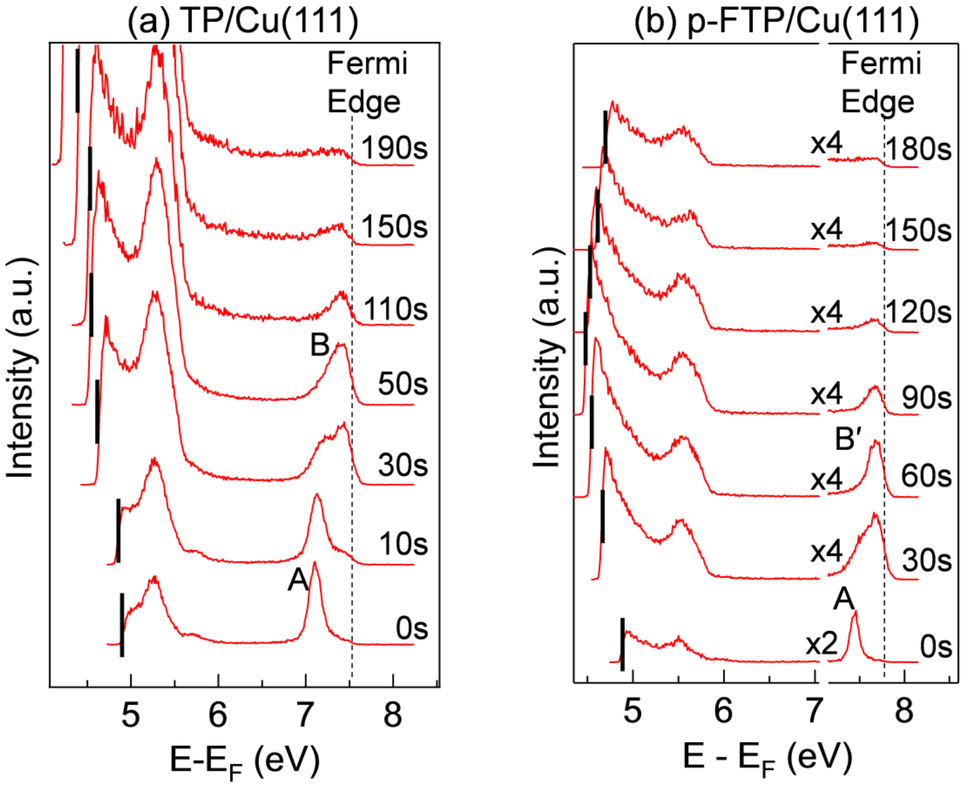

Figure 4.2 TPPE spectra of (a) TP/Cu(111) and (b) p-FTP/Cu(111) at low coverage. These series of spectra were collected at different exposure times shown in the right side of each figure. The photon energies used are 3.76 and 3.88 eV for TP and p-FTP, respectively. At the bottom of each panel, the TPPE spectrum of clean Cu(111) is shown. Each thick solid line indicates the low-energy cut-off for each photoemission spectrum. The Fermi edge is also indicated as a dashed line. Features A (surface state), B and B′ (new features) have binding energies of ~ 0.4, 0.16, and 0.14 eV, respectively. The details of the data are explained in the text.

As described in the experimental section, our use of TPPE permits the identification of the origin of a spectral feature as being either in the initial, intermediate, or final state of the TPPE process by means of a measurement of the electron energy given by $E = E_k + \Phi + E_F$ *versus* the photon energy $E_{h\nu}$, where E_k is the photoelectron kinetic energy, E_F is the Fermi level, and Φ is the work function. In particular, the slope of the shift in the peak of a spectral feature *vs* photon energy, *i.e.*, $dE/dE_{h\nu}$, is used to determine the nature of the feature. For example, prior measurements have shown $dE/dE_{h\nu} = 2$ from the clean Cu(111) surface state due to the fact that this state lies below the Fermi level. Figure 4.3 shows such a measurement for the case of the 0.16 eV peak using TPPE with $E_{h\nu}$ = 3.66, 3.76, 3.88, and 3.99 eV. Thus in this case the measurement also showed a slope of 2 indicating that the peak is associated with an occupied state.

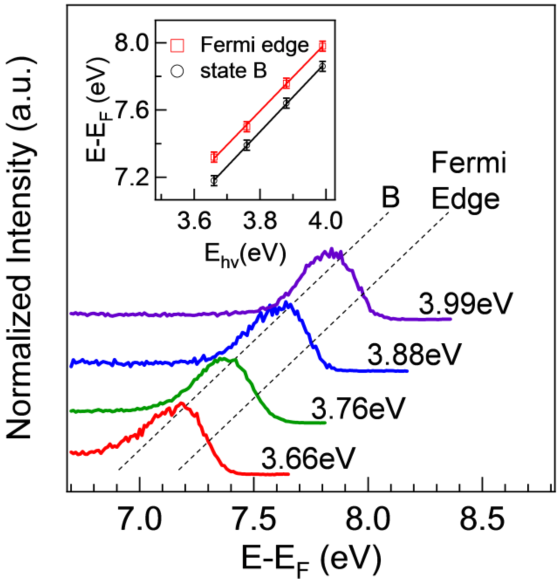

Figure 4.3 TPPE spectra of TP/Cu(111) with different photon energies ($E_{h\nu}$= 3.66 - 3.99 eV). Dashed lines indicate shifts of peak B (left) and the Fermi level (right). The amount of peak shift is, to within error, $2\Delta E_{h\nu}$, as shown in the inset.

4.3.2 Angle-resolved measurements of spectra

The angle-resolved capability of TPPE system was also used to determine the dispersion, *i.e.*, *E vs.* $k_{\|}$, of the features B (TP) and B′ (p-FTP). The results from this measurement for TP are shown in the data of Fig. 4.4(a). This measurement was done at an exposure time of 140 s to minimize the contribution of the bare Cu surface state, *i.e.*, at a coverage for which the bare surface state is fully extinguished. Angle-resolved photoemission spectra were also measured (not shown here, see *Supporting Information*) for p-FTP at lower exposure time (60 s). Also shown in Fig. 4.4(b) are basic fits to the data based on the assumption that it has a parabolic dependence of E vs $k_{||}$; the fits showed an effective mass of $m^* \sim 3.5\pm0.5\ m_e$ for TP and $3.9\pm1.4\ m_e$ for p-FTP, where m_e is the electron mass. Clearly this effective mass is much greater than that of the surface state ($m^* = 0.5\pm0.1\ m_e$) of bare Cu(111) as shown in Fig. 4.4. Note however, that this parabolic fit is less satisfactory for the data at larger values of $k_{||}$. In fact a better fit is obtained if a simple harmonic dependence is assumed for the dispersion as shown in the inset of Fig. 4.4(b). This fit suggests that there is backfolding of this occupied state at $k_{||} > 0.2$ Å^{-1}. This important point will be discussed below. Recently, similar backfolding behavior was also seen for a periodic coupled quantum well structure or superlattice for Cu(111) covered by a periodic adsorbate-molecule structure.[27] In that prior work, it was concluded that the adsorbate molecules localized the surface electrons.

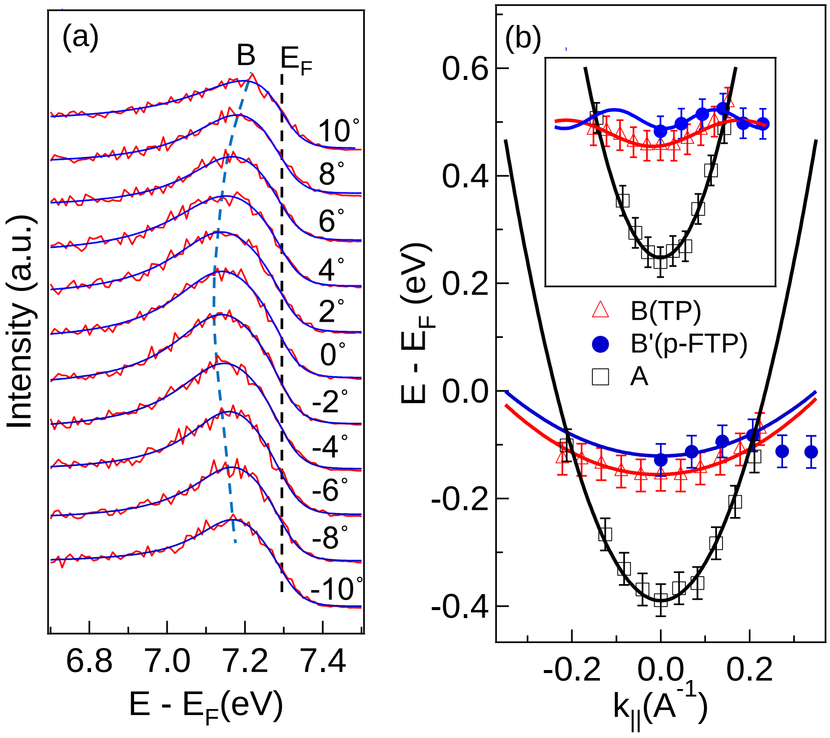

Figure 4.4 (a) Angle-resolved TPPE spectra around peak B with $E_{h\nu}$ = 3.65 eV. The detector angle is shown on the right side. The dashed blue and black guide lines indicate peak B and the Fermi edge, respectively. (b) The dispersion curves of peak B for TP and p-FTP. Also the dispersion of surface state (A) on the bare surface is also shown for comparison. The photoelectron parallel momenta in the *x*-axis are obtained from the measured detector angle using Eq. 3. The inset shows a periodic potential fit for B and B′. The data were collected at an exposure time of 150 s for TP and 60 s for p-FTP, respectively.

4.3.3 TPPE spectroscopy of TP at high coverage

The goal of this chapter is to examine the *low-coverage* comparative behavior of our two benzene thiols, which have opposite dipole orientation. However, since there has been one previous report[28] of the TPPE spectral of TP on a Cu(111) surface *at high coverage*, we made an initial measurement of this spectra of this system at high exposure so as to provide useful cross check on the consistency of our system with that of Ref. 28. Our measurement was made at a photon energy of 3.76 eV, since it was relatively close to that used in the reference, and employed a series of exposures equal to or longer than 150 s. Note also this high-coverage data shows no traces of the features (discussed above) observed at low-coverage. The most prominent and best defined feature in the data is a peak at 6.75 eV above the Fermi level, although a smaller feature is also noticeable at 6.91 eV. (see the inset of Fig. 4.5) The absolute energy and separation of the 6.75 eV and 6.91 eV peaks are very close to those in Ref. 28. Finally, based on the measurements of kinetic energy *vs.* photon energy by us and Ref. 28, these two observed states are assigned to a final state at 6.75 eV and an intermediate state at 3.16 eV, respectively.

Note that while these states are of interest here as an important consistency check with earlier measurements in Ref. 28, their assignments are of interest in their own right. Thus, Ref 28 revealed that both states appear to exhibit σ symmetry and their energetic locations are nearly independent of the length of hydrocarbon chain. The origins of both states were initially attributed to σ^*_{CuS} and a combination of σ^*_{CS} and π^*_{CuS} based on *ab initio* simulations[28]; however, this assignment has apparently come into question as a result of other photoemission studies, which found another unoccupied state at 1.2~1.6 eV that was attributed to an atomic S or thiol/metal interface bond.[16, 29-31] Those studies also suggest that there may well be a similar unoccupied state at TP/Cu(111) interface even though we cannot discern it due to the fact that the state is imbedded in an energy range filled with secondary electrons. Careful spectroscopic measurements are desirable to clarify the existence of unoccupied state at a lower-energy level. Also we want to point out another possible origin of the 3.16 eV feature rather than that of a molecular state. Recent TPPE studies on alkanethiol/Au(111) found an image-like interface state below the vacuum level.[32] This state was also found to be independent of the hydrocarbon group as well. Its effective mass was found to be close to free-electron mass and Ref. 28 also reported that 3.16 eV is dispersive even though the data is not shown. Thus, further experimental and theoretical studies are necessary to fully understand the origin of this state.

Note that in addition to these unoccupied states, we observed another final state at ~6.13 eV above the Fermi level. Using the measurements of kinetic energy versus photon energy data, we confirmed that this state is an occupied state with a binding energy of 1.4 eV. This state is known to arise from an antibonding orbital of the Cu-S bond; see, for example, the case of S/Cu(100)[31] and the case of methanethiol/Cu(100)[33] both at similar energies.

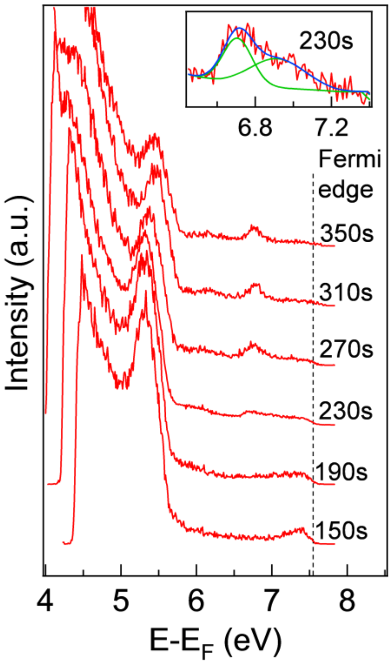

Figure 4.5 TPPE spectra on TP/Cu(111) at a series of high coverage values of adsorbate molecules taken at a photon energy of 3.76 eV. This series of spectra were collected for the different exposure times shown on the right side of the panel. The dashed line indicates the Fermi edge. The inset shows a two-peak fitting of the spectrum taken at an exposure time of 230 s.

4.4 Discussion

4.4.1 Prior work on thiols on Cu(111) or related Cu surfaces

Because of the importance of thiols in forming prototypical self-assembled monolayers, there have been extensive experimental and theoretical studies probing the detailed interfacial chemistry of these molecules, adsorbed on Cu surfaces.[11, 13, 18, 22-25, 28, 31, 33-37] For example, in the case of TP and p-FTP, NEXAFS studies of those molecules on Cu(100) surface revealed that the tilt angles of TP and p-FTP were 21° and 25° from the surface normal for 1 ML coverage, respectively.[25] For TP/Cu(111), earlier angle-resolved UPS studies showed that the orientation of TP was perpendicular or nearly-perpendicular at full coverage.[24] By comparison, more recent detailed studies of the surface structure of TP and p-FTP were conducted by Wong, *et* al.[23] They used low-temperature STM and DFT to reveal the lattice structure and orientation of TP, p-FTP, and other halogenated TPs on Cu (111). In particular, they found that when the coverage was sufficiently low, *e.g.*, at 0.25 ML, TP was found to lie in a flat geometry, whereas at ~1 ML it was aligned vertically. In particular, the tilt angle of TP was 65° from the surface normal at low coverage. This same group also showed that the lateral interaction of halogenated TPs led to a different self-assembled structure at low coverage. In addition, other DFT studies for TP monolayers on Cu(111) showed that the tilt angle was along the surface normal.[36]

In contrast to the more numerous chemical and surface-structure studies of intact TP and other thiols on Cu(111), there are fewer studies of the electronic structure at <1ML and the coverage dependence and electronic-state assignment appears not to have been examined. Thus, Vondrak *et al.* used TPPE to examine the unoccupied-state structure of a full monolayer of TP plus other alkanethiols on Cu(111).[28] Their measurements of the TP surface were carried out under full-coverage conditions and are discussed in more detail below. While electronic-structure studies with benzenethiols have not been extensive, there have been several measurements, which have observed the electronic structure and coverage-dependent shifts of benzene[38-40] and other organic species including strongly periodic systems on Cu(111)[27] and other metals.[41-43] Of particular interest have been observation of low-coverage shifts of the Cu(111) surface state[39] and image states[38] upon adsorption of these species. In addition, as mentioned above, strong backfolding was observed for an adsorbate system having a periodic surface arrangement.[27] These observations are commented on in more detail below.

4.4.2 Work function variation with coverage

One of our most striking observations is the strong change in the low-energy cutoff with coverage that is observed for both TP and p-FTP at low coverage as shown in Fig. 4.2, as well as the fact that this behavior occurs with opposite polarity for each of the two molecules. This shift in low-energy cutoff can be related to a more fundamental quantity, the change in work function, by using the fact that for TPPE, the work function is given by $\Phi = 2h\nu - (E_F - E_{LC})$, where E_F and E_{LC} are the Fermi edge and the low-energy cutoff in the TPPE spectra, respectively.[17, 44]

Using the above relation, we plot the coverage-dependence of the work function for surfaces covered with one of the two different molecules as a function of exposure in Fig 4.6(a). The horizontal axis is the exposure time of the molecules. In addition to this axis, we have provided an auxiliary scale showing the approximate coverage obtained with this exposure. Use of the data in Ref. 23 allows us to calibrate the curve of work function *vs.* exposure. In particular this and other studies by the same group showed that upon adsorption at low-coverage, p-FTP initially forms a loosely packed honeycomb structure of face-down molecules. However a further increase in coverage leads to a denser structure with higher coverage of the face-down phase. The observations for second or denser ‘lying-down’ phase and our measurements of the coverage dependence of the work function allow us to estimate the coverage using a plot based on the first-order adsorption kinetics. Our estimation of coverage relies on the assumption that the work function is proportional to coverage. This assumption is valid only for low coverage because depolarization effects, which result in a sublinear dependence with coverage, are then much less pronounced as has recently been shown, for example, by the Monti Group .[6] *Calculations are presented* in the *Supporting Information. For both molecules,* the change of work function with coverage is nearly identical up to at 0.4~0.5 ML. At this point, both systems exhibit an inflection point in their coverage-*vs.*-work-function plot and then diverge with slopes of opposite polarity as the coverage further increases. Note that near the inflection point (50-110 s) for the TP and the p-FTP curves, the slope of the graph is close to zero.

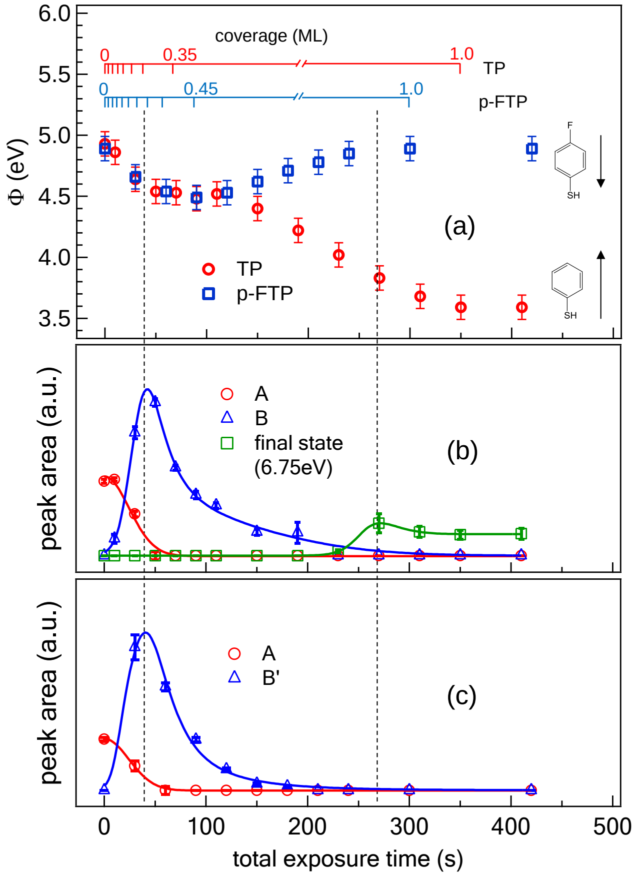

Figure 4.6 (a) Measured work function as a function of the total exposure time of TP (red circle) and p-FTP (blue square) on Cu(111). Auxiliary scales at the top of the figure show the approximate coverage for a given exposure. The inflection point of both curves appears at ~100s. The plateau at ~270s indicates the saturation of the coverage of the adsorbed molecules on the substrate. TP and p-FTP are drawn as an inset with arrows indicating the dipole projected along the 1-4 molecular axis. (b, c) The peak areas of the surface state (A, red circle), the new feature (B or B′, blue triangle), and the final state at 6.75eV (green square) as a function of total exposure time of TP (b) and p-FTP (c) on Cu(111). The data points for each state were connected by a guide to the eyes for better visibility. The dashed lines were drawn to indicate the alignment of similar features between graphs.

These observations regarding work function change can be understood by considering a simple model used in a recent study of benzenethiols on a Cu(100) surface, which examined how these and other loosely related molecules alter the work function of the Cu surface.[25] A similar approach has also been applied in other studies using alkanethiol and fluoroalkanethiols.[45, 46] In this approach, the molecular component of the overall surface work function is approximated as having a contribution from the projected molecular dipole onto the surface normal plus a dipole polarization due to the molecular bond. This molecular bond dipole includes charge redistribution, a "push-back" effect due to Pauli repulsion, and other possible effects upon formation of a chemisorbed bond by the adsorbate. As with other groups who have employed this simple description, we do not take into account the electrostatic interaction between the dipoles, which may reduce (depolarize) the effective dipole moment per molecule at higher coverage.[47] In the case of TP and other thiols, STM studies have shown that at low coverage, these molecules are known to have a supine or lying-down geometry and thus their dipole projection normal to the surface is then very small and at low coverage the bond-dipole contribution is then dominant. However, as the coverage increases, the adsorbate begins to assume its standing-up phase; thus at high coverage the molecular dipole contribution becomes important.

Hence, the behavior in Fig. 4.6 is related to the phase transition from a supine to a standing-up orientation. If the orientation of the two molecules was not fully supine, the two curves would not be coincidental in the first part of the curve, since for a supine molecule there is no molecular component perpendicular to the surface and thus the work function depends chiefly on the bond dipole. Since the work function change in this region is due to the molecular density times the bond dipole, the work function change slows as the coverage saturates for near full coverage of molecules, which are oriented in the supine position. At this point in coverage, molecules then change their orientation to the vertical orientation and the surface concentration can then increase further. *Note that as pointed out by others, this process is known to involve surface domains rather than individual molecules.*[23] Subsequently, domains with standing-up conformation increase as the surface concentration of molecules also increase. In fact, prior STM studies showed the mixed-domain structure of standing-up and supine benzenethiols. After the inflection point, both curves begin to diverge, although the slope of the TP curve is a factor of ~ 1.6× that of p-FTP. In this region of the curve, the slope is sensitive to the change in the total surface dipole as well as the increase in surface concentration. Since the bond dipole of p-FTP is antiparallel to the normal component of intrinsic molecular dipole whereas that of TP is parallel, the total interface dipole consisting of these dipoles is smaller for p-FTP, thus making the slope for TP larger than that for p-FTP.

This simple model can be tested for quantitative internal consistency by using the known relationships between work function change and the two contributions to the surface dipole for each adsorbed molecule. In effect we obtain the total surface dipole/adsorbed molecule at 1ML coverage and then extract out the dipolar contribution from the bond dipole/molecule, which to first order is not coverage dependent. This can then be used to predict the work function at the inflection point, *i.e.*, 0.4-0.5ML, for which coverage the molecules are still dominantly in the supine position and thus the molecule contribution to the adsorbate dipole will be negligible. Thus based on the Helmholtz equation, the change in the work function at 1ML can be related to the adsorbate surface coverage and the normal component of the total adsorbate dipole,

$$\Delta\Phi = -\,ne\mu_{\mathrm{ads},\perp}\big/\varepsilon_0\ , \tag{4.2}$$

where n is the surface density of the adsorbate dipoles and ε_0 is the vacuum permittivity. n can be derived from thiol studies on Cu(100). We use the value of n from known value for Cu(100) because the surface packing density of the erect thiols is governed by the thiol molecular size (see *Supporting Information*). Then using Eq. 4.2, the effective adsorbate polarization/adsorbate molecule is estimated to ~0.68 D and ~0 D for TP and p-FTP, respectively.

$$\mu_{\mathrm{ads},\perp} = \mu_{0,\perp} / \varepsilon_{eff} + \mu_{BD}. \tag{4.3}$$

This equation has been used successfully for the case of benzenethiols on a Cu(100) surface.[25] The molecular dipoles, *i.e.*, $\mu_{0,\perp}$ = 0.97D or $\mu_{0,\perp}$ = −0.78D for TP or p-FTP are estimated from simulation data in Ref. 25 and orientation angles given in by Ref 37. We set ε_{eff} = 2.94 for the two molecules, a reasonable assumption given that the molecules considered by us have the same polarizability as those in Ref. 25. Inserting $\mu_{\mathrm{ads},\perp}$ and $\mu_{0,\perp}$ into Eq. 4.3 for the two molecular species, we obtain a value of μ_{BD} for both molecular species of 0.31 D. Recalling that due to the supine molecule orientation at low coverage we can neglect the molecular dipole contribution, the work function change at the inflection point, with $n \sim 2 \times 10^{14}$ cm^{-2}, is then estimated using Eq. 4.2 to be ~ −(0.23 - 0.28) eV; this value can be compared to our experimental value of ~ −0.4eV.

The difference between the model calculation and experimental data can be attributed to the simplicity of the model used here, including the multiple assumptions for the model calculation, such as surface density of molecule, dielectric constant, tilt angle of benzene group, etc. One particularly important assumption in the model is that the bonding dipole is independent of coverage. This assumption may not be rigorously true. For example a recent theoretical study showed that the bond dipole of thiolate SAM is significantly affected by packing density even without taking into account a change in orientation.[47] In addition, since the benzene group is proximate to the surface at low coverage it will also to some extent influence the surface polarization.[38, 40] This effect together with the electrostatic dipole-dipole interactions are obviously not accounted for in our model. However while the model used here is approximate, it is clear that it does describe at least the dominant physics involved.

4.4.3 Identification and nature of the new state near −0.15 eV

The state located at a binding energy of 0.16 ± 0.08 eV is the most prominent low-binding-energy spectral feature of TP on Cu(111). Our measurement of the variation of kinetic energy with wavelength shows that it is an occupied initial state. The same feature with the slightly different binding energy of 0.14 ± 0.04 eV was also measured in our experiments for adsorbed p-FTP. These two states appear not to have been commented on or even observed in any prior theoretical or experimental work: in fact, recent photon photoemission studies on thiol/Cu (or the closely related Au system) have found HOMO and LUMO levels located < −1 eV and > 1 eV from the Fermi level, respectively.[18, 31, 33, 48-51] The additional distinctive characteristics of the −0.15 eV state are, first, that it is a spatially localized or very weakly dispersive state, as is shown *via* our angular-resolved measurements; this behavior is in contrast with the strongly dispersive nature of the usual clean Cu(111) surface state. Second its photoemission intensity is found to rise and then decrease with coverage over the range of 0-0.5 ML, *i.e.*, at low coverage. Examination of the data shows the appearance of this state is clearly associated the deposition of TP on the surface, while its disappearance occurs after ~0.4-0.5 ML, *i.e.*, the same coverage at which the TP begins to shift out of its supine position. The binding energy of this TP state (as well as, *mutatis mutandis*, its p-FTP analog) is constant within experimental error at 0.1-0.3ML coverage where this state is particularly prominent.

To identify this state, we consider two possible origins of the feature, including 1) a chemisorbed bond, which changes with surface phase or, more particularly, surface orientation or 2) a quantum-confined Cu surface state.

The first possible origin is that the state for either TP or p-FTP is a chemisorbed state that is only present at low coverage, *i.e.*, at < 0.4-0.5 ML. This low binding-energy state is not seen for a coverage of > 0.5 ML (see Fig. 4.2), a coverage which has been shown *via* STM studies[23] to be above that for which the molecule assumes a vertical geometry. Thus, this chemisorbed state would have to be identified with the supine orientation of the benzene thiols. Further note that no evidence of the state is seen at high, *i.e.*, ~1 ML, coverage since the only states measured are, for TP, an unoccupied state energy of 6.75 eV and for p-FTP an unoccupied state at 8.65 eV (not shown, see *Supporting Information*) for our data and data in Ref. 28 as well as an occupied state at −1.4eV. Of course one must also consider if a change in surface phase, *i.e.*, molecular orientation in our case, could shift the binding energy of the 1.4 eV state to 0.16 eV between low and high coverage. However, there appears to have been no earlier examples of the change in S-metal surface bond energy with ligand orientation for thiols – although there has been at least tentative observation of this technique for thiophene.[17] Moreover, our experiments show clear evidence that the −0.15 eV state originates from the Cu surface state rather than chemisorbed states between the Cu and adsorbate while the rise of −0.15 eV state signal occurs simultaneously with a reduction in the surface state signal, whereas the three chemisorbed states just mentioned begin to show up after the −0.15 eV state becomes undetectable. This observation is consistent with the fact that −0.15 eV state was not observed in UPS studies of TP/Cu(100) system, for which the Shockley surface state is not present.[18] We thus conclude that it is unlikely that the –0.15 eV states would originate from any distinct, low-coverage, chemisorbed bond.

A more likely and experimentally consistent origin of behavior 0.15 eV state and its behavior in Figs. 4.2, 4.4, and 4.6 lies in the effect of a new of adsorbate molecules on the otherwise delocalized electron in the Cu(111) *sp* surface state. Such surface impurities can place lateral potential barriers throughout the surface, which can lead to confinement of the normally delocalized surface-state electron, and thus alter its binding energy. Such confinement shifts have been seen previously on surfaces having simple surface-structure-confined Cu(111) surface electrons.[52] For example, it is well known that on regularly stepped Cu(111), prepared from a vicinal surface, binding-energy shifts in surface electrons are seen due to confinement of the electron by ~10's of Angstrom-wide steps. Thus in Ref. 53, Wang *et al.* showed that with a simple 1-dimensional Kronig-Penney model, the surface state energy shifts upward (decreasing binding energy) by about 200 meV as the terrace length decreased from infinite (flat surface) to ~ 7.4 Å due to electron confinement. In addition, confinement effects have also been observed in a striped phase of O/Cu(110).[53]

In addition, and perhaps more to the point, there have been several prior studies of the confinement of the Cu(111) surface-state electron in the presence of adsorbate atoms or molecules. These studies include early theoretical work by Hormandinger and Pendry,[54] which developed a theoretical framework for adsorbate-induced surface-state-electron localization. This theoretical treatment related the confinement shift to the adsorbed-molecule-induced potential barriers. A more-recent *experimental* study used ARPES to show that a small, *i.e.*, 0.1 ML, addition of CO on the Cu(111) surface caused an decrease in the binding energy by 0.15 eV.[55] A second study, using benzene on Cu(111) along with a TPPE measurement, has shown a shift of the same magnitude.[39] Thus the shifts in these cases are typically within 100s of meV of the original bare-surface binding energy below the Fermi level, a magnitude close to the values measured in our wavelength-dependent photoemission data shown in Fig. 4.2. Finally, a third very relevant and elegant study used a 2D molecular surface lattice formed by adsorption of dehydrogenated 4,9-diaminoperylene-quinone-3,10-diimine onto a Cu(111) surface to demonstrate that a lateral surface superlattice of the Cu surface electron could be formed.[27] The coupling within the superlattice was found to be weak thus yielding well defined quantum wells. ARPES measurements showed a small electron dispersion and backfolding by the Brillouin zone of the surface lattice. The dispersion was fit by a near sinusoidal dispersion as would be expected by a periodic confinement potential.

In our TP- and p-FTP-dosed surface, the most substantial surface molecule interaction would be *via* the S-metal bonding in adsorbate islands; in fact, some experiments have suggested that the benzene ring moieties are not in contact with the Cu surface[23] and thus would not present any substantial surface potential modulation. The S surface bond would be sufficiently disruptive that it is likely to form a surface barrier. In addition, these prior STM studies have shown that regular arrays of p-FTP are imaged on low coverage surfaces at 80 K.[23] In the case of TP-dosed surfaces, the molecular surface ordering is not as regular; nonetheless, STM imaging does show persistent patterns of centered hexagonal structures under closely related conditions. Our TPPE measurements are consistent with surface confinement by a regular array. Thus for both molecules, clear evidence for backfolding is seen in the angle-resolved measurement of the dispersion. Given the more pronounced surface ordering seen in p-FTP, it is not surprising that the adsorbate structure causes a larger energetic shift and stronger localization than does TP, as shown in Fig. 4.2. Further note that the unit cell of 0.18 Å^{-1} reported for p-FTP[17] agrees well with the backfolding wavenumber of 0.21 $\pm 0.03\text{Å}^{-1}$ seen in our data in Fig. 4.5.

Thus our observed TPPE data is supportive of confinement being the source of the −0.15 eV state for TP and p-FTP. In particular, the fact that this spectral feature has the same spectral density as the unconfined electron state is consistent with a simple fixed confinement being the origin of this spectral feature. In addition, the fact that the new states show weak dispersion with a folded zone, which for the case of p-FTP is consistent with the known period, is also consistent with state being strongly confined.

Finally we note that it appears surprising that there is no signature of the final states, *i.e.*, those with energies of 6.75 and 6.91 eV, *at low coverage* and which are only detected at exposures close to saturation; see Fig. 4.6. While we do not have a definitive explanation of this observation, we note photoemission from molecules in a supine position or in a state of disorder might be expected to have a different, including much reduced, photoemission signature that those in an upright position. Clearly this phenomenon will require additional studies for a definitive answer.

4.5 Conclusion

The goal of our work has been to develop an understanding of how low coverage of benzenethiols on Cu(111) affects electronic structure of the molecule-metal interface. Our first observation is that adsorption alters the surface polarization of the interfacial layer. Our results show that at low coverage the formation of an adsorbate metal bond provides the dominant source of polarization and as the coverage increases the change in adsorbate geometry to an upright geometry further shifts the surface dipole layer and hence the surface polarization. In addition, our results also show the importance of molecule-based surface confinement of the Cu surface electrons in altering their energetic location and dispersion of this surface band. The

Umklapp features measured are in accord with earlier STM measurements of surface structure of these two adsorbates.

References

1. Koch, N., Organic Electronic Devices and Their Functional Interfaces. *ChemPhysChem* **2007**, *8*, 1438-1455.
2. Ishii, H.; Sugiyama, K.; Ito, E.; Seki, K., Energy Level Alignment and Interfacial Electronic Structures at Organic/Metal and Organic/Organic Interfaces. *Adv. Mater.* **1999**, *11*, 605-625.
3. Heimel, G.; Romaner, L.; Zojer, E.; Bredas, J.-L., The Interface Energetics of Self-Assembled Monolayers on Metals. *Acc. Chem. Res.* **2008**, *41*, 721-729.
4. Kahn, A.; Koch, N.; Gao, W., Electronic Structure and Electrical Properties of Interfaces between Metals and π-Conjugated Molecular Films. *J. Polym. Sci., Part B: Polym. Phys.* **2003**, *41*, 2529-2548.
5. L'vov, V. S.; Naaman, R.; Tiberkevich, V.; Vager, Z., Cooperative Effect in Electron Transfer between Metal Substrate and Organized Organic Layers. *Chem. Phys. Lett.* **2003**, *381*, 650-653.
6. Monti, O. L. A.; Steele, M. P., Influence of Electrostatic Fields on Molecular Electronic Structure: Insights for Interfacial Charge Transfer. *PCCP* **2010**, *12*, 12390-12400.
7. Love, J. C.; Estroff, L. A.; Kriebel, J. K.; Nuzzo, R. G.; Whitesides, G. M., Self-Assembled Monolayers of Thiolates on Metals as a Form of Nanotechnology. *Chem. Rev.* **2005**, *105*, 1103-1170.

8. Aqua, T.; Cohen, H.; Sinai, O.; Frydman, V.; Bendikov, T.; Krepel, D.; Hod, O.; Kronik, L.; Naaman, R., Role of Backbone Charge Rearrangement in the Bond-Dipole and Work Function of Molecular Monolayers. *J. Phys. Chem. C* **2011**, *115*, 24888-24892.

9. Camillone III, N.; Chidsey, C. E. D.; Liu, G.-y.; Scoles, G., Superlattice Structure at the Surface of a Monolayer of Octadecanethiol Self-Assembled on Au(111). *J. Chem. Phys.* **1993**, *98*, 3503-3511.

10. Camillone III, N.; Khan, K. A.; Osgood Jr, R. M., The Thermal Chemistry of Model Organosulfur Compounds on Gallium Arsenide (110). *Surf. Sci.* **2000**, *453*, 83-102.

11. Jackson, G. J.; Woodruff, D. P.; Jones, R. G.; Singh, N. K.; Chan, A. S. Y.; Cowie, B. C. C.; Formoso, V., Following Local Adsorption Sites through a Surface Chemical Reaction: CH_3SH on Cu(111). *Phys. Rev. Lett.* **2000**, *84*, 119-122.

12. Nuzzo, R. G.; Zegarski, B. R.; Dubois, L. H., Fundamental Studies of the Chemisorption of Organosulfur Compounds on Gold (111). Implications For Molecular Self-Assembly on Gold Surfaces. *J. Am. Chem. Soc.* **1987**, *109*, 733-740.

13. Zhou, J.-G.; Williams, Q. L.; Hagelberg, F., CH_3SH Molecules Deposited on Cu(111) and Deprotonation. *Phys. Rev. B* **2008**, *77*, 035402.

14. Poirier, G. E.; Pylant, E. D., The Self-Assembly Mechanism of Alkanethiols on Au(111). *Science* **1996**, *272*, 1145-1148.

15. Lindstrom, C. D.; Muntwiler, M.; Zhu, X. Y., Electron Transport Across the Alkanethiol Self-Assembled Monolayer/Au(111) Interface: Role of the Chemical Anchor. *J. Phys. Chem. B* **2005**, *109*, 21492-21495.

16. Miller, A. D.; Gaffney, K. J.; Liu, S. H.; Szymanski, P.; Garrett-Roe, S.; Wong, C. M.; Harris, C. B., Evolution of a Two-Dimensional Band Structure at a Self-Assembling Interface. *J. Phys. Chem. A* **2002**, *106*, 7636-7638.

17. Zhou, J.; Yang, Y. X.; Liu, P.; Camillone, N.; White, M. G., Electronic Structure of the Thiophene/Au(111) Interface Probed by Two-Photon Photoemission. *J. Phys. Chem. C* **2010**, *114*, 13670-13677.

18. Di Castro, V.; Bussolotti, F.; Mariani, C., The Evolution of Benzenethiol Self-Assembled Monolayer on the Cu(100) Surface. *Surf. Sci.* **2005**, *598*, 218-225.

19. Lindsay, S. M.; Ratner, M. A., Molecular Transport Junctions: Clearing Mists. *Adv. Mater.* **2007**, *19*, 23-31.

20. Bock, C.; Pham, D. V.; Kunze, U.; Kafer, D.; Witte, G.; Woll, C., Improved Morphology and Charge Carrier Injection in Pentacene Field-Effect Transistors with Thiol-Treated Electrodes. *J. Appl. Phys.* **2006**, *100*, 114517-7.

21. Jiang, P.; Deng, K.; Fichou, D.; Xie, S.-S.; Nion, A.; Wang, C., STM Imaging *ortho*- and *para*-Fluorothiophenol Self-Assembled Monolayers on Au(111). *Langmuir* **2009**, *25,* 5012-5017.

22. Kwon, K.-Y.; Pawin, G.; Wong, K. L.; Peters, E.; Kim, D.; Hong, S.; Rahman, T. S.; Marsella, M.; Bartels, L., H-Atom Position as Pattern-Determining Factor in Arenethiol Films. *J. Am. Chem. Soc.* **2009**, *131*, 5540-5545.

23. Wong, K. L.; Lin, X.; Kwon, K. Y.; Pawin, G.; Rao, B. V.; Liu, A.; Bartels, L.; Stolbov, S.; Rahman, T. S., Halogen-Substituted Thiophenol Molecules on Cu(111). *Langmuir* **2004**, *20*, 10928-10934.

24. Agron, P. A.; Carlson, T. A., Angular Resolved UPS and XPS Spectra of Benzenethiol Adsorbed on Cu(111) at 300K. *J. Vac. Sci. Tech.* **1982**, *20*, 815-817.

25. Schmidt, C.; Witt, A.; Witte, G., Tailoring the Cu(100) Work Function by Substituted Benzenethiolate Self-Assembled Monolayers. *J. Phys. Chem. A* **2011**, *115*, 7234-7241.

26. Hengsberger, M.; Baumberger, F.; Neff, H. J.; Greber, T.; Osterwalder, J., Photoemission Momentum Mapping and Wave Function Analysis of Surface and Bulk States on Flat Cu(111) and Stepped Cu(443) Surfaces: A Two-Photon Photoemission Study. *Phys. Rev. B* **2008**, *77*, 085425.

27. Lobo-Checa, J.; Matena, M.; Müller, K.; Dil, J. H.; Meier, F.; Gade, L. H.; Jung, T. A.; Stöhr, M., Band Formation from Coupled Quantum Dots Formed by a Nanoporous Network on a Copper Surface. *Science* **2009**, *325*, 300-303.

28. Vondrak, T.; Wang, H.; Winget, P.; Cramer, C. J.; Zhu, X. Y., Interfacial Electronic Structure in Thiolate Self-Assembled Monolayers: Implication for Molecular Electronics. *J. Am. Chem. Soc.* **2000**, *122*, 4700-4707.

29. Föhlisch, A.; Feulner, P.; Hennies, F.; Fink, A.; Menzel, D.; Sanchez-Portal, D.; Echenique, P.; Wurth, W., Direct Observation of Electron Dynamics in the Attosecond Domain. *Nature* **2005**, *436*, 373-376.

30. Nakaya, M.; Shikishima, M.; Shibuta, M.; Hirata, N.; Eguchi, T.; Nakajima, A., Molecular-Scale and Wide-Energy-Range Tunneling Spectroscopy on Self-Assembled Monolayers of Alkanethiol Molecules. *ACS Nano* **2012**, *6*, 8728-8734.

31. Leschik, G.; Courths, R.; Wern, H., Electronic Structure Investigation of Cu(001)-p(2 × 2) S Using Angle-Resolved Photoemission and Inverse Photoemission. *Surf. Sci.* **1993**, *294*, 355-366.

32. Muntwiler, M.; Lindstrom, C. D.; Zhu, X. Y., Delocalized Electron Resonance at the Alkanethiolate Self-Assembled Monolayer/Au(111) Interface. *J. Chem. Phys.* **2006**, *124*, 081104-3.

33. Bussolotti, F.; Corradini, V.; Di Castro, V.; Grazia Betti, M.; Mariani, C., Electronic Structure of Methanethiolate Self-Assembled on the Cu (100) Surface. *Surf. Sci.* **2004**, *566*, 591-596.

34. Driver, S. M.; Woodruff, D. P., Scanning Tunnelling Microscopy Study of the Interaction of Dimethyl Disulphide with Cu(111). *Surf. Sci.* **2000**, *457*, 11-23.

35. Driver, S. M.; Woodruff, D. P., Adsorption Structures of 1-Octanethiol on Cu(111) Studied by Scanning Tunneling Microscopy. *Langmuir* **2000**, *16*, 6693-6700.

36. Perebeinos, V.; Newton, M., Electronic Structure of S–C_6H_5 Self-Assembled Monolayers on Cu(111) and Au(111) Substrates. *Chem. Phys.* **2005**, *319*, 159-166.

37. Schmidt, C.; Götzen, J.; Witte, G., Temporal Evolution of Benzenethiolate SAMs on Cu(100). *Langmuir* **2011**, *27*, 1025-1032.

38. Dougherty, D. B.; Maksymovych, P.; Lee, J.; Yates, J. T., Jr., Local Spectroscopy of Image-Potential-Derived States: From Single Molecules to Monolayers of Benzene on Cu(111). *Phys. Rev. Lett.* **2006**, *97*, 236806.

39. Munakata, T.; Sakashita, T.; Shudo, K.-i., Two-Photon Photoemission from Benzene Adsorbed on Cu(111). *J. Electron. Spectrosc. Relat. Phenom.* **1998**, *88–91*, 591-595.

40. Velic, D.; Hotzel, A.; Wolf, M.; Ertl, G., Electronic States of the C_6H_6/Cu 111 System: Energetics, Femtosecond Dynamics, and Adsorption Morphology. *J. Chem. Phys.* **1998**, *109*, 9155-9165.

41. Ziroff, J.; Gold, P.; Bendounan, A.; Forster, F.; Reinert, F., Adsorption Energy and Geometry of Physisorbed Organic Molecules on Au(111) Probed by Surface-State Photoemission. *Surf. Sci.* **2009**, *603*, 354-358.

42. Schwalb, C. H.; Sachs, S.; Marks, M.; Schöll, A.; Reinert, F.; Umbach, E.; Höfer, U., Electron Lifetime in a Shockley-Type Metal-Organic Interface State. *Phys. Rev. Lett.* **2008**, *101*, 146801.

43. Muller, E. A.; Johns, J. E.; Caplins, B. W.; Harris, C. B., Quantum Confinement and Anisotropy in Thin-film Molecular Semiconductors. *Phys. Rev. B* **2011**, *83*, 165422.

44. Cahen, D.; Kahn, A., Electron Energetics at Surfaces and Interfaces: Concepts and Experiments. *Adv. Mater.* **2003**, *15*, 271-277.

45. Alloway, D. M.; Hofmann, M.; Smith, D. L.; Gruhn, N. E.; Graham, A. L.; Colorado, R.; Wysocki, V. H.; Lee, T. R.; Lee, P. A.; Armstrong, N. R., Interface Dipoles Arising from Self-Assembled Monolayers on Gold: UV−Photoemission Studies of Alkanethiols and Partially Fluorinated Alkanethiols. *J. Phys. Chem. B* **2003**, *107*, 11690-11699.

46. Li, H.; Duan, Y.; Paramonov, P.; Coropceanu, V.; Brédas, J.-L., Electronic Structure of Self-Assembled Fluoromethylthiol Monolayers on the Au(111) Surface: Impact of Fluorination and Coverage Density. *J. Electron. Spectrosc. Relat. Phenom.* **2009**, *174*, 70-77.

47. Romaner, L.; Heimel, G.; Zojer, E., Electronic Structure of Thiol-Bonded Self-Assembled Monolayers: Impact of Coverage. *Phys. Rev. B* **2008**, *77*, 045113.

48. Whelan, C. M.; Barnes, C. J.; Walker, C. G. H.; Brown, N. M. D., Benzenethiol Adsorption on Au(111) Studied by Synchrotron ARUPS, HREELS and XPS. *Surf. Sci.* **1999**, *425*, 195-211.

49. Kim, B.; Choi, S. H.; Zhu, X. Y.; Frisbie, C. D., Molecular Tunnel Junctions Based on π-Conjugated Oligoacene Thiols and Dithiols between Ag, Au, and Pt Contacts: Effect of Surface Linking Group and Metal Work Function. *J. Am. Chem. Soc.* **2011**, *133*, 19864-19877.

50. Pasquali, L.; Terzi, F.; Seeber, R.; Doyle, B. P.; Nannarone, S., Adsorption Geometry Variation of 1,4-Benzenedimethanethiol Self-Assembled Monolayers on Au(111) Grown from the Vapor Phase. *J. Chem. Phys.* **2008**, *128*, 134711-10.

51. Rieley, H.; Price, N. J.; White, R. G.; Blyth, R. I. R.; Robinson, A. W., A NEXAFS and UPS Study of Thiol Monolayers Self-Assembled on Gold. *Surf. Sci.* **1995**, *331–333, Part A*, 189-195.

52. Wang, S. C.; Yilmaz, M. B.; Knox, K. R.; Zaki, N.; Dadap, J. I.; Valla, T.; Johnson, P. D.; Osgood, R. M., Jr., Electronic Structure of a Co-decorated Vicinal Cu(775) surface: High-Resolution Photoemission Spectroscopy. *Phys. Rev. B* **2008**, *77*, 115448.

53. Bertel, E.; Lehmann, J., Electronic Structure of Self-Organized Lateral Superlattices on a Metal Surface: O/Cu(110). *Phys. Rev. Lett.* **1998**, *80*, 1497-1500.

54. Hörmandinger, G.; Pendry, J. B., Interaction of Surface States with Rows of Adsorbed Atoms and Other One-Dimensional Scatterers. *Phys. Rev. B* **1994**, *50*, 18607-18620.

55. Baumberger, F.; Greber, T.; Delley, B.; Osterwalder, J., Tailoring Confining Barriers for Surface States by Step Decoration: CO /Vicinal Cu(111). *Phys. Rev. Lett.* **2002**, *88*, 237601.

Supporting Materials

Periodicity of the p-Fluorothiophenol (p-FTP) Honeycomb Structure

In order to obtain the periodicity of p-FTP we make use of angle-resolved photoemission (ARPES) data. Thus we notice first that the data in Fig. 4.4 show clear evidence of backfolding of the Brillouin zone. This data is then fit using a sine curve to find that the backfolded zone boundary is at $0.42Å^{-1}$. A similar fit can be made for the case of TP to give a backfolded zone boundary at $0.52Å^{-1}$. This value can be compared to data in Ref. 1, which showed STM images of p-FTP assemblies at low coverage. The periodicity of this structure was ~ 2nm. By using this data, we calculate the periodicity in k-space as follows: $|k_{||}| = 2\pi$ / (20Å *sin60)) = $0.36Å^{-1}$. This value is within 15% of the value obtained from photoemission. In the case of FP, there is no clear experimental measurement of periodicity; however *ab initio* calculations suggest values of the order measured in our experiment.

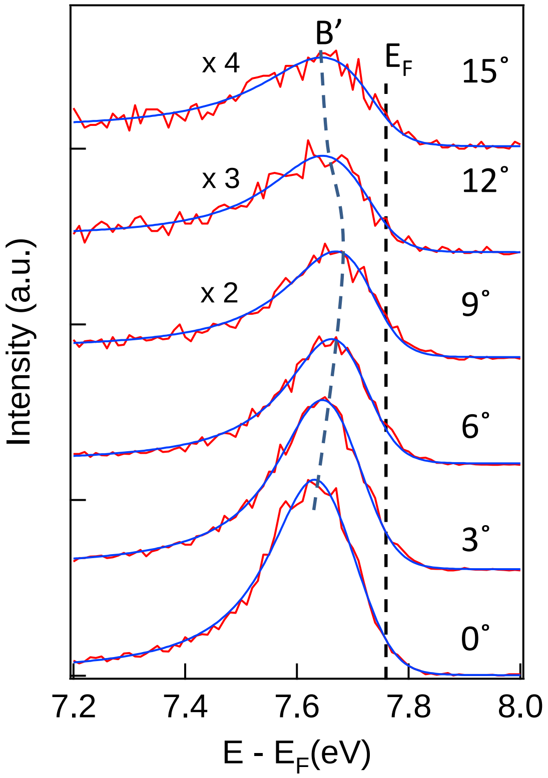

Figure 4.7 Angle-resolved TPPE spectra of p-FTP around peak B′ with $E_{h\nu}$ = 3.88 eV. The detector angle is shown on the right side. The dashed blue and black guide lines indicate peak B′ and the Fermi edge, respectively. The data were collected at an exposure time of 60 s. The spectra at higher angles are magnified for visibility. Data for FP and p-FTP are also shown in Fig.4 in the text.

Coverage Estimation

Use of the data in Ref. 1 allows us to calculate the coverage of TP or p-FTP in the low coverage regime. For example, when p-FTP adsorbates form a complete monolayer of face-down phase molecules, their area/molecule is 40.3 $Å^2$ (n_{mol}/n_{sub} = 0.14). By using area/molecule data, we can then obtain the coverage of face-down monolayer of p-FTP, ~ 0.48ML. Similarly the coverage of face-down monolayer of TP is ~0.38ML

Under conditions of low coverage, we estimate the adsorbate coverage using the data of workfunction *vs* exposure. Note that the value of the workfunction is a complex function of adsorbate density, depolarization, orientation, and other effects. However, for a loosely packed film at low coverage, adsorbate density is far more important than other factors. Therefore we fit our data until the inflection point using a first-order adsorption rate equation. If we assume $d\Theta/dt \sim c(1-\Theta)$ and ignore desorption, which is appropriate at T=300K for typical thiol layers on Cu (111) with $E_d \sim 0.8$eV, $\Theta(t) = 1-\exp(-ct)$, where c is a constant. The fitting of each adsorbate is shown in Fig. 4.8. The adsorption rate constant, c, is 0.041 s^{-1} and 0.032 s^{-1} for TP and p-FTP, respectively. Based on these results, we have added auxiliary axes in Fig. 4.6 that show the estimated coverage of each adsorbate.

An important additional quantity, which is needed for the calculation of coverage discussed above or in the self-consistent calculation of the workfunction is surface density at 1ML. As mention in the main text this density is set by the size of the molecule; that is prior studies have shown that the surface density is set by the maximum geometric packing density of the TP and p-FTP molecule. However, we also must obtain the density of full coverage for the standing-up phase. Unfortunately this quantity does not appear to have been measured and thus is not available in the literature; thus we instead rely on the known area/molecule of TP/Cu(100) data from Ref 2, 19.6Å^2, an approach which is valid given that molecular packing is set by the molecular size. This value is n =5.1 x 10^{14} cm^{-2}, a value corresponding to a molecular surface area of 19.6 Å^2 of TP,[2] for both cases. This area agrees closely with the cross-sectional area of the erect molecule. Note, in addition, other aromatic thiols have comparable molecular density (20-30 Å^2) when they form densely-packed, standing-up monolayers on metal substrates.[3-5] This argument suggests that the use of a Cu(111) substrate will lead to approximately the same molecular surface density as for a Cu(100) substrate.

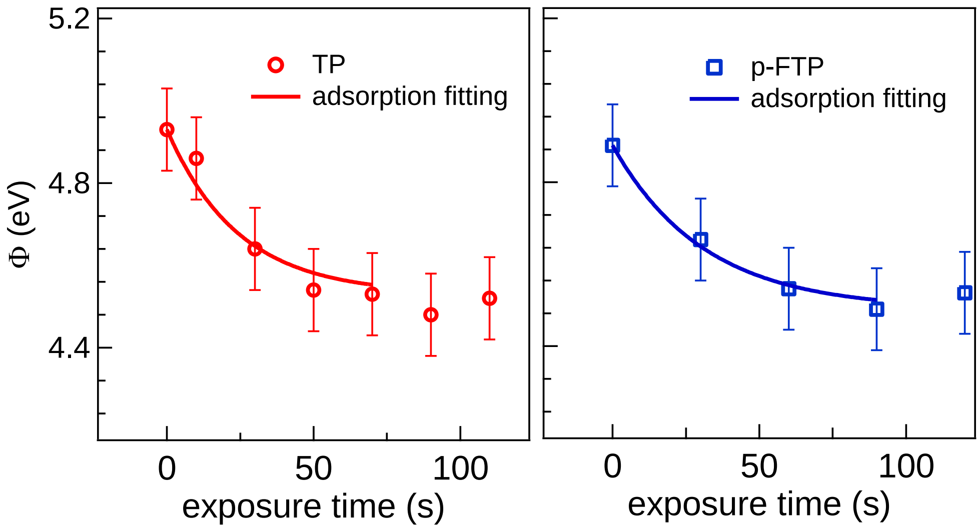

Figure 4.8 Work function as a function of the total exposure time of TP (a. red circle) and p-FTP (b. blue square) on Cu(111). Solid lines are obtained by fitting the dats to the adsorption rate equation for each adsorbate.

Photon Energy Dependence of TPPE Spectra at Full Coverage: TP

The photon-energy dependence in Fig. 4.9 allows us to assign C to an occupied state and D to a final state. The figure shows the TPPE spectra of TP/Cu(111) at three different photon energies ($E_{h\nu}$= 3.65, 3.76, 3.94 eV). Dashed lines indicate shifts of peak C (left), D (center), and the Fermi level (right). The amount of peak shift is, to within error, $2\Delta E_{h\nu}$ for C state and 0 for D state. As is discussed in the experimental section this dependence allows us to assign the states to occupied and unoccupied states, respectively.

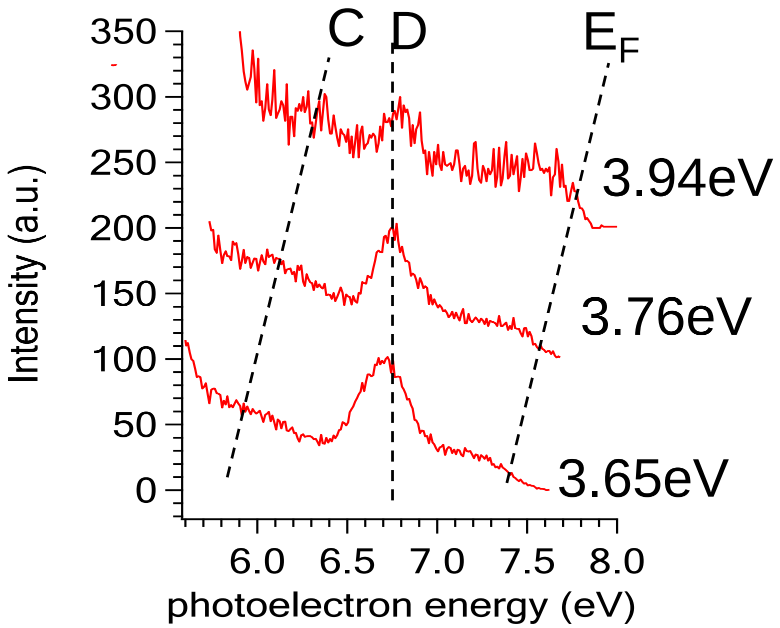

Figure 4.9 TPPE spectra of TP/Cu(111) with different photon energies ($E_{h\nu}$= 3.65, 3.76, 3.94 eV). Dashed lines indicate shifts of peak C (left), D (center), and the Fermi level (right). The amount of peak shift is, to within error, $2\Delta E_{h\nu}$ for C state and 0 for D state.

Photon Energy Dependence of TPPE Spectra at Full Coverage: p-FTP

Similarly the TPPE photon-energy dependence for p=TFP in Fig. 4.10 shows clearly the presence of an intermediate state G and a final state F. Thus the TPPE spectra of p-FTP/Cu(111) is shown for different photon energies over the range $E_{h\nu}$= 3.88~4.72 eV. The dashed lines indicate shifts of peak C (left), F, G (center), and the Fermi level (right). The amount of peak shift is, to within error, $2\Delta E_{h\nu}$ for the C state, 0 for F, $\Delta E_{h\nu}$ for the G state.

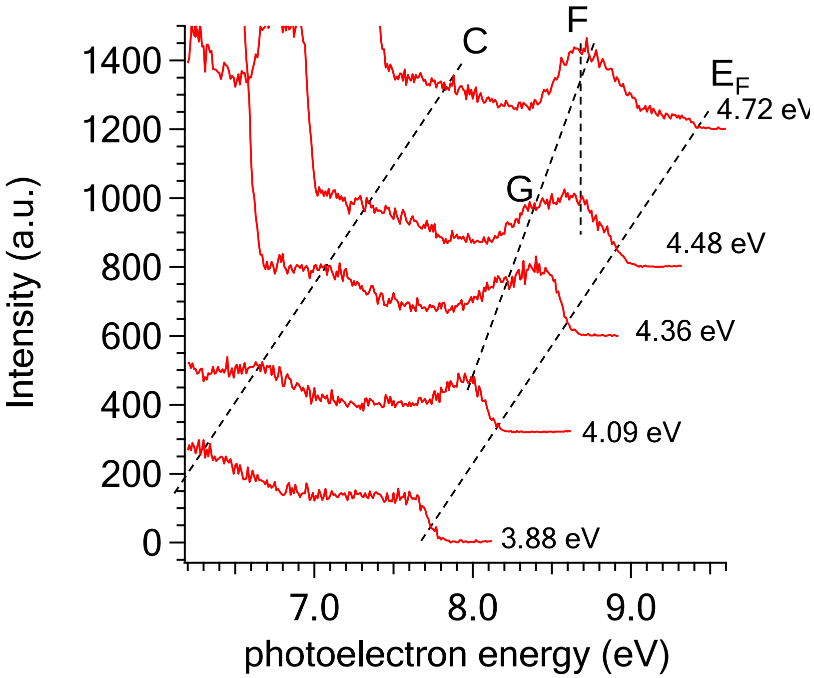

Figure 4.10 TPPE spectra of p-FTP/Cu(111) with different photon energies ($E_{h\nu}$= 3.88~4.72 eV). Dashed lines indicate shifts of peak C (left), F, G (center), and the Fermi level (right). The amount of peak shift is, to within error, $2\Delta E_{h\nu}$ for the C state, 0 for the F state and $\Delta E_{h\nu}$ for the G state.

Notes on the Dipoles of TP and p-FTP Used Here

An important side note is that that the dipoles of these two molecules are not completely parallel with the 1-4 axis of phenyl group. This off-axis behavior is due to the fact that the dipolar component of the SH bond form along the 1-4 phenyl axis. The adsorption of thiophenol on the copper surface breaks this bond and creates a symmetric form, thiophenolate. Therefore, as shown in Ref 2, we have used the projected dipole instead of the total dipole for quantitative analysis of adsorbate dipole in the discussion. Since the magnitude of dipole moments are 1.24 D for TP and 1.11 D for p-FTP based on a MP2 calculations, the projected dipoles onto surface normal are $\mu_{0,\perp} = 0.97$D for TP and $\mu_{0,\perp} = -0.78$D for p-FTP.

References for Supporting Materials

1. Wong, K. L.; Lin, X.; Kwon, K. Y.; Pawin, G.; Rao, B. V.; Liu, A.; Bartels, L.; Stolbov, S.; Rahman, T. S., Halogen-Substituted Thiophenol Molecules on Cu(111). *Langmuir* **2004**, *20*, 10928-10934.
2. Schmidt, C.; Witt, A.; Witte, G., Tailoring the Cu(100) Work Function by Substituted Benzenethiolate Self-Assembled Monolayers. *J. Phys. Chem. A* **2011**, *115*, 7234-7241.
3. Azzam, W.; Fuxen, C.; Birkner, A.; Rong, H.-T.; Buck, M.; Wöll, C., Coexistence of Different Structural Phases in Thioaromatic Monolayers on Au(111). *Langmuir* **2003**, *19*, 4958-4968.
4. Käfer, D.; Bashir, A.; Witte, G., Interplay of Anchoring and Ordering in Aromatic Self-Assembled Monolayers. *J. Phys. Chem. C* **2007**, *111*, 10546-10551.
5. Käfer, D.; Witte, G.; Cyganik, P.; Terfort, A.; Wöll, C., A Comprehensive Study of Self-Assembled Monolayers of Anthracenethiol on Gold: Solvent Effects, Structure, and Stability. *J. Am. Chem. Soc.* **2006**, *128*, 1723-1732.

Chapter 5

Coverage-Dependent Modification of the Surface Electronic Structure of an Organic-Semiconductor-Adsorbate Layer

The electronic structure of a hexa-*cata*-hexabenzocoronene (HBC) / Cu (111) interface is investigated by two-photon photoemission over a range of coverage from 0 to 2 ML monolayers. It is found that increasing the HBC coverage shifts the vacuum level of the Cu substrate until this shift saturates at a coverage of ~2 ML. Over this same range of coverage, the Shockley and the bare-surface Cu(111) image-potential states are shown to be quenched, while new unoccupied states appear and grow in strength with coverage. The use of momentum- and polarization-resolved photoemission spectra reveals that the new states are modified image states.

5.1 Introduction

Rational design of organic photovoltaic electronic (OPV) devices requires a detailed and complete understanding of the organic semiconductor (OS) interfaces throughout the device structure. Thus, research to understand the fundamental chemical physics of these interfaces has been extensive and summarized in several recent thorough reviews [1-4]. This prior research has shown, for example, that the electronic structure of the OS /metal interface plays an important role in electron transport across the metal-contact interface and, hence, charge collection in the photovoltaic cell. In addition, these studies have determined that the interactions between the adsorbed molecules and the metal/surface layer can cause the formation of new energy states at the interface, and a shift in interfacial electron-barrier heights (due to changes in interfacial energy levels) and transmission through the barriers (due to broadening of the electronic levels); these phenomena can lead to a reduction in charge transfer across the interface. In the present paper, we use the model system of the OS, hexa-*cata*-hexabenzocoronene (HBC), on Cu(111) to develop a fundamental atom-level understanding of the interfacial electronic structure. Our experiments use two-photon photoemission (TPPE) in conjunction with ultrahigh-vacuum (UHV) surface preparation to probe the interfacial electronic structure of a pristine HBC/Cu(111) interface. TPPE provides a versatile probe of model interfaces since it allows both the occupied and unoccupied interfacial states to be examined over a wide spectral range and with femtosecond-time resolution[4-10].

Our choice of model system is based on recent interest in and synthesis of HBC, a promising organic photovoltaic material. In particular, HBC is known to be a non-planar p-type organic semiconductor, which is photoconductive with high-efficiency of charge separation [11]. It has recently also been shown to have a high open-circuit potential when blended with C_{60}.

Specifically the value of V_{oc}, which is set by the HOMO-LUMO gap, is 1 eV [12]. In addition, this PV material has attractive material properties, which allow it to co-crystallize with C_{60} to form a ball and socket molecular pair[10]. The material is also chemically air-stable when processed in organic solution. It has also been characterized/tested via the fabrication of HBC solar photovoltaic devices, as described in Ref. 12. In particular, the OPV devices of HBC/C_{60} in a bilayer architecture have open-circuit potentials, which are close to the theoretical values, and promising overall efficiencies [12]. The devices are also chemically stable even in an air ambient and can thus be used under ambient condition without any encapsulation. HBC is a robust molecular species; thus differential scanning calorimetry experiments have shown that HBC is thermally stable up to 320˚C.

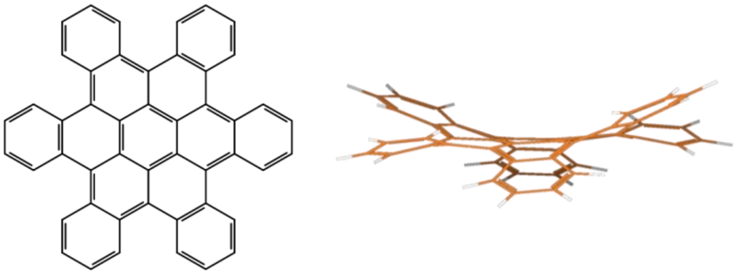

Figure 5.1 Molecular structure of hexa-*cata*-hexabenzocoronene. The molecule is ~14 Å in width and has a bending angle for the intersecting pentacene-like subunits of ~20˚.

The molecular structure of HBC is sketched in Fig. 5.1. The "contorted" structure of HBC, shown in the side view of this molecule, reported in Ref. 13, is reproduced via computations based on geometry optimization, using either force-field or *ab initio* simulation packages. The origin of distortion from planarity is the steric clash of its proximal hydrogen atoms. The molecule width is ~14 Å and its height is 3.5 Å and the bending angle of each intersecting pentacene-like subunit is ~20˚. With respect to the structure of HBC on metal surfaces, several STM studies have been reported [14, 15]. These studies show that on reactive-metal surfaces such as Ru(0001), individual HBCs are strongly bound to the metal surface and, in fact, some molecules are flattened due to partial dehydrogenation [14]. On the other hand, HBC has been shown to be mobile on Cu(111), leading to self-assembly of a honeycomb-like island structure [15]. These prior STM studies were carried out at sub-monolayer coverage only, and thus the structure in its monolayer or bilayer form is still not understood. In addition, there appear to have been no prior studies of the interfacial electronic structure of HBC.

Due to the broken translational symmetry of a surface, along with any adsorbate-induced effects, new surface electronic structure is induced in an adsorbate-covered surface, which is different from that of the bare surface. One distinctive surface feature, which appears both on a bare surface and in the presence of adsorbate layers or islands is that of a series of image potential states [4, 6, 7, 9, 16-24] These interfacial states are of particular interest because they are present on a variety of surfaces and their properties are very sensitive to the surface environment. Image-potential-state electrons are confined perpendicular to the surface but move freely along the parallel plane. Their energy can be expressed as a Rydberg progression,

$$E = E_{vac} - \frac{Ry}{16}\frac{1}{(n+a)^2} = E_{vac} - \frac{0.85\ eV}{(n+a)^2} \tag{5.1}$$

where E_{vac} is the energy of vacuum level, Ry is 13.6 eV, n is the principal quantum number, and a is a quantum defect. More details of image-potential states can be found in Refs. [4, 6, 7, 9, 16-23]. The sensitivity of these states to the conditions on a surface have made the spectroscopy of these states an important probe for examining a variety of surface-physics- and chemistry-related effects for organic/single-crystal-metal interfaces (see below), including electron solvation, work-function and surface polarization, electron quantum confinement, surface-electron dynamics [4, 7, 17, 18].

In fact, two-photon photoemission (TPPE) has been used recently to examine not only image states but, more generally, unoccupied surface states of organic semiconductor interfaces. Organic film-covered electrode surfaces may modify image potential states and often develop molecule-derived states such as HOMO/LUMO pairs and charge-transfer states. In prior TPPE studies of organic semiconductor interfaces, the effect of changing coverage on image potential states has been investigated [25-29]. For example, TPPE studies on C_{60} on Cu(111) [25] have revealed that image-derived states show a distinctly different dispersion property in the 1ML and 2ML film phases because of changes in electronic surface corrugation in the presence of adsorbed molecules. More generally, the coverage dependence of electronic structure for organic semiconductor interfaces is, thus, a useful approach to understand the fundamental electronic structure of surface states. In addition, the morphology or crystal structure of a film has been shown to depend on the coverage or density of molecules due to intermolecular and molecule-surface interactions [30-32]. Finally as suggested above, since image-potential states are located at the interface, the energy and dispersion of image states are strongly affected by the structural evolution of an organic film and thus the properties of these states such as binding energy or dispersion can be used to probe this structure.

In this paper, we employ TPPE to measure both initially occupied and unoccupied states at a HBC/Cu interface as a function of coverage. In particular, the paper describes the use of femtosecond TPPE to follow the formation of the interface electronic structure. Our femtosecond probe has a sufficiently high data rate to allow ready measurement of angle resolved photoemission, which in turn allows examination of the issues of localization [4, 7, 33, 34]. For our measurements, pristine surfaces are prepared by careful sputtering and annealing in UHV. *In situ* dosing and TPPE are used to track the change in interface electronic structure as coverage is precisely varied. This later capability also enables the nature and magnitude of the interfacial polarization or work function to be carefully investigated. And in fact, with this instrumentation, we find that the work function and electronic structure of the Cu substrate surface strongly depend on the coverage of HBC. In particular, using our coverage-dependent photoemission spectra, we have observed a disappearance and growth of unoccupied states for 0-2ML-covered HBC/Cu(111). In addition, we have further identified the nature of these newly developed unoccupied states by angle- and polarization-resolved photoemission experiments and attributed them to adsorbate-shifted image states.

5.2 Experimental Section

Our experiments used a high-purity (99.999% purity), single-crystal Cu(111) sample of 1.2-cm diameter. The sample was placed in a UHV chamber ($<2\times10^{-9}$ Torr) equipped with an ion-sputtering gun, a low energy electron diffraction (LEED) instrument, a quadrupole mass spectrometer (QMS), and a spherical-sector electron-energy analyzer. The sample was prepared by Ar^+-sputtering at 1.5 keV for 20 min. and subsequent annealing to 700°C . Each sample-preparation cycle was repeated until sharp LEED spots were observed. Note that LEED observations of the bare surface together with our occupied-state photoemission capability, which can examine the intensity and position of the Cu(111) *sp* surface state, enabled us to fully characterize the quality of our UHV prepared Cu surface. Similarly, measurement of the bare-surface work function also served as a means of cross-checking the surface quality. In addition, our chamber was equipped with a QMS to fully characterize the nature of the background gas in the chamber and hence the integrity of the vacuum system.

A custom organic evaporator was fabricated in-house and used to form the molecule/Cu interface via dosing from the evaporator crucible, which was located 10 cm from the sample surface. Calibrated exposure of the surface was carried out by heating the crucible to a predetermined temperature and rotating the crucible toward the sample. The chamber pressure was monitored by an ion gauge during sample preparation. After completing the interface preparation, the sample was rotated to face away from the sample and the crucible was then cooled. Thus all surface dosing was carried out on a clean surface in UHV and at room temperature. In some experiments, as described below, post-dosing annealing was used to insure that the surface adsorbate layer was “smoothed”. The synthesis of the HBC charge for the doser was as described in previous work [35]. After loading of HBC in our evaporator in air, it was stored in the UHV chamber. Furthermore, in order to effectively remove any low-vapor-pressure impurity, the crucible of evaporator was kept heated at 150 ˚C.

Our electronic structure and surface polarization experiments made use of angle-resolved TPPE. In order to obtain high signal-to-noise ratio while minimizing space-charge effects, our TPPE system used a tunable ultrafast optical parametric amplifier driven by regeneratively amplified Ti:Sapphire laser pulses. The output from this laser was either used as generated or converted via standard continuum generation methods into visible-wavelength output pulses; these pulses were then frequency-doubled in a nonlinear crystal, producing a train of wavelength-tunable UV, 90 fs pulses at a 250 KHz repetition rate. The photon energies used ranged from ~ 3.6 to 4.8 eV. The laser was focused on the sample, and with a fixed incidence angle of 70°, so as to obtain a typical maximum fluence of ~10 J/cm^2.

Photoemitted electrons were collected using a spherical-sector energy analyzer having a momentum resolution of $\delta k_{\|} = 0.03$ Å^{-1} and the energy resolution was set to ~60 meV. The detector was rotated about the fixed sample so as to collect data along the $\overline{\mathrm{M}}-\overline{\Gamma}-\overline{\mathrm{M}}$ direction of the Cu(111) surface Brillouin zone. Our sample was biased at −4 V to reduce the effects of stray electric fields in the vicinity of sample. The photoemission data were corrected for both the additional kinetic energy and change in the parallel momentum $k_{\|}$ of the electrons due to this accelerating voltage using the method described in a literature [36]. Note that throughout our measurements, it was important to determine if the combination of surface work function and photon energy was such that an unacceptably large number of electrons were created by one photon photoemission. Typically this was an issue if the photon energy $E_{h\nu} = h\nu > 4.6$ eV and coverage $\Theta \geq 0.3$ ML; in this case, no experiments were carried out at high coverage, since the work function was then reduced to the point that one-photon photoemission occurred.

In order to determine whether a particular spectral feature originated from an occupied or unoccupied state required a measurement of a series of TPPE data, each with different photon energy at normal emission angle and identical surface properties. A comparison of the final-state-energy peak shift with photon energy then allowed determination of the nature of state being examined. Thus for an occupied state, the peak shift is known to be twice the photon-energy difference, while for an intermediate state, the peak shift is equal to the photon-energy difference, and finally for a final state, which is above the vacuum level, there is no shift in final-state energy peak with a change in the photon energy [4, 6, 17, 20, 37]. With regard to the angle-resolved capability, the measured angle of the detector and the measured kinetic energy E_k of the photoelectron are related to the parallel momentum $k_{\|}$ of the emitted electron *via* the well-known expression

$$k_{\parallel} = \frac{\sqrt{2m_e E_k}}{\hbar}\sin\theta . \tag{5.2}$$

Finally in angle-resolved photoemission, measurement of the dispersion curve of a specific spectral region is well known to allow determination of the degree of localization of the state being probed. This approach was used extensively in interpreting our photoemission experiments.

5.3 Results

Following careful preparation, illumination of the bare Cu(111) surface with our pulsed UV laser source yielded the well-known electron distribution curves (EDC) of Cu(111). In particular, the lowest curve in Fig. 5.2 (a) shows the photoemission spectrum, using illumination with monochromatic light at 3.71 eV; this spectrum contains the Shockley surface state of Cu(111). This surface state is only seen on a pristine well-ordered surface and is thus indicative of the quality of the surface and its method of preparation. Figure 5.2 (a) also shows a series of monochromatic TPPE spectra of HBC/Cu(111) as a function of coverage, from bare Cu (0 ML) to ~2ML of HBC. In addition, the expanded spectra at different values of coverage of HBC (from 0 to 2 ML) are also shown in the figure. These expanded traces in panel (b) show the coverage values indicated in the traces in panel (a).

In order to estimate the coverage, a measurement was made of the shift in work function as the dosing time was varied. One such measurement is shown in the inset of Fig. 5.2 (a), which plots work function versus HBC-deposition time. Based on the temperature-dependence of desorption, we are able to estimate the dosing time for depositing 1ML and 2ML HBC coverage;

these times are indicted by arrows in the figure. More details of these measurements are found in our discussion below and in the *Supporting Information*.

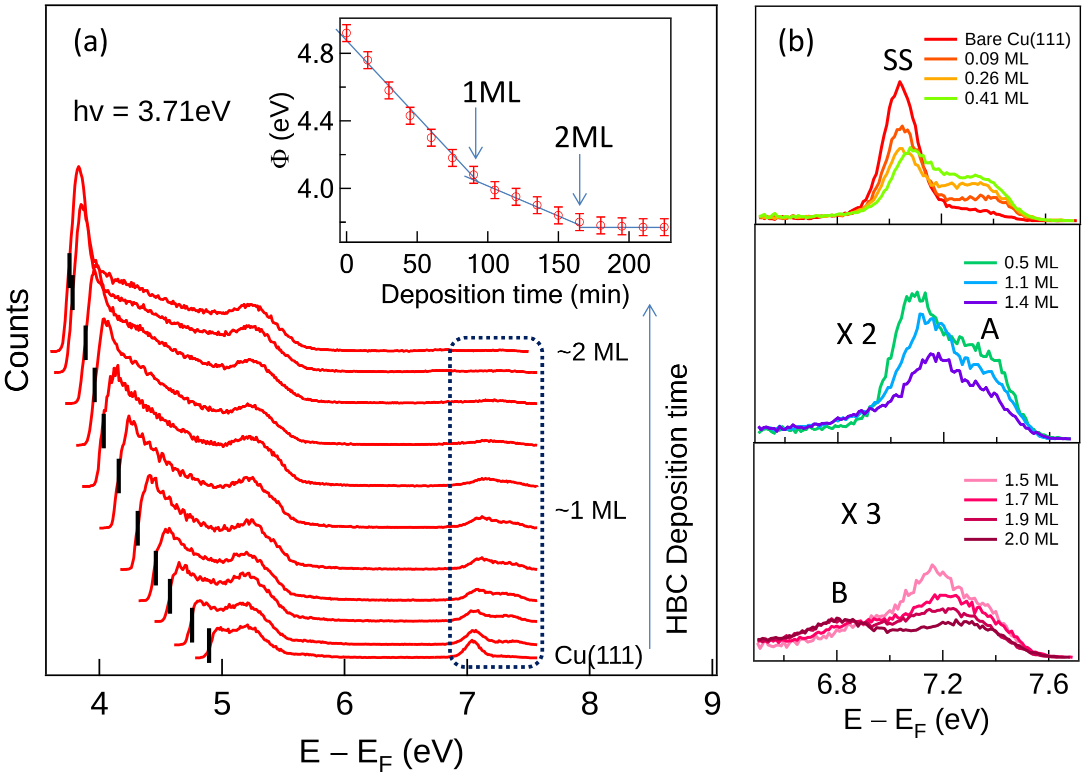

Figure 5.2 Series of monochromatic (*h* = 3.71 eV) TPPE spectra of HBC/Cu(111) vs. final-state energy (referred to the Fermi level) and as a function of coverage from bare Cu (0 ML) to ~2ML HBC. The full two-photon EDCs are shown for a set of values of HBC coverage in panel (a). The dashed box indicates the spectral region shown in panel (b). The Shockley surface state and new features (A and B) are indicated. (Inset) Surface work function plotted as a function of HBC deposition time. The dosing times for 1ML and 2ML HBC coverage are indicated by the arrows. The blue guide arrows in the inset indicate the location of a change of slope in the plot. The sharp black lines on the left side of the EDCs indicate the low-energy cutoff.

This data allows us to make several observations. First, we measure the change in the low-energy cutoff in electron kinetic energy and the vacuum level *versus* dosing time; see Fig. 5.2 (a). This plot then allows us to examine the surface polarization or work function (Φ) *versus* coverage. Note that the work function is calculated using the relation $\Phi = 2h\nu-(E_F-E_{LC})$, where E_F and E_{LC} are the Fermi edge and the low-energy cutoff in the TPPE spectra, respectively. Such a plot of work function *versus* coverage is given in the inset of Fig. 2. The data in this plot show that the work function decreases monotonically with an increase in coverage and thus does not exhibit the more complex change in polarization seen in other systems, including those with a permanent dipole [32, 38]. However, a slight change in slope with coverage is seen at two specific values of coverage. Specifically, these changes in slope are seen for dosing times of ~90 min and ~180 min. Each of these regions of the plot corresponds to the formation of a specific coverage in terms of layers: thus the initial slope corresponds to forming a monolayer ($\Delta\Phi = -0.8$ eV), while the second corresponds to a bilayer ($\Delta\Phi = -1.1$ eV), respectively. However, after the bilayer is completed, no measureable further change in the slope of work function *versus* coverage is seen. A similar behavior for work function *versus* coverage has been found in other organic semiconductors on metal surfaces [28, 29].

In addition, dosing-dependent changes are also apparent in the intensity of the Shockley surface state. In particular, the intensity of photoemission signal from this state, SS, decreases and the peak energy of its signal upshifts as the coverage increases. A more detailed plot is obtained by expanding the EDCs in the region of 7 - 7.5 eV kinetic energy. This expanded data, plotted in Fig. 5.2 (b), shows that the Shockley-surface-state shift is 0.09 eV at 1ML and then, with additional coverage, continues to shift toward higher energy but also undergoes a sharp decrease in intensity. This sharp decrease in the surface state signal with coverage is known to occur due to site filling when organics or other adsorbates are deposited on an otherwise clean Cu surface [25, 29]. Finally as the coverage increases, it is also found that two molecular-induced states (A and B) appear and grow in intensity. Note also than in the case of the A state, the intensity of the peak then decreases as the coverage increases *above* 1ML. In the case of the B state, the feature grows dramatically as the coverage exceeds 1ML and then peaks and declines as the average coverage exceeds 2ML.

The broad feature (State A), which appeared at low coverage, was also examined using angle-resolved monochromatic TPPE. An example of one such set of results, for the specific case of a surface of 0.5 ML HBC/Cu(111), is plotted in Fig. 5.3. These measured angular-dependent photoemission spectra show the dispersive surface state, as well as a new feature A. The absolute energy of the surface state is −350 meV from E_F; this value is shifted by ~ 0.05 eV from its peak energy on a clean surface. Thus the surface and the A states are separated by only ~180 meV, making it difficult to extract precise information on their energy separation, given our instrumental resolution of 60 meV. Since the surface-state is seen with high S/N, its effective mass, i.e., $m^* = \hbar^2 (d^2E/d^2k)^{-1}$, can be readily extracted. Based on a parabolic curve fitting, the effective mass of the Shockley state is $m_{ss}^* \sim 0.4\, m_e$. On the other hand, the dispersion of the A state is not easily obtained in the plot in Fig. 5.3 (a) since the weak A state merges with and is thus not resolvable from the surface state, except at higher values of $k_{||}$. Other dispersion data for state A are presented below.

In order to further characterize the A state, the polarization dependence of A was investigated; one set of results are shown in Fig. 5.3 (b). This measurement showed that the intensity of the A state when pumping with *p*-polarized light was > 100× times that when pumping with *s*-polarized light; see the caption for Fig. 5.3 (b). This strong polarization dependence is similar to that typically observed for image or surface states. Since the unoccupied orbitals of HBC, which are located below vacuum level, are π*- type and can be excited by *s*-polarized light; our results indicate that state A is not a HBC molecular state.

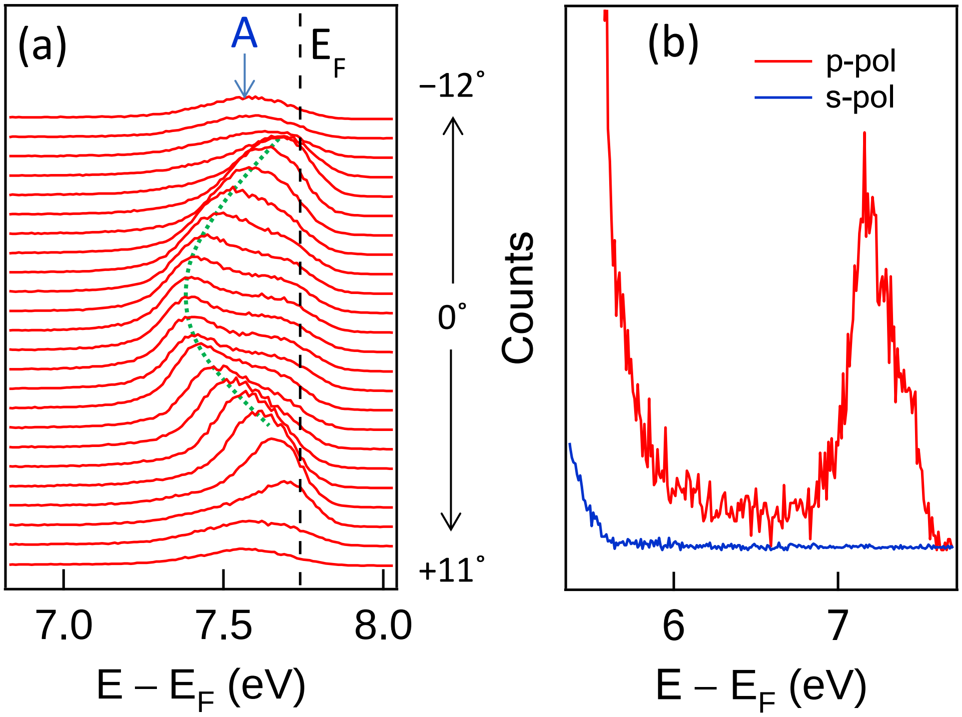

Figure 5.3 (a) TPPE spectra of a surface of 0.5 ML HBC/Cu(111) and $E_{h\nu} = 3.87$ eV The green line indicates the Shockley surface state (SS); the blue arrow indicates state A. (b) The polarization dependence, i.e., *s* and *p*, of the TPPE spectra of 0.8 ML HBC/Cu(111) with $E_{h\nu} = 3.73$ eV; note that any signal from the *s*-polarization is below the S/N ratio of our detection system.

In an effort to acquire higher S/N for higher-resolution spectra, we performed bichromatic studies of surface photoemission at low coverage, i.e., $\Theta \leq 0.3$ ML HBC on Cu, as shown in Fig. 5.4. Because of the lower energy of the second photon in this process, the photoemission process from the excited state has a higher cross section and, in addition, there are typically less secondary electrons created in the bichromatic process. These factors allow us to obtain higher S/N, thus enabling acquisition of the coverage-dependent scan shown in Fig. 5.4. These data show clearly an evolution of the electronic structure with coverage. Consider first, for example, the spectral feature A; when coverage increases to 0.1 ML, this feature rises above the signal-to-noise ratio and then grows with increasing coverage. In fact, a plot of the intensity of this feature normalized to that of the image state (IS) (see discussion in the following paragraph) *versus* coverage, shows clearly that the spectral intensity of this peak *versus* coverage is anticorrelated to that of the image-state intensity. Note that the $n = 1$ image state (IS) is found in the bichromatic TPPE spectra, while this state is not observed in other monochromatic spectra in Figs. 5.2 and 5.3. The reason that this state is observed in bichromatic TPPE is because the energy of the pump photon in bichromatic TPPE $E_{h\nu,\,pump} = 4.72$ eV (with $E_{h\nu,\,probe} = 1.55$ eV) is high enough to access the image state in the first step of the two-photon photoemission scheme, whereas in the monochromatic pumping scheme used here the pump photon energy is $E_{h} < 4$ eV and is energetically unable to access the image-state.

Second, the coverage-dependent measurements also show that the energy of the A state, as measured by its peak location, is independent of the sample work function even for a work-function change (decrease) of ~ 0.3 eV. This absence of a shift with work function change is also seen, for example, in the case of the bare-surface Cu(111) image state, which is denoted by the label IS. In this connection, extensive prior measurements of image states on metal crystals have shown that such states, which are intermediate states for TPPE, are ”pinned” to the Cu(111) *local* vacuum level. The present results suggest that the A state is an unoccupied state located at ~3.7

eV above the Fermi level (or 1.15 eV below vacuum level at 0.3 ML); thus for our excitation scheme, it is an intermediate state. In order to confirm that this state was an intermediate state, experiments were carried out to measure the photon-energy dependence of monochromatic TPPE at large detection angles or $k_{||} > 0.20\text{Å}^{-1}$. These experiments (not shown in the figures) showed that the peak of the A state shifted linearly with photon energy, thus positively identifying it as an intermediate state.

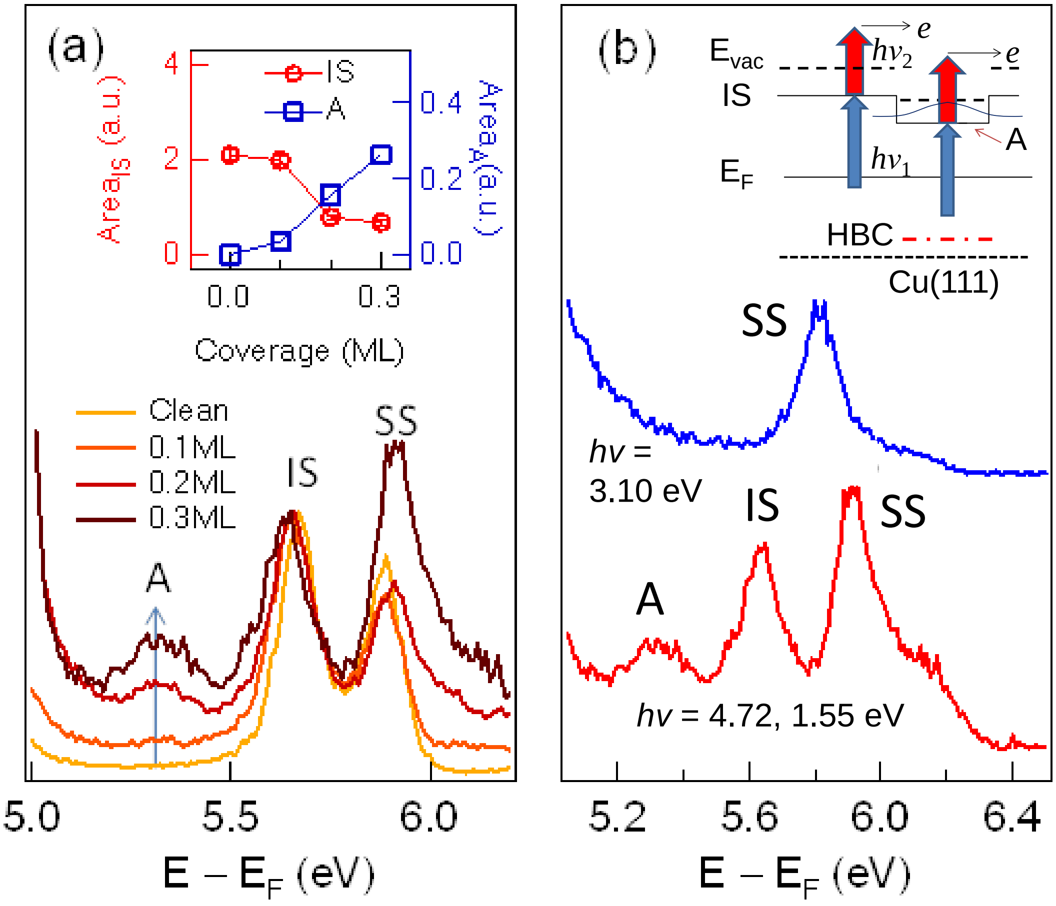

Figure 5.4 (a) Bichromatic TPPE spectra of 0.0 (bare Cu), 0.1, 0.2, and 0.3 ML HBC/Cu(111) with $E_{h\nu,\, pump}$ = 4.72 eV and $E_{h\nu,\, probe}$ = 1.55 eV. The arrow indicates a new state “A”, which grows in intensity with coverage. IS and SS are the image state (n =1) and Shockley surface state, respectively. The data is normalized with respect to the intensity of IS. (Inset) Area of IS (red) and A (blue) as a function of coverage. (b) Monochromatic ($E_{h\nu}$ = 3.10 eV) and bichromatic TPPE spectra of 0.3ML HBC/Cu(111). Intermediate states such as A and IS appear in the bichromatic spectrum only, as is discussed in the text. (Inset) Schematic position-dependent energy diagram of an HBC island on Cu(111). .

In order to examine the extent, to which the states were localized, as well as to assist in their identification, bichromatic *angle-resolved* TPPE measurements were made in the vicinity of peak A using $E_{h\nu,\,pump}$ = 4.68 eV and $E_{h\nu,\,probe}$ = 1.55 eV; this set of data is shown in Fig. 5.5(a). It is clear that state A exhibits dispersion. Using this data in this figure and Eq. 2, the dispersion curves of the state A are plotted for electron kinetic energy *vs.* parallel momentum as is shown in Fig. 5.5(c). Our data show that the effective mass of state A (m_A*) is 1.1 ± 0.1m_e. In addition, the image state, IS, appears possibly less dispersive, i.e., m^* = 1.5 ± 0.5m_e, than for typical image states, m^* = 1.0 m_e, on clean surfaces. In addition, the data also show that there is no change in the Shockley surface-state dispersion with low HBC coverage. Finally, note that the linearly dispersive bulk copper *sp* state is apparent as a weak spectral feature adjacent to the image state at high $k_{||}$, in accord with earlier measurements [39].

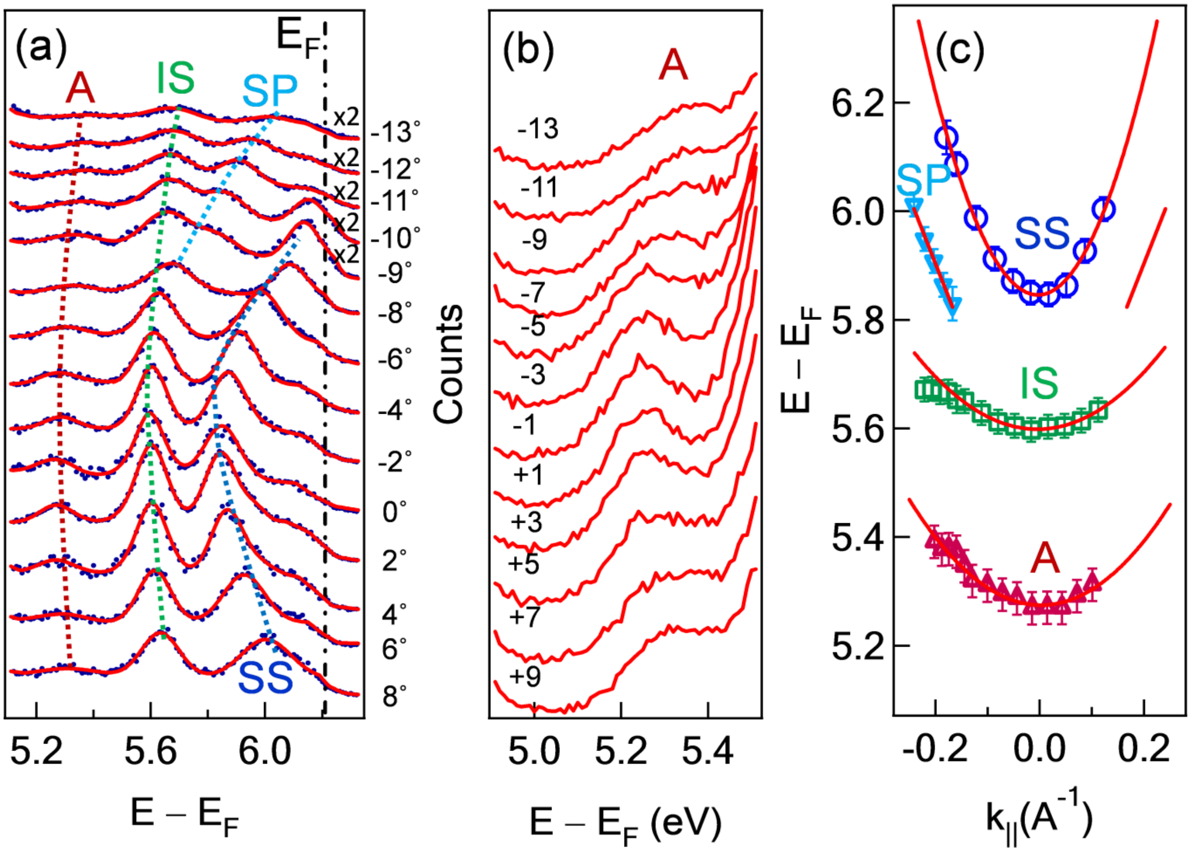

Figure 5.5 (a) Angle-resolved TPPE spectra of 0.3ML HBC on Cu(111) in the vicinity of peak A with $E_{h\nu,\,pump}$ = 4.68 eV and $E_{h\nu,\,probe}$ = 1.55 eV. (A: a new state, IS: image state (n = 1), SS: Shockley surface state, SP: bulk Cu intermediate state [39]). (b) Data taken in a selected energy range with $E_{h\nu,\,pump}$ = 4.62 eV and $E_{h\nu,\,probe}$ = 1.55 eV to improve the signal-to-noise ratio. (c) The dispersion curves of the state A, image state, and surface state derived from (a).

After increasing the HBC coverage to higher values (1-2 ML), it was found that an additional spectral feature, state 'B', was present at 6.1-eV final-state energy above the Fermi level, i.e., $E{-}E_F$, as shown in Fig. 5.6(a). In addition, coverage-dependent measurements show that this state grows with increasing coverage; this behavior is in contrast to the intensities of the surface state and state A, which decrease with coverage over this same range of coverage, i.e., 1 - 2 ML. A measurement of the peak shift *vs.* photon energy, as shown in Fig. 5.6(b), also indicates that state B is an intermediate state. In particular at 2 ML HBC coverage, the peak is located at 0.8 eV below the vacuum level (that is its binding energy is 0.8 eV), under conditions, for which the surface-averaged work function is ~3.8 eV, i.e., that for a 2ML film.

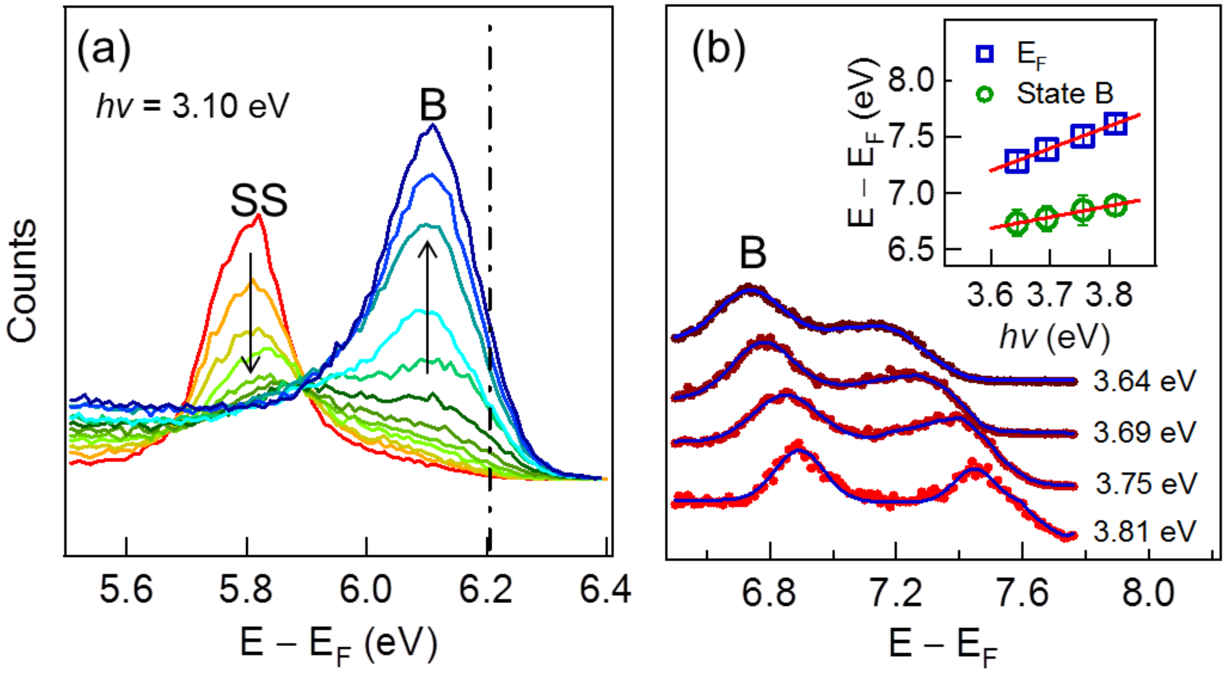

Figure 5.6 (a) A series of TPPE spectra of HBC/Cu(111) as a function of HBC-coverage in the region of the electron kinetic energy near state B at $E_{h\nu}$ = 3.10 eV. Black arrows indicate the intensity decrease of the SS, while at the same time the intensity of B is increasing from Θ = 0 to 2 ML; the coverage increases by approximately 0.16 ML for each curve in going from the lower to the upper curve of state B. (b) TPPE spectra of 2ML HBC /Cu(111) with different photon energies ($E_{h\nu}$= 3.64 - 3.81 eV). The amount of peak shift is, to within error, $\Delta E_{h\nu}$, as shown in the inset.

The nature of state B can be further clarified by examining its dispersive character; see the data in Fig. 5.7(a) and 5.7(b). The figures show that this state is strongly dispersive and its effective mass is $m^* = 0.96 \pm 0.08\ m_e$, which is close to the free-electron mass measured for image states. The measured polarization dependence of this state (not shown here) showed that it had σ symmetry, as is also seen in our surface and image states. Based on our observations, we conclude that state B is the modified image state ($n = 1$) characteristic of 2ML HBC/Cu(111). Note incidentally that in our measurements, the presence of other higher-lying image states, for example the $n = 2$ state, could not be detected due to their low intensity and presence of other nearby states. Also as seen in Fig. 5.6, there appears to be an additional state at ~ 0.6 eV above the B state; however, this state is distorted by its proximity to the Fermi edge and was not examined further. Figure 5.6(a) also shows that the energy of state B is independent of coverage over the range from 0 to 2ML. One possibility for this lack of coverage dependence is that the state is pinned to local vacuum level, as is the case for image states. This behavior would be consistent with a surface with a growth mode that is island-type and where the image state is on an island.

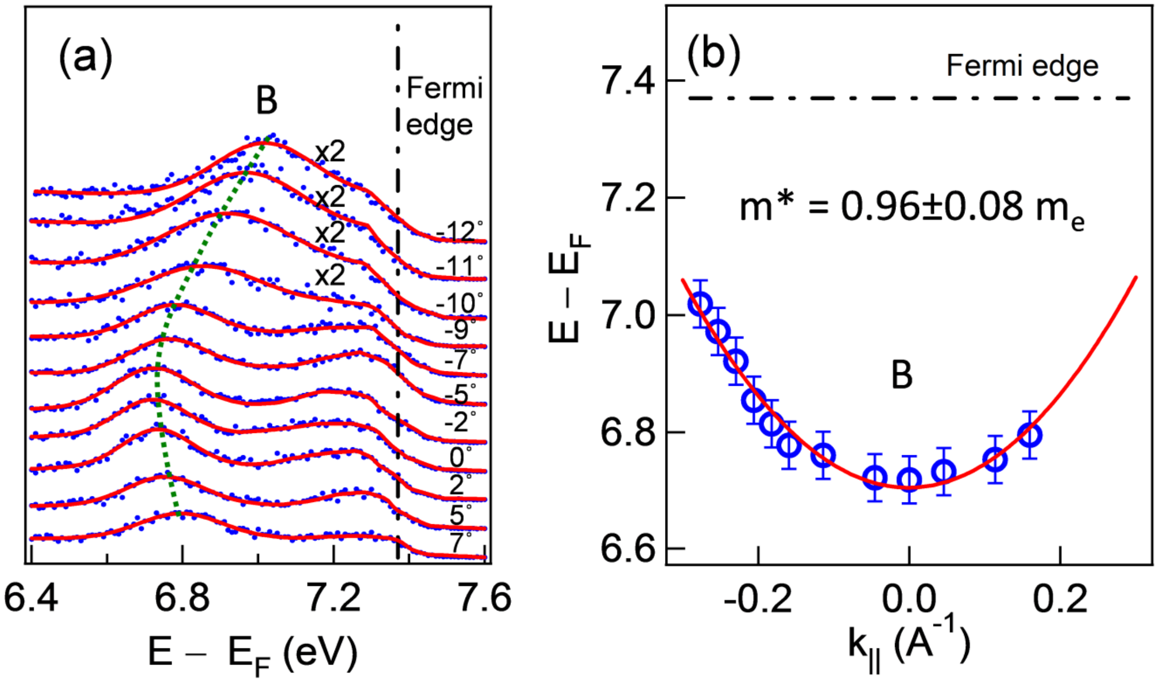

Figure 5.7 (a) Angle-resolved TPPE spectra for peak B, with $E_{h\nu}$ = 3.68 eV and Θ = 2ML HBC coverage, at different emission angles (b) The measured dispersion curves of peak B, which yields an effective mass m^*= 0.96±0.08 m_e. The error bar is set by the uncertainty of fitting and photon energy.

5.4 Discussion

5.4.1 *Work Function of HBC/Cu(111) and Its Coverage Dependence*

The work function of a surface is a measure of the surface potential barrier plus the chemical potential of substrate materials[3]. The presence of adsorbates can modify this surface potential and result in major modification of the interfacial dipole. As discussed in several recent reviews, experimental investigations in the last two decades have shown that there are several possible mechanisms for alteration of the polarization at a molecule/metal interface by adsorbates, including “push-back” of the “spilled out” electron distribution, charge transfer, induced states, formation of chemical bonds, and adsorbate permanent molecular dipoles[40]. However, in our case, HBC does not possess a permanent dipole and thus this channel for work function change is not applicable. In addition, HBC is known to be mobile on Cu(111)[15] and to have a relatively low desorption temperature; both observations indicate that interfacial chemical reactions do not occur and thus this chemical source of work function change is also not present in our case.

Finally, push-back (or the cushion or pillow effect[41]) is known to be a major mechanism for the reduction of the adsorbate/interfacial work function. It is clearly delineated in the case of physisorbed species on a metal surface. In fact, work function changes due to push back can dominate changes due to other mechanisms for the adsorbate/metal system. For example, Terentjevs, *et al.* showed that vanadyl naphthalocyanine (VONC) shifts the work function of Au (111) by 0.7 eV through push-back and this shift actually reduces the molecular-dipolar contribution to the work function[42]. On the other hand for an HOPG substrate with this same molecular adsorbate, push back is known to be small or nonexistent and, in that case, the interfacial dipole is determined by the molecular adsorbate dipole[26]. Another, perhaps more specifically relevant, example of push-back is for corannulene ($C_{20}H_{10}$) on Cu(111)[43]. This bowl-shape-aromatic hydrocarbon reduces the work function of Cu (111) by −1.3 to −1.5 eV via the push-back mechanism alone. Thus it is reasonable that the same phenomena should be present for the HBC/Cu(111) system, in which HBC also has a partial bowl-like configuration**,** and would also then be expected to reduce the work function by approximately the same magnitude; our measurements show in fact a 0.8-1.1 eV work function reduction (see inset of Fig. 5.2(a)).

In addition, it is also known from prior studies of large organics such as perylene-3,4,9,10-tetracarboxyilic dianhydride (PTCDA) and copper phthalocyanine (CuPc), that the Induced Density of Interface States (IDIS) mechanism may contribute significantly to the work function shift of an adsorbate surface[44, 45]. For example, 60% of the work function shift for PTCDA/Au ($\Delta\Phi_{total} \sim 0.25$ eV) and 80% for CuPc/Au ($\Delta\Phi_{total} \sim 1.2$ eV) were attributed to charge transfer [45]. In this mechanism, which has been studied extensively by the Kahn Group, if the chemical interaction of an organic semiconductor with a metal substrate significantly broadens the molecular levels, the density of states (DOS) in the band gap of the molecule may then significantly increase[2, 44, 46]. This induced DOS then "fills up" the gap region to the charge neutrality level (CNL), which typically occurs in the energy range between midgap and the LUMO level for many organic semiconductors. The offset between the CNL and the Fermi level can then act as a driving force for partial charge transfer through the interface. For our HBC/Cu(111) system, the lack of clear molecular states in our photoemission spectra suggests that significant broadening of molecular states is occurring. Based on the typical CNL position of organic semiconductors and the electronic structure of HBC crystals (ionization energy ~5.5 eV and band gap ~3.1 eV)[12], the CNL position of HBC can be roughly estimated to be between the midgap (−4 eV) and the LUMO (−2.4 eV) of HBC with regard to the vacuum level. In this case, electron transfer from HBC to Cu can occur and thus contribute to surface polarization. Since both push-back and charge transfer polarize the interface in the same direction, both effects may well be important for our experimental data. In order to quantify the degree of charge transfer, the induced DOS of HBC need to be obtained by other methods, including DFT calculations.

Although Fig. 5.2 shows that the average surface work function decreases monotonically with increasing coverage, Θ, there is a significant difference between the slope of this decrease for $\Theta < 1$ML in comparison to that for $\Theta > 1$ML, i.e., the work function change is 0.8 ± 0.1 eV from 0 ML to 1 ML and 0.3 ± 0.1 eV from 1 ML to 2 ML. This same change, i.e., a decrease, in the slope in Φ *vs.* coverage has been also observed for other aromatic molecules on metal substrates[28, 29]. Consider first the decrease when $\Theta < 1$ML. This gradual change is due to the fact that as the concentration of adsorbates rises, the total effect of push-back/charge transfer (see above) across the surface of the metal also increases and the work function then decreases. Second, the change in slope in going to $\Theta > 1$ML can be attributed to screening by the completed first layer. In summary, the polarization changes seen in our measurements are in accord in magnitude and layer dependence with changes seen in other organic/metal systems[6, 28, 29, 37] and are consistent with the mechanisms discussed here.

5.4.2 Bare Metal Image State (IS, n=1) at Sub-Monolayer HBC Coverage

As reviewed above, image states are two-dimensional states confined by Bragg scattering from the substrate surface lattice and by the image-potential Coulombic attraction on the vacuum side of the electron motion. Depending on their principal quantum number *n*, these states have their greatest probability density from a few to few tens of Å's above a metal or dielectric surface. Their spatial distribution and physical origin allow image states to be used as a surface probe. In fact, changes in surface structure or the presence of dielectric overlayers can be detected by changes in the binding energy or dispersion of image electrons[19, 47, 48].

From our results, we can conclude that our state IS, as indicated in Figs. 5.4 and 5.5, is the *n*=1 "bare-surface" image state on the copper-exposed areas of a sub-monolayer HBC-covered copper surface. This identification is apparent because, first, there is only a small (~20 meV) difference shift in binding energy of the image state from that on clean Cu(111). Second the intensity of the IS was found to decrease with an increase in the HBC coverage. Image states are known to have their energies pinned to the local vacuum level of copper surface; thus the absence of any significant binding energy shift in the IS state energy level as the HBC coverage increases is entirely consistent with such "pinning". This behavior has been observed for other molecular-adsorbate-covered metal surfaces when the adsorbates exhibit island growth[6, 28, 29, 49].

Our measurements also show that the IS dispersive properties are slightly if, at all, affected by the presence of HBC. In particular, our angle-resolved TPPE measurements for 0.3 ML HBC/ Cu(111) show that the effective mass of the IS is, within experimental error, the same as that of clean copper, i.e. its effective mass is the expected value of $m^* = 1.0\ m_e$. Our dispersion measurements showed that no significant change in the effective mass of the IS state as coverage increased from 0 to 0.3 ML. While bare surface dispersion is seen for some cases of organics on single-crystal metals, in other cases bandfolding has been measured and attributed to periodic potential variation from adsorbed molecules on the surface (see the next section for a more extensive discussion).

5.4.3 Origin of State A

As discussed below, both our monochromatic and bichromatic TPPE measurements reveal that the HBC-covered-copper surface state A is 3.7 eV above the Fermi level at the typical coverage of 0.3 ML used in many of the experiments for the present paper. Our polarization-dependent studies suggest that this state does not originate from π-conjugated molecular orbitals. Since the spectral peak intensity of the bare-Cu(111) image state is anticorrelated with the intensity of state A at submonolayer coverage, it is reasonable to consider whether state A is also derived from the $n = 1$ image state; that is, whether the addition of adsorbates gives rise to this state by simply shifting the energy and dispersion of the bare Cu(111) image state. Recent experiments by others using a variety of organic adsorbates have shown clearly that image states can form on surfaces fully covered, i.e., 1-3 ML, with alkanes, aromatics, or even C_{60}-type adsorbates[4, 5, 7]. In these cases, the image-state binding energies were found to be modified by the presence of molecular overlayers as a results of several phenomena including dielectric screening or the formation of a vertical "quantum well"[4, 6, 7, 27].

Consider first the shift of the work function. The inset in Fig. 5.2(a) shows that the work function of Cu(111) is shifted down from 4.9 eV to ~4.1 eV when it is covered with a full monolayer of HBC. Now consider state A for a surface covered with Θ <1 ML of HBC, that is, a condition, for which the surface is covered only with monolayer-thick islands. During photoemission any electrons emitting from these islands experience a local work function, Φ_L[6], a phenomena originally discussed in terms of metal hetero-islands on flat surfaces. A schematic showing the energetics in such a local work function are shown in Fig. 5.4(b) inset. As is shown in Ref. 6, this local work function is very close to the measured work function, $\Phi(\Theta = 1)$ for 1ML fully covered adsorbate surface, i.e., for our experiment, a 1-ML HBC-covered surface. An important aspect of the existence of the local work function is that it leads to a laterally defined potential-well barrier on the boundaries of the islands, which has the approximate magnitude of the local work function of Cu(111) minus that of the 1-ML-covered HBC surface, which is ~ 0.8 eV. This lateral barrier can then confine the image electron on the lower-work-function surface if they are trapped prior to their recapture by the metal surface.

If this value of Φ_L and the measured energy of state A is used, the measured binding energy, as referred to the local vacuum level, would be ~0.4 $\pm$ 0.2 eV, where the estimated error bars are obtained by consideration of the uncertainties both in energy and coverage. Note this value seems somewhat smaller than that expected from a value of the adsorbate-induced downward shifted n=1 image state within the projected band gap in Cu(111) based on the phase-analysis consideration of Refs. 47 or 50. And in fact, the binding energies of the n = 1 image state of other adsorbed-molecule-covered Cu surfaces have varied widely from 0.4 eV to 1.1 eV[19, 50]. Finally note that our coverage is generally much smaller than that used in applying the dielectric continuum model to calculating binding energies of image states at dielectric/metal interfaces[18, 33, 48, 50]. In addition, while the DCM model has been used successfully for noble gases and alkane molecules, its applicability for organic semiconductors may be more limited because the DCM model does not include either the electronic or atomic structure of the adsorbates.

Consider next the degree of localization of the image state on the Cu surface. As indicated in Fig. 5.5, our dispersion data suggest that the adsorbate-modified image states has dispersion characteristics, which are similar to that of an $n = 1$ image state on a clean Cu surface. In this connection, many prior studies have found that image states of organic semiconductors/metal systems are normally dispersive, as in the present case[5, 27, 29, 51]. However, in other cases, organic semiconductor layers, including presumably islands, cause the formation of localized image states due to either to polaron formation[7], or to structural or electrical corrugation[25], or to hybridization with molecular states[26]. In other cases periodic potentials within the molecular islands are known to lead to backfolding. In our case, prior STM observations[15] have shown that HBC exhibits island-type growth of HBC, even at low coverage (0.3 ML). Our free-electron-like dispersive data shows that these localization and backfolding mechanisms do not appear to play an important role for the modified image state on the HBC islands. Note that the apparent lateral variation in potential on a sub-monolayer HBC-covered surface, seen in the low-temperature STM study[15], seems at odds with our observations. Thus, a more systematic study [30] as to how this periodic potential effects localization of electrons is required.

To summarize this subsection, based on our observations discussed above, the A state is due to local modification of the work function by adsorption of the image electron on monolayer-thick islands of HBC. Short wavelength periodic lateral confinement of the electron by the molecule does not appear to be present in this case of state A.

5.4.4 Origin of State B

Our measurements of dispersion, binding energies, polarization- and their coverage-dependence suggest that state B also arises from image electrons trapped on islands, i.e., for this surface, image electrons affixed to the 2ML HBC regions on an otherwise 1ML- covered surface of Cu(111). Our TPPE measurements reveal that the HBC-covered-copper surface state B is 3.8 eV above the Fermi level. As shown in Fig. 5.6(a), state B is observed only when additional HBC absorbs on a 1ML-covered surface. Specifically, the B-state peak appears at ~1 ML, and then grows in intensity until the coverage increases to 2 ML. The binding energy is independent of changes in the average work function of the surface, say between 1 and 2 ML. If we compare the binding energy of state A for a 1 ML surface with B on a 2ML surface, the two states differ by 0.40 ± 0.2 eV. This difference is consistent with the known fact that image-state binding energies are modified by the number of adsorbed layers on metal surfaces, which support the image electron [4, 7].

The above coverage behavior is due to the fact that the energetic position of state B is coupled to any *local* work function change for HBC-covered Cu(111); although it is independent of the average work function as mentioned in the previous section. Image states are pinned to the local vacuum level so that a shift of the vacuum level, with regard to a fixed spectrometer surface, is directly proportional to the shift in the local work function [6, 17, 28, 29]. Such a shift would occur if 2ML regions were present on the full 1-ML-covered metal substrate. As described in the previous section, the local work function of the adsorbate island can be closely approximated by the value of the work function for a large-area surface with the same coverage on the island. In the case of state B, the local work function in this approximation would thus be equivalent to that measured for a full 2ML film of HBC on Cu (111). The measured local work function for 2ML

HBC/Cu(111), 3.8 eV, is considerably lower than 4.9 eV of bare Cu(111) [see Fig. 5.2(a) inset]. Furthermore, the fact that the photoelectron spectra of B remain constant as the coverage is varied between 1 and 2 ML [Fig. 5.6(a)] argues that the film structure does not depend on surface coverage. In order to quantify the effect of work function on state B, we can compare the binding energy of state B with that of the well-defined $n = 1$ image state of bare Cu(111). Using the Fermi level as the energy reference, we find that the energetic difference between the image state ($n = 1$) on bare Cu(111) and state B is 1.05 eV, which is, within experimental error, equal to the difference in work function of the two surfaces of 1.10 eV.

The shift in binding energies of the state B image state is consistent with other prior observations of image states modified by the presence of molecular layers on a metal substrate. Based on the local work function, 3.8 eV, the binding energy of state B is 0.80 ± 0.2 eV; note that the uncertainty in the local work function assumption is significant for the 2ML case as the position of the 2ML break is not clearly defined by the reduced slope of the work function/exposure curve in the inset in Fig 5.2. While this value is larger than that for the A state, it is within the combined error of the binding energies of the two states. In addition, this value is, as mentioned above, clearly comparable to that on other organic/metal interfaces.

5.5 Conclusion

The surface states of a metal surface, say an electrical contact, are sensitive probes of the adsorption and modification of its surface structure and its electronic properties by an adsorbed organic layer. In our experiment, a promising organic semiconductor for photovoltaic applications, HBC, was deposited on a Cu(111) substrate using a precisely controlled gas-phase doser. The electronic structure of the newly formed interface was then monitored by angle- and polarization-resolved TPPE. While the work function of the HBC/Cu system monotonically decreases with an increase in coverage of up to 2ML, the image potential state evolves in a more complex manner. As coverage increases for $\Theta = 0 - 1$ML, the $n = 1$ state of the bare Cu surface is converted to state A, which has the σ symmetry of a typical image state. At the same time, the Cu *sp* surface state is quenched with coverage. For $\Theta = 1 - 2$ ML, an additional state, B, begins to grow and becomes the most predominant feature among the unoccupied surface states. As for the case of state A, state B is dispersive, with a binding energy comparable to the n=1 image state of Cu. The energetic position of both of these intermediate states is indicative of the image electrons being trapped by the local work function discontinuity at the HBC island edge in each of the coverage regimes. The value of the local work function for each state is compatible with prior observations of work functions of organic species on Cu(111).

References

1. Braun, S.; Salaneck, W. R.; Fahlman, M., Energy-Level Alignment at Organic/Metal and Organic/Organic Interfaces. *Adv. Mater.* **2009,** *21* (14-15), 1450-1472.
2. Hwang, J.; Wan, A.; Kahn, A., Energetics of metal–organic interfaces: New experiments and assessment of the field. *Materials Science and Engineering: R: Reports* **2009,** *64* (1–2), 1-31.
3. Koch, N., Organic Electronic Devices and Their Functional Interfaces. *ChemPhysChem* **2007,** *8* (10), 1438-1455.
4. Zhu, X. Y., Electronic structure and electron dynamics at molecule–metal interfaces: implications for molecule-based electronics. *Surf. Sci. Rep.* **2004,** *56* (1–2), 1-83.
5. Armbrust, N.; Güdde, J.; Jakob, P.; Höfer, U., Time-resolved two-photon photoemission of unoccupied electronic states of periodically rippled graphene on Ru (0001). *Phys. Rev. Lett.* **2012,** *108* (5), 056801.
6. Fauster, T.; Steinmann, W., Two-photon photoemission spectroscopy of image states. *Electromagnetic Waves: Recent Developments in Research* **1995,** *2*, 347-411.

7. Szymanski, P.; Garrett-Roe, S.; Harris, C. B., Time-and angle-resolved two-photon photoemission studies of electron localization and solvation at interfaces. *Prog. Surf. Sci.* **2005,** *78* (1), 1-39.

8. Stahler, J.; Bovensiepen, U.; Meyer, M.; Wolf, M., A surface science approach to ultrafast electron transfer and solvation dynamics at interfaces. *Chem. Soc. Rev.* **2008,** *37* (10), 2180-2190.

9. Martin, W., Time-resolved two-photon photoemission from metal surfaces. *J. Phys.: Condens. Matter* **2002,** *14* (43), R1099.

10. Petek, H.; Ogawa, S., Femtosecond time-resolved two-photon photoemission studies of electron dynamics in metals. *Prog. Surf. Sci.* **1997,** *56* (4), 239-310.

11. Cohen, Y. S.; Xiao, S.; Steigerwald, M. L.; Nuckolls, C.; Kagan, C. R., Enforced One-Dimensional Photoconductivity in Core-Cladding Hexabenzocoronenes. *Nano Lett.* **2006,** *6* (12), 2838-2841.

12. Tremblay, N. J.; Gorodetsky, A. A.; Cox, M. P.; Schiros, T.; Kim, B.; Steiner, R.; Bullard, Z.; Sattler, A.; So, W.-Y.; Itoh, Y.; Toney, M. F.; Ogasawara, H.; Ramirez, A. P.; Kymissis, I.; Steigerwald, M. L.; Nuckolls, C., Photovoltaic Universal Joints: Ball-and-Socket Interfaces in Molecular Photovoltaic Cells. *ChemPhysChem* **2010,** *11* (4), 799-803.

13. Xiao, S.; Myers, M.; Miao, Q.; Sanaur, S.; Pang, K.; Steigerwald, M. L.; Nuckolls, C., Molecular Wires from Contorted Aromatic Compounds. *Angew. Chem.* **2005,** *117* (45), 7556-7560.

14. Rim, K. T.; Siaj, M.; Xiao, S.; Myers, M.; Carpentier, V. D.; Liu, L.; Su, C.; Steigerwald, M. L.; Hybertsen, M. S.; McBreen, P. H.; Flynn, G. W.; Nuckolls, C., Forming Aromatic Hemispheres on Transition-Metal Surfaces. *Angew. Chem. Int. Ed.* **2007,** *46* (41), 7891-7895.

15. Treier, M.; Ruffieux, P.; Groning, P.; Xiao, S.; Nuckolls, C.; Fasel, R., An aromatic coupling motif for two-dimensional supramolecular architectures. *Chem. Commun.* **2008,** *0* (38), 4555-4557.

16. Echenique, P. M.; Pendry, J. B., The existence and detection of Rydberg states at surfaces. *J. Phys. C: Solid State* **1978,** *11* (10), 2065.

17. Osgood Jr, R. M.; Wang, X., Image states on single-crystal metal surface. In *Solid State Phys.*, Henry, E.; Frans, S., Eds. Academic Press: 1997; Vol. Volume 51, pp 1-80.

18. Güdde, J.; Berthold, W.; Höfer, U., Dynamics of Electronic Transfer Processes at Metal/Insulator Interfaces. *Chem. Rev.* **2006,** *106* (10), 4261-4280.

19. Hotzel, A.; Moos, G.; Ishioka, K.; Wolf, M.; Ertl, G., Femtosecond electron dynamics at adsorbate–metal interfaces and the dielectric continuum model. *Appl. Phys. B* **1999,** *68* (3), 615-622.

20. Steinmann, W., Spectroscopy of image-potential states by two-photon photoemission. *Appl. Phys. A* **1989,** *49* (4), 365-377.

21. Smith, N. V., Phase analysis of image states and surface states associated with nearly-free-electron band gaps. *Phys. Rev. B* **1985,** *32* (6), 3549.

22. Echenique, P. M.; Berndt, R.; Chulkov, E. V.; Fauster, T.; Goldmann, A.; Höfer, U., Decay of electronic excitations at metal surfaces. *Surf. Sci. Rep.* **2004,** *52* (7–8), 219-317.

23. Harris, C. B.; Ge, N.-H.; Lingle Jr, R.; McNeill, J.; Wong, C., Femtosecond dynamics of electrons on surfaces and at interfaces. *Annu. Rev. Phys. Chem.* **1997,** *48* (1), 711-744.

24. Fauster, T.; Weinelt, M.; Höfer, U., Quasi-elastic scattering of electrons in image-potential states. *Prog. Surf. Sci.* **2007,** *82* (4–6), 224-243.

25. Dutton, G.; Pu, J.; Truhlar, D. G.; Zhu, X. Y., Lateral confinement of image electron wave function by an interfacial dipole lattice. *J. Chem. Phys.* **2003,** *118* (10), 4337-4340.

26. Steele, M. P.; Blumenfeld, M. L.; Monti, O. L. A., Image states at the interface with a dipolar organic semiconductor. *J. Chem. Phys.* **2010,** *133* (12), 124701-11.

27. Gaffney, K. J.; Miller, A. D.; Liu, S. H.; Harris, C. B., Femtosecond Dynamics of Electrons Photoinjected into Organic Semiconductors at Aromatic-Metal Interfaces. *J. Phys. Chem. B* **2001,** *105* (38), 9031-9039.

28. Velic, D.; Hotzel, A.; Wolf, M.; Ertl, G., Electronic states of the C_6H_6/Cu(111) system: Energetics, femtosecond dynamics, and adsorption morphology. *J. Chem. Phys.* **1998,** *109* (20), 9155-9165.

29. Wang, H.; Dutton, G.; Zhu, X. Y., Electronic Structure at Organic/Metal Interfaces: Naphthalene/Cu(111). *J. Phys. Chem. B* **2000,** *104* (44), 10332-10338.

30. Lobo-Checa, J.; Matena, M.; Müller, K.; Dil, J. H.; Meier, F.; Gade, L. H.; Jung, T. A.; Stöhr, M., Band Formation from Coupled Quantum Dots Formed by a Nanoporous Network on a Copper Surface. *Science* **2009,** *325* (5938), 300-303.

31. Duhm, S.; Heimel, G.; Salzmann, I.; Glowatzki, H.; Johnson, R. L.; Vollmer, A.; Rabe, J. P.; Koch, N., Orientation-dependent ionization energies and interface dipoles in ordered molecular assemblies. *Nat. Mater.* **2008,** *7* (4), 326-332.

32. Hong, S.-Y.; Yeh, P.-C.; Dadap, J. I.; Osgood, R. M., Interfacial Dipole Formation and Surface-Electron Confinement in Low-Coverage Self-Assembled Thiol Layers: Thiophenol and p-Fluorothiophenol on Cu(111). *ACS Nano* **2012,** *6* (12), 10622-10631.

33. Lingle, R. L., Jr.; Padowitz, D. F.; Jordan, R. E.; McNeill, J. D.; Harris, C. B., Two-dimensional localization of electrons at interfaces. *Phys. Rev. Lett.* **1994,** *72* (14), 2243-2246.

34. Ge, N.-H.; Wong, C. M.; Harris, C. B., Femtosecond studies of electron dynamics at interfaces. *Acc. Chem. Res.* **2000,** *33* (2), 111-118.

35. Plunkett, K. N.; Godula, K.; Nuckolls, C.; Tremblay, N.; Whalley, A. C.; Xiao, S., Expeditious Synthesis of Contorted Hexabenzocoronenes. *Org. Lett.* **2009,** *11* (11), 2225-2228.

36. Hengsberger, M.; Baumberger, F.; Neff, H. J.; Greber, T.; Osterwalder, J., Photoemission momentum mapping and wave function analysis of surface and bulk states on flat Cu(111) and stepped Cu(443) surfaces: A two-photon photoemission study. *Phys. Rev. B.* **2008,** *77* (8), 085425.

37. Steinmann, W.; Fauster, T., Laser Spectroscopy and Photochemistry on Metal Surfaces. *Advanced Series in Physical Chemistry* **1995,** *5*.

38. Bröker, B.; Hofmann, O. T.; Rangger, G. M.; Frank, P.; Blum, R. P.; Rieger, R.; Venema, L.; Vollmer, A.; Müllen, K.; Rabe, J. P.; Winkler, A.; Rudolf, P.; Zojer, E.; Koch, N., Density-Dependent Reorientation and Rehybridization of Chemisorbed Conjugated Molecules for Controlling Interface Electronic Structure. *Phys. Rev. Lett.* **2010,** *104* (24), 246805.

39. Hao, Z.; Dadap, J. I.; Knox, K. R.; Yilmaz, M. B.; Zaki, N.; Johnson, P. D.; Osgood, R. M., Nonequilibrium Band Mapping of Unoccupied Bulk States below the Vacuum Level by Two-Photon Photoemission. *Phys. Rev. Lett.* **2010,** *105* (1), 017602.

40. Ishii, H.; Sugiyama, K.; Ito, E.; Seki, K., Energy Level Alignment and Interfacial Electronic Structures at Organic/Metal and Organic/Organic Interfaces. *Adv. Mater.* **1999,** *11* (8), 605-625.

41. Crispin, X.; Geskin, V.; Crispin, A.; Cornil, J.; Lazzaroni, R.; Salaneck, W. R.; Brédas, J.-L., Characterization of the Interface Dipole at Organic/ Metal Interfaces. *J. Am. Chem. Soc.* **2002,** *124* (27), 8131-8141.

42. Terentjevs, A.; Steele, M. P.; Blumenfeld, M. L.; Ilyas, N.; Kelly, L. L.; Fabiano, E.; Monti, O. L. A.; Della Sala, F., Interfacial Electronic Structure of the Dipolar Vanadyl Naphthalocyanine on Au(111): “Push-Back” vs Dipolar Effects. *J. Phys. Chem. C* **2011,** *115* (43), 21128-21138.

43. Bauert, T.; Zoppi, L.; Koller, G.; Garcia, A.; Baldridge, K. K.; Ernst, K.-H., Large Induced Interface Dipole Moments without Charge Transfer: Buckybowls on Metal Surfaces. *J. Phys. Chem. Lett.* **2011,** *2* (21), 2805-2809.

44. Vázquez, H.; Flores, F.; Kahn, A., Induced Density of States model for weakly-interacting organic semiconductor interfaces. *Org. Electron.* **2007,** *8* (2–3), 241-248.

45. Vazquez, H.; Dappe, Y. J.; Ortega, J.; Flores, F., Energy level alignment at metal/organic semiconductor interfaces: ``Pillow" effect, induced density of interface states, and charge neutrality level. *J. Chem. Phys.* **2007,** *126* (14), 144703-8.

46. Vázquez, H.; Oszwaldowski, R.; Pou, P.; Ortega, J.; Pérez, R.; Flores, F.; Kahn, A., Dipole formation at metal/PTCDA interfaces: Role of the Charge Neutrality Level. *EPL (Europhysics Letters)* **2004,** *65* (6), 802.

47. Wolf, M.; Knoesel, E.; Hertel, T., Ultrafast dynamics of electrons in image-potential states on clean and Xe-covered Cu (111). *Phys. Rev. B* **1996,** *54* (8), R5295.

48. Wong, C. M.; McNeill, J. D.; Gaffney, K. J.; Ge, N. H.; Miller, A. D.; Liu, S. H.; Harris, C. B., Femtosecond studies of electron dynamics at dielectric-metal interfaces. *J. Phys. Chem. B* **1998,** *103* (2), 282-292.

49. Niesner, D.; Fauster, T.; Dadap, J. I.; Zaki, N.; Knox, K. R.; Yeh, P. C.; Bhandari, R.; Osgood, R. M.; Petrović, M.; Kralj, M., Trapping surface electrons on graphene layers and islands. *Phys. Rev. B* **2012,** *85* (8), 081402.

50. Güdde, J.; Höfer, U., Femtosecond time-resolved studies of image-potential states at surfaces and interfaces of rare-gas adlayers. *Prog. Surf. Sci.* **2005,** *80* (3–4), 49-91.

51. Johns, J. E.; Muller, E. A.; Frechet, J. M. J.; Harris, C. B., The Origin of Charge Localization Observed in Organic Photovoltaic Materials. *J. Am. Chem. Soc.* **2010,** *132* (44), 15720-15725.

Supporting Information

Identification of Monolayer Coverage of HBC on Cu(111)

In order to identify the monolayer coverage, we first prepared a multilayer HBC film on Cu by evaporating HBC onto the substrate in sufficient time. The sample was heated to a predetermined temperature. After cooling the sample to 300K, TPPE spectra were measured to identify any change of work function or in other known features. If there was no change in the TPPE spectrum, we increased the heating temperature and repeated the heating-cooling-measurement cycle. When a significant change in the TPPE spectra was observed, this same thermal cycle was repeated numerous times so as to achieve a longer effective heating or annealing time and thus complete any desorption at this temperature; see Fig. 5.8. In this way, we found a specific temperature range to selectively desorb the weakly-bound HBC molecules from the sample. Since the desorption temperature of a monolayer is distinct and generally higher than the multilayer for organic adsorbates on metal surfaces[1-4], the molecular film remaining after this thermal desorption process was defined as 1ML coverage of HBC. By measuring the work function of this 1ML film of HBC/Cu(111), we then had a probe to determine the dosing time for depositing 1ML HBC coverage. The dosing times for other coverages, including 2ML, are determined based on the assumption that the coverage of HBC is linearly proportional to the deposition time. The change of slope in the work function as a function of coverage (inset of Fig. 5.2) agrees with this estimation.

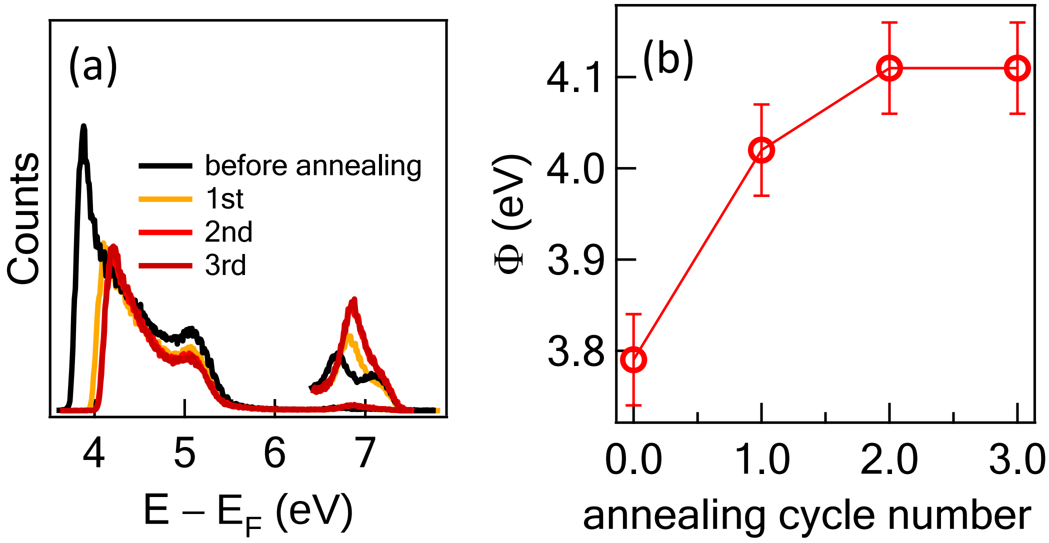

Figure 5.8 (a) A series of TPPE spectra with E_h = 3.64 eV before and after annealing cycles for 2ML HBC/Cu(111). The temperature and time for each annealing cycle was 270 ± 20˚C and 50 min, respectively, (b) The work function *versus* the number of annealing cycle for 2ML HBC/Cu(111).

Dependence of State B on the Polarization of Incident Light

In order to identify the nature of the symmetry of state B, TPPE spectra were collected using two different polarizations of incident beams: p- and s-polarizations. It was found that state B was only detected TPPE spectra when the incident laser beam had p-polarization. This result indicates that state B is a state possessing σ–symmetry, such as is seen typically for an image potential state of copper surfaces.

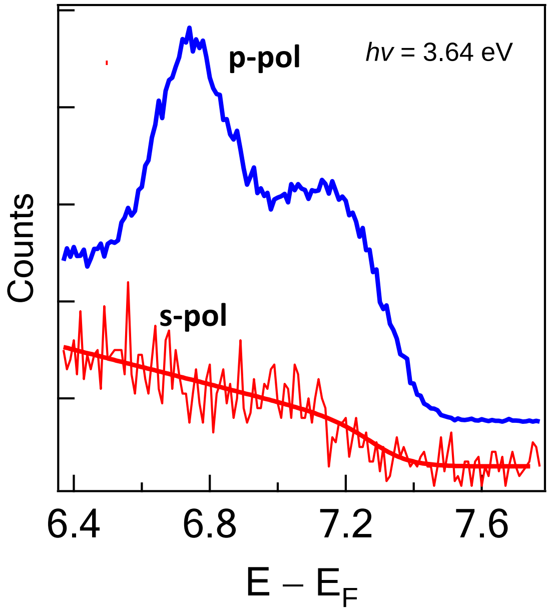

Figure 5.9 TPPE spectra of 2 ML HBC/Cu(111) around state B with $E_{h\nu}$ = 3.64 using p- and s-polarized incident beams.

Examination of Annealing Effect on the State A

The TPPE spectra of 0.3ML HBC/Cu(111) was examined before and after 20 min 150 ˚C annealing of the molecular film. After this procedure, no measurable change of either the work function or TPPE spectrum was observed. These results suggest that the states seen for this film, such as state A, do not originate from defect states of the HBC film.

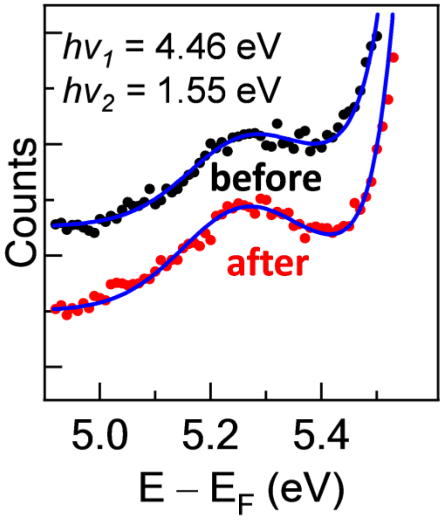

Figure 5.10 TPPE spectra of 0.3ML HBC/Cu(111) around state A with $E_{h\nu,\, pump}$ = 4.46 eV and $E_{h\nu,\, probe}$ = 1.55 eV before and after annealing at 150 ˚C for 20 min.

Examination of Annealing Effect on the State B

In addition, the TPPE spectrum of 2ML HBC/Cu(111) was examined before and after annealing. There was no measurable change of either work function or TPPE spectrum, again indicating the HBC film is lacks defect states and thus these are not likely the origin of state B.

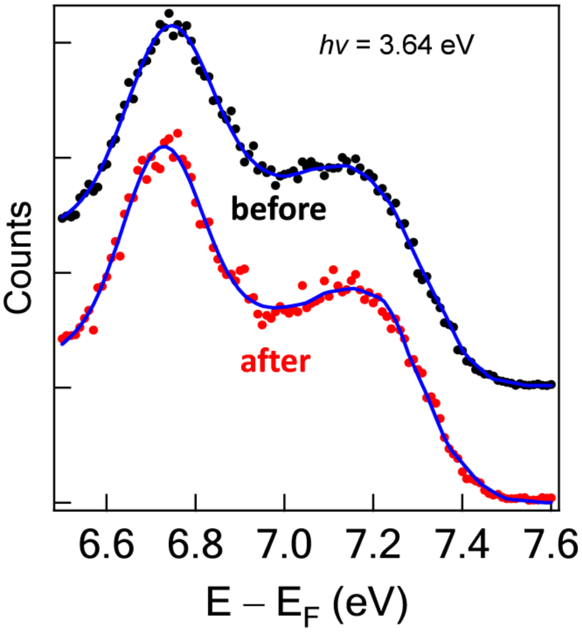

Figure 5.11 (a) TPPE spectra of 2 ML HBC/Cu(111) around state B with $E_{h\nu}$ = 3.64 before and after annealing at 190 ˚C for 50 min.

References of Supporting Materials

1. Käfer, D. and G. Witte, *Evolution of pentacene films on Ag(111): Growth beyond the first monolayer. Chem. Phys. Lett*., 2007, 442, 376-383.

2. Kilian, L., E. Umbach, and M. Sokolowski, *Molecular beam epitaxy of organic films investigated by high resolution low energy electron diffraction (SPA-LEED): 3,4,9,10-perylenetetracarboxylicacid-dianhydride (PTCDA) on Ag(111). Surf. Sci.*, 2004. 573, 359-378.

3. Schuerlein, T.J., et al., *Large Molecule Epitaxy on Single Crystal Metals, Insulators and Single Crystal and MBE-Grown Layered Semiconductors. Jap. J. App. Phys.* 34, 3837

4. Söhnchen, S., et al., *Molecular Beam Deposition of Perylene on Copper: Formation of Ordered Phases. Chem. Mater., 2005.* ***17,*** *5297-5304.*

Chapter 6

Optical Third-Harmonic Generation of Graphene

We report strong third-harmonic generation (THG) in monolayer graphene grown by chemical vapor deposition (CVD) and transferred to an amorphous silica (glass) substrate; the photon energy is in three-photon resonance with the exciton-shifted van Hove singularity at the *M*-point of graphene. The polarization selection rules are derived and experimentally verified. In addition, our polarization- and azimuthal-rotation-dependent THG measurements reveal in-plane isotropy as well as an in-plane/out-of-plane anisotropy of the nonlinear optical response of graphene. Since the third-harmonic signal exceeds that from bulk glass by more than two orders of magnitude, the signal contrast permits background-free scanning of graphene and provides insight into the structural properties of graphene.

6.1 Introduction

Single-layer graphene has become a subject of intense interest and study because of its remarkable electronic, optical, mechanical, and thermal properties, combined with its unique electronic band structure[1–4]. Despite its monolayer-to-few-layer thickness, graphene offers an array of properties that are of interest for optical physics and devices. These properties include relatively flat optical absorption from around 0.5 to 1.5 eV, with a strong doping dependent absorption edge and pronounced excitonic effects[5–9]; coupling of optical and mechanical properties in graphene membranes[10]; and plasmonic properties[11,12]. Such studies have underscored the importance of the linear optical properties of graphene[5–9,13–15]. In addition, measurements of optical carrier generation in graphene have led to the observation of strong hot-electron photoluminescence as well as new scattering phenomena involving highly excited carriers[16–18].

Recent theoretical investigations of nonlinear optical effects arising from interband electronic transitions have revealed that, despite graphene's single-atomic-layer thickness, its nonlinear optical response is particularly strong[19–21]. The potential of graphene as a functional nonlinear optical material has engendered many nonlinear optical studies. Second-order-nonlinear optical effects, particularly second-harmonic generation (SHG), have been investigated theoretically[22–25] and experimentally[22,26]. Because ideal freestanding monolayer graphene is centrosymmetric, its second-order nonlinear response vanishes within the dipole approximation[24]. In contrast, symmetry-allowed third-order nonlinear optical effects in graphene are remarkably strong, leading to studies that include saturable absorption[27–32], optical limiting[33,34], two-photon absorption[35], four-wave mixing (FWM)[36,37], and current-induced SHG[38]. In one notable FWM investigation, the authors have estimated the third-order nonlinear susceptibility of single-layer and multilayer graphene and demonstrated the capability of FWM for imaging of graphene using two input beams[36].

Third-harmonic generation (THG) is a third-order nonlinear process that provides three key advantages over FWM: (1) It can be carried out with a single-wavelength source, in contrast to the two-beam method of FWM; (2) for graphene, there is negligible hot-electronluminescence background (generated by the fundamental wave) at the much larger photon energy of the thirdharmonic (TH) output wave relative to that of the input wave; and (3) for typical sources, THG has a potential for imaging with higher transverse resolution, because of its shorter output wavelength and cubic power dependence, than is possible with FWM or with the linear optical process of the same fundamental frequency. THG has also been demonstrated as a scanned-microscopy probe of interfaces with axial resolution of the order of the confocal parameter[39].

A recent study experimentally demonstrated THG from graphene for transitions occurring near the *K* point and was carried out at normal-incidence angle; in that study, the authors report a quadratic dependence of THG on graphene layer number[40]. In contrast, the present work reports experimental THG from graphene under conditions in which the TH is in three-photon resonance with the *M* point of graphene and at non-normal-incidence angle in order to provide access to other nonlinear susceptibility elements not accessible under a normal-incidence configuration, and to probe thicker films, in the case of multilayer graphene. In addition, we present a theoretical description of THG in graphene by considering the nonlinear slab geometry. We derive the polarization selection rules by taking into account the full symmetry of the tensor properties of graphene and the layer-number dependence of the TH, and compare these properties with experiment. Our theoretical calculations predict subquadratic dependence on layer number in direct quantitative agreement with our experiment. Finally, we demonstrate the first imaging of discrete graphene crystals by THG.

Thus, our goal is twofold: to characterize the TH nonlinear optical response of graphene near its *M* saddle point and to examine the potential of THG as an optical probe and imaging approach for graphene. Our study has yielded important physics insights in THG from graphene, including the following: (1) the isotropy of the in-plane nonlinear optical response, (2) anisotropy between the out-of-plane and in-plane nonlinear optical responses, and (3) the coherent nature of THG, which gives rise to an approximately subquadratic layer dependence of the THG signal at low layer numbers. In addition, the strong TH signals from graphene on amorphous silica glass (SiO_2) provide high contrast between graphene and glass, thereby permitting nearly background-free imaging of graphene islands, which uncovers thin-film structure that is difficult to observe via linear optical microscopy. Furthermore, the use of THG allows a broader choice of substrates than for typical optical imaging of graphene using certain fixed-thickness oxide layers on Si(001) to facilitate optical contrast[41]. This capability to probe graphene on arbitrary substrates is an important advantage of THG over linear optical imaging since graphene has been transferred to various substrates, including silicon-on-insulator[37], sapphire[42], diamondlike carbon[43], hexagonal boron nitride[44], quartz and glass[45], and flexible polymer substrates[46–49], for photonic and electronic applications.

6.2 Theoretical Consideration

We begin our description of the nonlinear optical response of graphene by considering the nonlinear optical process in a slab geometry for the two cases of the harmonic field perpendicular and parallel to the incidence plane (*s*- and *p*-polarized cases, respectively) as previously derived by Bloembergen and Pershan in their classic paper[50]. Specifically, we derive the linear and nonlinear optical fields arising from a nonlinear slab on a semi-infinite substrate. The extension of the model to the case with a finite substrate is straightforward but will be more complex, as has been considered in SHG from multilayers[51].

The simpler case of semi-infinite substrate, in which multiple reflections within the substrate are absent, is justified, since the coherence length of the fundamental beam, $\lambda^2/(n\Delta\lambda)\approx$ 21 m, is much less than the substrate thickness, typically around 1 mm (as in our case). Figure 1 shows the optical geometry with the relevant fields and polarization. The nonlinear optical parameters are denoted by F_i, where $F = E$ (electric field), H (magnetic intensity), K (nonlinear optical wave vector), or θ (wave vector angle relative to surface normal direction), and $i = \{R, M, M', T\}$, indicating the reflected, internal downward going, internal upward going, and transmitted fields, respectively. In addition, the nonlinear polarization P^{NL}, which is the complex amplitude of $\mathbf{P}^{\mathrm{NL}}$, is referred with the inhomogeneous wave vector $\mathbf{K}_S = 3\mathbf{k}$, where $\mathbf{k}$ is the downward going linear wave vector in the slab; $\mathbf{K}_S$ is directed at the angle θ_S relative to the surface normal. The magnitude of the component parallel to the surface of each of the nonlinear wave vectors is equal to $K_{||} \equiv K_{R,||}$ (generalized Snell's law). The dielectric constants in the reflection, medium, and transmission regions are given by ε_R, ε_M, and ε_T, respectively, at the nonlinear optical frequency, Ω, which we will set later to 3ω for the case of THG. Note that the dielectric constant associated with the nonlinear polarization, $\varepsilon_S = \varepsilon_S(\omega)$, is evaluated at the fundamental frequency.

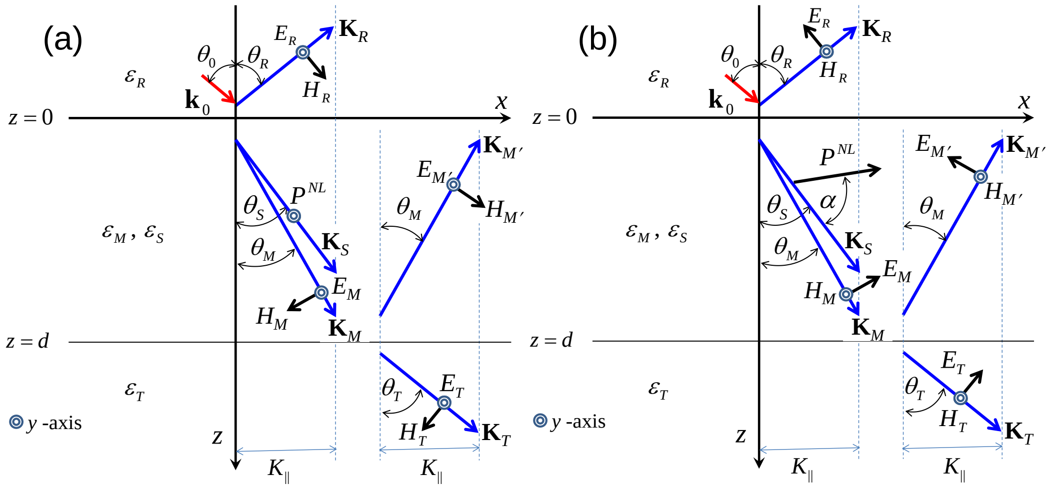

Figure 6.1 Geometry of harmonic generation in a slab of nonlinear material for (a) *s* and (b) *p* polarizations. The fundamental wave vector $\mathbf{k}_0$ is shown for reference.

For each of the perpendicular and parallel-polarization configurations, a set of four linear equations is solved by applying the appropriate boundary conditions, as previously derived by Bloembergen and Pershan[50]. The relevant results are the expressions for the reflected harmonic field, E_R, for *s* and *p*-polarized cases, which are correspondingly given by[50]

$$E_R^{\perp}=\frac{4\pi P_{\perp}^{\mathrm{NL}}\left[\begin{array}{l}A(n_T\cos\theta_T-n_S\cos\theta_S)n_M\cos\theta_M-\\B(n_Sn_T\cos\theta_S\cos\theta_T-n_M^2\cos^2\theta_M)\end{array}\right]}{(n_M^2-n_S^2)\left[\begin{array}{l}\exp(2i\phi_M)(n_R\cos\theta_R-n_M\cos\theta_M)(n_T\cos\theta_T-n_M\cos\theta_M)-\\(n_R\cos\theta_R+n_M\cos\theta_M)(n_T\cos\theta_T+n_M\cos\theta_M)\end{array}\right]},\tag{6.1a}$$

$$E_R^{\parallel}=\frac{4\pi P_{\parallel}^{\mathrm{NL}}\left\{\begin{array}{l}\left[\begin{array}{l}A(n_S\cos\theta_T-n_T\cos\theta_S)n_M\cos\theta_M-\\B(n_M^2\cos\theta_T\cos\theta_S-n_Tn_S\cos^2\theta_M)\end{array}\right]n_M\sin\alpha-\\\left[An_T\cos\theta_M+Bn_M\cos\theta_T\right](n_M^2-n_S^2)\sin\theta_S\cos\alpha\end{array}\right\}}{n_M(n_M^2-n_S^2)\left[\begin{array}{l}\exp(2i\phi_M)(n_M\cos\theta_R-n_R\cos\theta_M)(n_M\cos\theta_T-n_T\cos\theta_M)-\\(n_M\cos\theta_R+n_R\cos\theta_M)(n_M\cos\theta_T+n_T\cos\theta_M)\end{array}\right]}\tag{6.1b}$$

with phase terms

$$A = 1 + \exp(2i\phi_M) - 2\exp[i(\phi_M + \phi_S)]$$
$$B = 1 - \exp(2i\phi_M) \tag{6.1c}$$

where the relevant parameters are defined as $\phi_M = n_M \Omega d / c$, $\phi_S = n_S \Omega d / c$, $n_R = \varepsilon_R^{1/2}(\Omega)$, $n_M = \varepsilon_M^{1/2}(\Omega)$, and $n_S = \varepsilon_S^{1/2}(\omega)$.

We now consider the complex amplitudes $P_\perp^{\mathrm{NL}}$ and $P_\parallel^{\mathrm{NL}}$ for the case of THG in Eq. 6.1a and 6.1b, which determine the components of the nonlinear optical polarization $\mathbf{P}^{\mathrm{NL}}$ according to Fig. 1 via the relations $P_{\mathrm{x}}^{\mathrm{NL}} = P_\parallel^{\mathrm{NL}} \sin(\theta_s + \alpha)$, $P_y^{\mathrm{NL}} = P_\perp^{\mathrm{NL}}$, and $P_{\mathrm{z}}^{\mathrm{NL}} = P_\parallel^{\mathrm{NL}} \cos(\theta_s + \alpha)$. Monolayer graphene possesses D_{6h} (6/*mmm*) symmetry; however, when supported on the surface of a glass substrate, graphene loses its inversion symmetry along the surface normal, thus giving rise to C_{6v} (6*mm*) symmetry. For either D_{6h} or C_{6v} symmetry, there are 21 nonzero $\chi^{(3)}$ elements, of which only 10 are independent[52]; the Cartesian components $P_i^{\mathrm{NL}} = \sum_j \sum_k \sum_l \chi_{ijkl}^{(3)} E_j E_k E_l$ ({*i*,*j*,*k*,*l*} = {*x*,*y*,*z*}) of $\mathbf{P}^{\mathrm{NL}}$, with the graphene surface along the *xy* plane, may be written as

$$P_{\{x,y\}}^{\mathrm{NL}} = \chi_1 (\mathbf{E}\cdot\mathbf{E}) E_{\{x,y\}} + (\chi_1' - \chi_1) E_{\{x,y\}} E_z^2 \tag{6.2a}$$

$$P_z^{\mathrm{NL}} = \chi_3' (\mathbf{E}\cdot\mathbf{E}) E_z + (\chi_3 - \chi_3') E_z^3 \tag{6.2b}$$

where four effective susceptibilities $\chi_1 \equiv \chi_{xxxx}^{(3)} = \chi_{xxyy}^{(3)} + \chi_{xyxy}^{(3)} + \chi_{xyyx}^{(3)}$, $\chi_1' \equiv \chi_{xxzz}^{(3)} + \chi_{xzxz}^{(3)} + \chi_{xzzx}^{(3)}$, $\chi_3 \equiv \chi_{zzzz}^{(3)}$, and $\chi_3' \equiv \chi_{zzxx}^{(3)} + \chi_{zxzx}^{(3)} + \chi_{zxxz}^{(3)}$ are expressed in terms of the ten independent susceptibility elements (note that terms whose *x* and *y* indices are interchanged, are equal, e.g., $\chi_{xxxx}^{(3)} = \chi_{yyyy}^{(3)}$, $\chi_{xxyy}^{(3)} = \chi_{yyxx}^{(3)}$, etc.); E_i is the component of the downward going electric-field amplitude **E** of the fundamental beam inside the medium. In principle, one needs to use both downward (**E**) and upward (**E′**) going *fundamental* waves in the slab. In the prescription of Bloembergen and Pershan, however, when |*E*| > |*E′*|, the nonlinear polarization constructed solely on the downward going field inside the slab (corresponding to E) will approximate the correct result[50]; this case is satisfied in graphene due to its low linear reflectance.

As we will show experimentally below, the use of a circularly polarized input beam yields no TH signals and, consequently, second terms vanish in Eq. 2(a)-(b) since $\mathbf{E}\cdot\mathbf{E}=0$ yielding $\chi_1=\chi_1'$ and $\chi_3=\chi_3'$. These conditions lead to the following relations: $\chi^{(3)}_{xxxx}=\chi^{(3)}_{xxyy}+\chi^{(3)}_{xyxy}+\chi^{(3)}_{xyyx}$ = $\chi^{(3)}_{xxzz}+\chi^{(3)}_{xzxz}+\chi^{(3)}_{xzzx}$ and $\chi^{(3)}_{zzzz}=\chi^{(3)}_{zzxx}+\chi^{(3)}_{zxzx}+\chi^{(3)}_{zxxz}$, and reduce the number of independent tensor elements from 10 to 8. Thus the polarization can now be written simply as

$$P_i^{\mathrm{NL}}=\chi_i\,(\mathbf{E}\cdot\mathbf{E})E_i \tag{6.3}$$

where $\chi_i=\{\chi_1,\chi_1,\chi_3\}$ for $i=\{x,y,z\}$. Eq. 6.3 implies that there are now two effective TH susceptibilities as a consequence of vanishing circular-polarized-input TH signals. These 2 effective susceptibilities correspond to an in-plane isotropic response associated with $\chi_1\equiv\chi^{(3)}_{xxxx}$ and an out-of-plane response associated with $\chi_3\equiv\chi^{(3)}_{zzzz}$. Eq. 6.3 also predicts that purely *p*- or *s*-polarized pump input beams produce purely *p*- or *s*-polarized TH beams, respectively, i.e., *p*-in/*p*-out and *s*-in/*s*-out signals are allowed, while *p*-in/*s*-out and *s*-in/*p*-out together with the circular-in/(s or p)-out polarization configurations are forbidden.

The graphene band structure further simplifies the values of the nonlinear susceptibility elements. Since, in our case, the relevant conduction and valence bands of graphene are formed from π orbitals of carbon atoms, the matrix elements associated with the resonant downward 3ω transitions are dominated by an in-plane (*x* or *y*) polarization corresponding to the leading index of the susceptibility tensor. The left inset in Fig. 6.2(a) shows the energy-band diagram and a schematic three-photon transition process for the conditions of our experiment. In this diagram, the exciton-shifted energy gap at the *M*-point is 4.6 eV[7-9], which is approximately three-photon resonant with our fundamental photon energy of 1.57 eV. In addition, near the *M*-point, the usual linear graphene dispersion curve flattens and thus the density of states is high due to the van Hove singularity at the saddle point, thereby enhancing the graphene nonlinear optical susceptibility via the transition matrix elements and the resonance in its denominator term. Transitions associated with the *z*-polarization are possible only with the σ orbitals, in which the energy separation is much larger than those of the π orbitals at the *M*-point by several electron volts[24]. Thus for the three upward virtual ω transitions followed by the downward resonant 3ω transition in the vicinity of the *M*-point, $|\chi^{(3)}_{xxxx}| >> |\chi^{(3)}_{zzzz}|$, and the remaining susceptibility terms that involve the index *z* are negligible. The number of independent elements is further reduced from 8 to 3 but only 1 effective tensor element, i.e., χ_1 , now remains. Thus we may set $\chi_i \approx \{\chi_1, \chi_1, 0\}$ in Eq. 6.3. Since our transition occurs in the vicinity of the *M*-point, we anticipate that it would involve significant excitonic effects as seen recently in single-photon transitions in this same region of *k*-space[7-9]. As a result, it would be useful to examine this transition using full band-structure calculations of the nonlinear susceptibilities, in the presence of many-body effects.

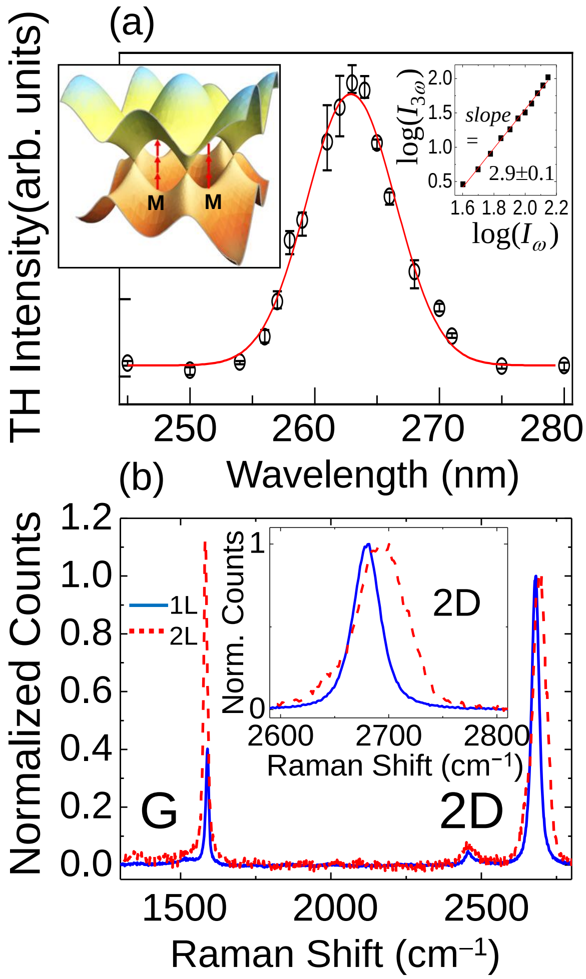

Figure 6.2 (a) THG spectrum along with a right inset log-log plot showing a cubic power dependence of the TH signal intensity $I_{3\omega}$ with respect to the intensity of the fundamental beam, I_ω. The left inset shows the electronic band structure of graphene including a 3-photon resonance at the exciton-shifted graphene M saddle-point. (b) The Raman spectra in the monolayer (1L) and bilayer (2L) regions of the graphene flakes (solid and dashed, curves, respectively). The Raman signals are normalized with respect to the 2D peak.

6.3 Experiment

Single crystals of graphene were grown by chemical vapor deposition (CVD) and subsequently transferred onto glass substrates using procedures described in detail previously[53]. Briefly, graphene was grown at 1030 ℃ on 25-μm-thick copper-foil, following low-pressure, encapsulated-growth methods[54], so as to yield spatially-isolated single crystals with characteristic overall dimensions of approximately 200 μm. The graphene was subsequently transferred onto glass substrates (~1 mm thick), which had been first cleaned in a solution of sulfuric acid and hydrogen peroxide (3:1), utilizing a dry-transfer procedure with PMMA to support the graphene crystals throughout the transfer process; this procedure has been described previously in detail[53].

Our THG studies on the graphene samples used 50 fs, 789 nm pulses from a Ti:sapphire laser, which passed through a half-wave plate and polarizer and then focused onto the sample with a typical average power of 100 mW at a 60° incidence angle. The spot radii of the TH signal along its short and long dimensions are measured to be ~2.5 and 5 μm using the knife-edge technique with a gold film, corresponding to a typical fundamental beam fluence of ~ 1 mJ/cm^2. At this fluence, no degradation of the graphene during irradiation was observed, thus permitting multiple and reproducible scans of the graphene flakes with no discernible change in signal levels. For the TH measurements, the sample is mounted on a mated orthogonal-translation and rotation stage, which permitted 2D scanning as well as measurements of the rotational anisotropy of the TH signals.

The reflected THG signal was collected by a collimating lens and passed through an analyzer and then a Pellin-Broca prism to filter out the fundamental beam and a monochromator, before being detected by a photomultiplier tube. A monochromator, whose throughput was approximately 10% due to its small bandwidth window centered at the peak THG signal, was necessary to reduce background signal significantly to the level of the dark count. The conversion efficiency of the graphene/glass system is of the order of 10^{-13} relative to the input power of the fundamental beam and, hence, we used a photon-counter. The *p*-in/*p*-out photon count rates for the glass substrate after background subtraction range from 0.2 to 0.8 ± 0.5/s, which are smaller than the background (noise level) counts of approximately 1.5 ± 0.3/s. After filtering, the TH raw-signal counts from the graphene/glass system were of the order of 100 counts per second per point. This count rate implies that to scan an image from a 1 mm^2 area, it will take >10 hours to scan with 5-μm step size. If the fluence is kept fixed, improvements in signal counts at smaller spot sizes are possible through use of shorter pulse widths, normal incidence geometry, and increased repetition rates; together with high throughput spectral filters and spectral integration, we estimate that count rates > 10^4/s are possible. Thus, faster scanning times, <1 hour, are achievable, which can be reduced further using 2D-imaging systems. As a point of comparison, we carried out SHG measurements under the same laser and focusing parameters, which yielded two orders of magnitude weaker signals than that of THG.

Prior to conducting our THG measurements, Raman spectroscopy, with a 532-nm pump laser, was employed to establish the monolayer quality of our graphene. For purposes of comparison with previous Raman spectroscopic analyses of graphene, CVD graphene samples were also transferred onto Si(001) substrates with 300 nm thick thermally grown SiO_2, utilizing identical processing procedures as described above for glass substrates. Figure 6.2(b) shows Raman spectra for graphene crystals. For the all of the crystal area (solid curve) except for a 20-μm region approximately in the center of the crystal, the absence of a D peak and a 2D/G ratio greater than 2, indicated monolayer crystal of high quality. Within the central spot of a graphene flake, the 2D/G ratio is less than 1 and the 2D peak is broader compared to the monolayer case (inset) in agreement with previous Raman measurements of bilayer graphene films[55,56]. Thus, this central region contains a bilayer film, a result observed also for CVD-grown graphene on Cu foils[57]. Raman spectra were also taken on graphene flakes transferred to the silica substrate used in our THG studies, with identical results.

6.4. Results and Discussion

For our THG studies, when the fundamental beam irradiated the graphene crystal, such as shown in Fig. 6.4(b), strong nonlinear optical emission was observed. To verify the origin of the signal, we detected TH signal at multiple locations over different graphene crystals. Typical TH intensity-dependence measurements (right inset) at one location are shown in Fig. 6.2(a). The wavelength of the TH spectrum centered at 263±4 nm and its I_ω^3 power dependence fully confirm the nature of the nonlinearity of the signal. The width of the TH frequency spectrum is close to $3^{-1/2}$ of that of the fundamental beam assuming a Gaussian linewidth. Note the absence of any photoluminescence background.

To elucidate the symmetry properties of graphene with regards to its nonlinear optical response, we compared the relative magnitudes of the signals from graphene/glass to that of a glass surface using different polarization combinations, as shown in Fig. 3. For the case of the graphene/glass surface, the dominant signals arise from the *s*-in/*s*-out and *p*-in/*p*-out polarization combinations. The cross-polarized configurations as well as the circularly polarized input (*c*-in/*s*-out, *c*-in/*p*-out) data are seen to be weak relative to the dominant signals. It should be noted that in general, a circularly polarized beam may change in ellipticity as the beam enters the material. Inside the graphene layer, one needs to take into account the Fresnel transmission coefficients for each orthogonal component of the field. Using the refractive indices of graphene and the oxide substrate, we find that the change in the ratio of the magnitudes and the relative phase of the *s*- and *p*-components of the fundamental field inside the graphene layer is nearly unchanged, i.e., the field maintains its circularly polarized character. We calculate the ratio of the circularly polarized intensity signal to that of the linearly polarized case to be of the order of 10^{-6}.

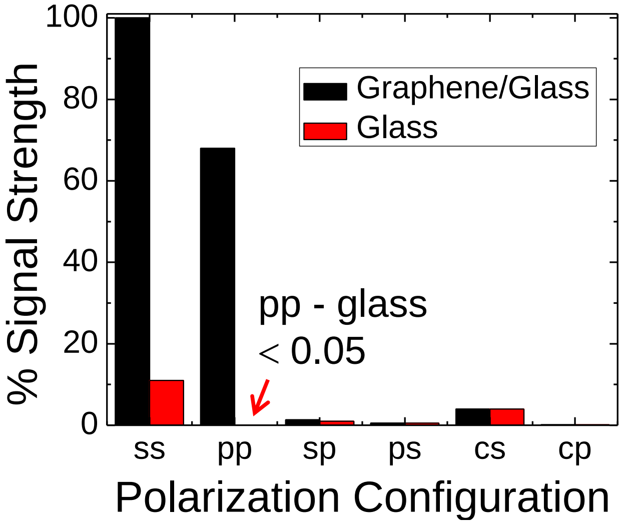

Figure 6.3 Relative signal levels at various THG polarization combinations normalized to the s-in/s-out signal levels of the graphene/glass system, which confirms the isotropic third-order nonlinear optical response of graphene.

These results clearly indicate that the expected THG polarization selection rules for the C_{6v} symmetry, as discussed above, are present. In addition, a comparison between the glass and graphene/glass signals for the *p*-in/*p*-out configuration indicates a negligible contribution from the glass substrate. This difference in signal levels between glass and graphene exceeds two orders of magnitude and hence the total signal arises essentially from the graphene monolayer. Thus the THG signals appear as arising entirely from the graphene layer for this polarization configuration. In addition for imaging purposes, we have used the *p*-in/*p*-out configuration to maximize contrast between the graphene and glass signals.

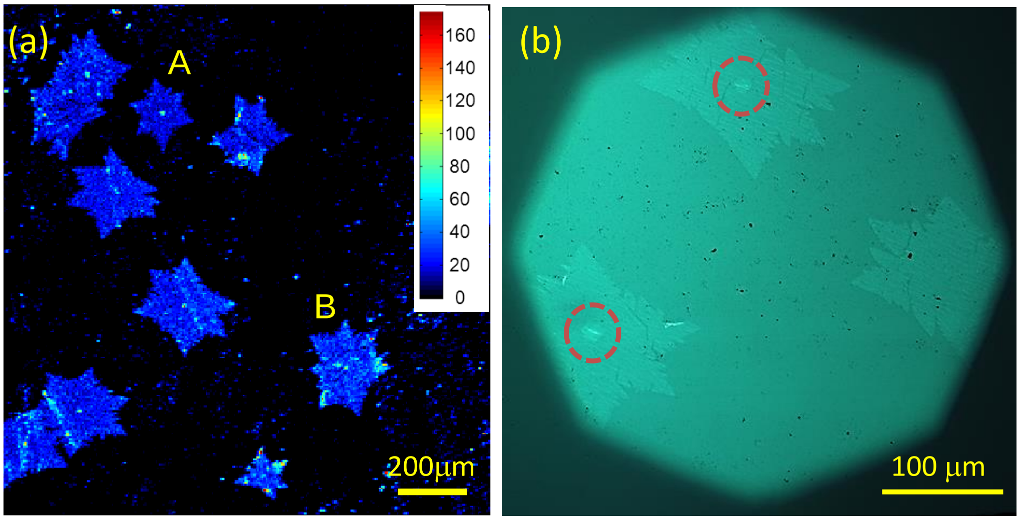

Figure 6.4 (a) THG *p*-in/*p*-out scan of a 1.4×1.4 mm^2 area featuring star-shaped CVD-grown monolayer graphene crystals on glass, which are approximately 200 µm in characteristic dimension. (b) Optical microscopy of graphene stars on glass; central bright spots (inside dashed red circles) correspond to bilayer graphene.

Additional properties of the TH generation could be established via probing of an array of similar graphene films. Figure 6.4(a) shows a scanned image, obtained from a large-area (1.4×1.4 mm^2) on a sample using the *p*-in/*p*-out configuration. The image contains randomly distributed star-shaped graphene crystals, with nearly uniform overall dimensions of approximately 200 µm. In this constellation of graphene "stars", there are clear "bright spots" in the center of most stars, which are attributed to bilayer signals from our Raman data and are approximately 20 µm in diameter; see also a magnified view of one of the stars in Fig. 6.4(a) below. These results in the central region are consistent with both optical imaging (Fig.6. 4b), in which the bilayer regions are clearly visible, and Raman measurements (Fig. 6.2b). Note also that the high-contrast TH signals from the graphene stars is further enhanced due to the absence of *p*-in/*p*-out TH signals from the glass substrate at this incidence angle.

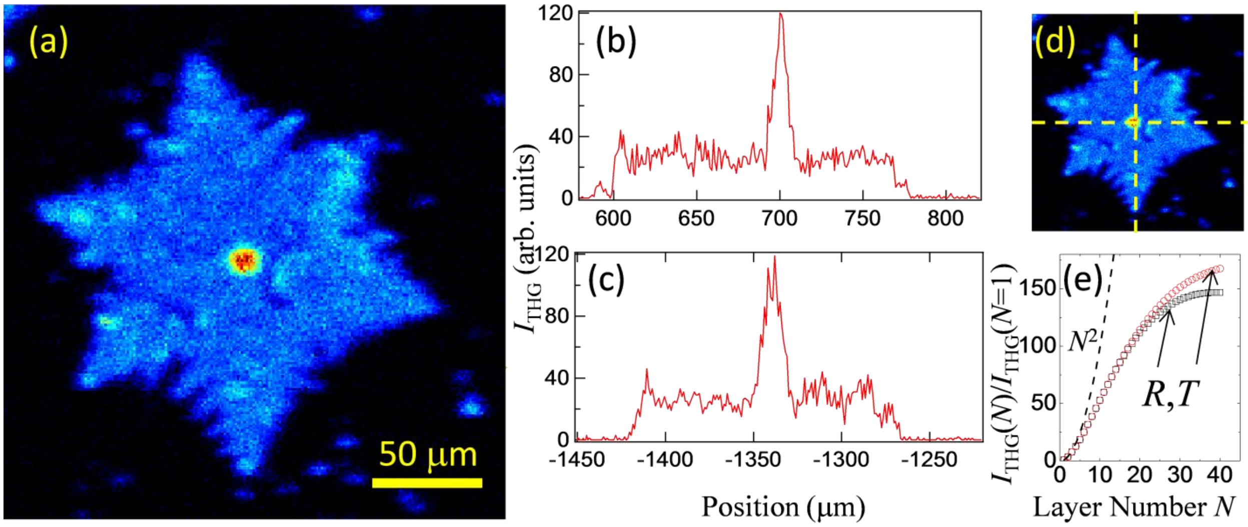

Figure 6.5 (a) TH *p*-in/*p*-out scan of graphene star "A" shown in Fig. 6.4(a); (b) and (c) are line scan data along the dashed vertical and horizontal lines that pass through the central spot as shown in (d); (e) *calculated* layer dependence of THG for reflected (*R*) and transmitted (*T*) signals normalized to monolayer signal using Eq. 6.1b; quadratic dependence is shown for reference (dashed).

A higher resolution scan of a single graphene flake, denoted by "A" in Fig. 4(a), is presented in Fig. 6.5(a) for a 240 × 240 μm^2 scanning field. The bright spot at its center enables us to quantify the dependence of the relative TH signal level as a function of layer number relative to the rest of the graphene signals. In particular, two line scans are shown in Fig. 6.5(b) and (c) corresponding to the vertical and horizontal dashed lines in Fig. 6.5(d), which pass through the central spot of this graphene flake. The peak TH signal, which is located at the central spot of this graphene star, is larger by a factor of approximately 3.8 ± 0.1 than the average signal from the remainder of the graphene crystal. As discussed above, our Raman measurements of this star on this substrate indicate that the central region has a bilayer composition. Using the reflected field from Eq. 1(b) to calculate the intensity $I \propto |E_{\parallel}^{R}|^2$ as a function of graphene layer number *N*, and making use of the optical constants of graphene at the fundamental and TH wavelengths[15], $n_{Gr}(\lambda) \approx 3+1.5i$ and $n_{Gr}(\lambda/3) \approx 2+3i$, respectively, and a slab thickness $d = 3.35N$ Å, we calculate a signal ratio of 3.7 between the bilayer and monolayer regions, in close agreement with our results. As a check, these constants are used to calculate normal-incidence reflectance and transmittance values using the *linear* optical analogue of either Eq. 1(a) or 1(b) for the case of air-graphene-air system with $n_R = n_T = 1$ at our fundamental wavelength. This calculation yields $R \approx 0$ and $T \approx 2.4N$ % ($N < 6$), respectively, as expected for multilayers of graphene and in good agreement with the measured values for suspended graphene in Ref. 5.

For comparison, the normal-reflection FWM signal for visible to near-IR pump wavelengths is given by $I_{FWM} \propto N^2/(1+N\pi\alpha/2)^8$ [36], where α is the fine-structure constant and $\pi\alpha \approx 0.023$ is the single-layer absorbance of graphene; this formula yields a ratio of $I_{FWM}(N=2)/I_{FWM}(N=1)$ = 3.7, which is similar to our measurements. Note that in the absence of absorption for the fundamental and output wavelengths, the ratio between *N*-layer and monolayer signals should be N^2 for either THG or FWM process, and hence for the case of bilayer, this ratio equals 4. For larger *N* values the effect of absorption on both input and output waves becomes stronger and consequently the THG intensity initially increases sub-quadratically with layer number up to a certain layer number where the signal reaches a maximum value, and then decreases at larger layer numbers. The layer number corresponding to the maximum signal is maximum depends on the incidence angle. Assuming that the dielectric constants are independent of layer number, we estimate that as high as ~ 40 layers can be determined with THG at the current incidence angle (see Fig. 5(e)). This number is reduced to ~20 layers under normal incidence, similar to that estimated via FWM. This general behavior is also true for the *transmitted* TH signal. With Raman imaging, however, this limit is ~10 where the signal is indistinguishable from graphite[58].

The high contrast in the TH signal, described above for Fig. 4, has important consequences for higher-resolution imaging. As a specific example, high contrast makes it particularly easy to observe certain structural features in Fig. 5(a), such as the fractal-like topographical structures, wrinkling, and depressions at the edge and internal area of the graphene star. These structures observed using THG follow similar features that are obtained using atomic force microscopy (AFM) on transferred CVD-grown graphene[59]. We are in the process of carrying out studies to correlate features observed using THG with that observed through AFM. Such structural features are also seen using optical microscopy but without the high contrast shown in Fig. 5(e); this result is due to the significantly lower contrast of linear optical microscopy. In addition, the image also shows internal structure, which is not readily apparent in linear microscopy. In particular fluctuations in the image brightness are seen in Fig. 5. Thus, we speculate that topographic variations in the graphene may cause changes in the local optical electric field, which is then magnified by the nonlinear interactions, although it is not possible to rule out the interplay of other effects such local fluctuations in doping, which varies the electronic response, or local strain. Note, in addition, that despite the use of a modest numerical aperture (NA) in our laser-beam imaging system, such spatial features are observed due to the inherent improved spatial resolution arising from the I_ω^3 dependence of the TH signal as well as the shorter TH wavelength. Further significant improvement in spatial resolution can be expected by making use of a higher NA system to enable submicrometer resolution. Another important consequence of our result is the potential use of TH imaging of graphene for arbitrary substrates beyond the now standard 300-nm-oxide/silicon substrate[41]. Such alternative substrates are currently a topic of interest brought about by new graphene/substrate combinations made possible with CVD graphene.

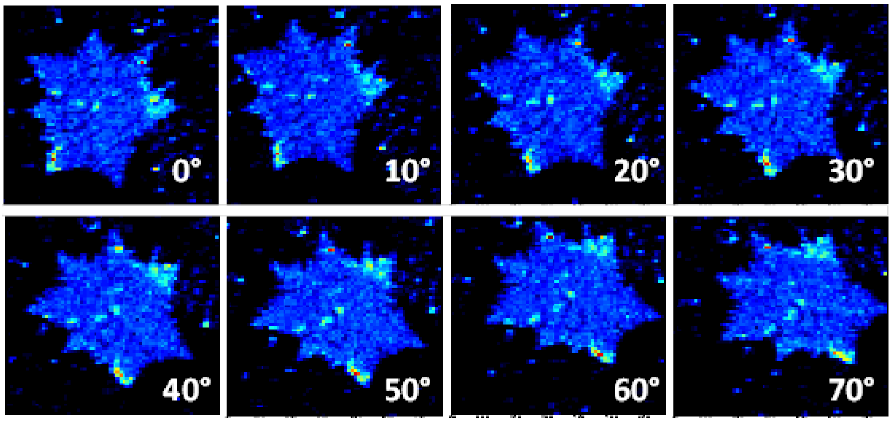

Figure 6.6 Azimuthal dependence of THG scans of the graphene star "B" shown in Fig. 4(a) indicating the isotropic nonlinear optical response of graphene.

As a final test of the in-plane isotropic nonlinear response of graphene to THG, we performed azimuthally dependent experiments by rotating the sample in the plane of the graphene. Figure 6 shows rotational scans of the graphene flake denoted as B in Fig. 4(a); each image is taken at a different azimuthal angle, spaced by increments of 10°. We chose this particular graphene flake due to the presence of bright areas of non-uniform TH signals, away from the center of the flake. These spots provide guide points to help track the rotation of the graphene flake. Note that the magnitude of the signals at an arbitrary local point within the star is generally constant to within 5% at all the angles used, indicating the isotropic response of the third-order nonlinearity of graphene. The results of these rotational measurements are consistent with the fact the signals among all the stars are relatively uniform in Fig. 4(a) despite the random angular crystallographic orientation of the stars. Finally we note that this series of scans also demonstrates the high reproducibility of THG microscopy of graphene.

In order to better quantify the relative strength of the TH signal from graphene, we also measured the corresponding TH signals from gold and other SiO_2-based substrates. Gold has also been utilized as a reference substrate in previous FWM study of graphene[36]. For our gold samples, we used a high-purity 100-μm thick gold film evaporated on a glass substrate. From our measurements and from calculations taking into account the fields within the respective media, we obtained $|\chi_{1,graphene}/\chi_{1,gold}| \sim 4.6$; we can further deduce the ratio of their nonlinearity per unit thickness as $R \equiv (|\chi_{1,graphene}|/L_{graphene})/(|\chi_{1,gold}|/L_{gold}) \sim 1.6\times10^{2}$, where the corresponding graphene and gold thicknesses were taken as $L_{graphene}$ = 0.335 nm and L_{gold} = 12 nm, respectively. Here we have taken the gold thickness as the inverse of its tabulated absorption coefficient at the TH wavelength[60]. These results show that the nonlinearity per unit thickness of graphene is particularly strong in comparison with that of gold. Previously, the ratio R was measured using FWM in the visible spectral range and away from the M-point of graphene[36]. As a comparison, our value of R, which is measured at the 3-photon resonant M-point using the THG process, is about 4 times larger than the previous FWM measurement, i.e., $R_{\mathrm{THG}}/R_{\mathrm{FWM}} \approx 4$.

For the case of SiO_2-based substrates such as crystalline quartz, fused silica, and soda-lime glass, we find that the nonlinear susceptibility $\chi_1 = \chi^{(3)}_{xxxx}$ values of these materials are within the same order of magnitude. In extracting these parameters, we made use of Eq. 1(a) and set $d = 0$

to yield $E_R^{\perp} = -4\pi P_{\perp}^{NL}(n_M \cos\theta_M - n_S \cos\theta_S)/[(n_M^2 - n_S^2)(n_R \cos\theta_R + n_M \cos\theta_M)]$. Our results show that the ratio $|\chi_{1,graphene}/\chi_{1,\mathrm{SiO_2}}|$ ranges from ~ 0.8 to 0.9 $\times 10^3$, i.e., the graphene nonlinearity is nearly three orders of magnitude larger than that of the SiO_2-based materials, which includes crystalline quartz.

6.5 Conclusion

In conclusion, we have demonstrated optical third-harmonic generation as a deterministic probe of graphene nonlinear optical properties. We have shown that despite its typical use as a probe of bulk media, THG can also be a probe of a single-atom-thick film with high discrimination due to the strong nonlinearity of graphene. The use of THG confirms the symmetry properties of graphene: Polarization-dependent and azimuthal rotation measurements reveal in-plane isotropic symmetry as well as in-plane/out-of-plane asymmetry of the nonlinear optical response in agreement with the hexagonal symmetry of graphene. These polarization-dependent measurements establish the relationships between tensor elements, which further allow us to reduce the number of independent tensor components. Together with the knowledge of band structure, the number of independent components reduces from 10 to 3 and the number of effective measurable tensor component reduces from 4 to 1, given by $\chi_{xxxx}^{(3)}$ = $\chi_{xxyy}^{(3)} + \chi_{xyxy}^{(3)} + \chi_{xyyx}^{(3)}$. The coherent nature of THG gives rise to a sub- quadratic layer dependence of the THG signal at low layer numbers. In addition, we have found that the nonlinear susceptibility $\chi_{xxxx}^{(3)}$ of graphene is nearly five times that of gold, and nearly three orders of magnitude larger than that of SiO_2-based substrates including quartz crystal, which shows the strong nonlinear optical response of the TH process for graphene, making it a potential probe for electronic processes near the exciton-shifted M point of graphene.

The in-plane isotropy, in conjunction with the coherent nature of THG, permits probing of the physical structure of graphene without crystallographic orientation dependence. THG further provides the potential for characterization of CVD-grown graphene structures on arbitrary substrates, without having to utilize high visibility contrast microscopy (i.e., not limited to SiO_2/Si substrates) and without the graphene hot-electron luminescence background as seen in other nonlinear optical studies such as FWM. Clearly, we have demonstrated that THG can be used as an optical microscopy probe of graphene even with modest optical focusing. In fact, THG has intrinsically higher spatial resolution due to the cubic intensity dependence of the nonlinear process and its shorter TH wavelength.

6.6 References

1. V. Singh, D. Joung, L. Zhai, S. Das, S. I. Khondaker, and S. Seal, "Graphene based materials: Past, present and future," Prog. Mater Sci. **56**, 1178-1271 (2011).

2. M. J. Allen, V. C. Tung, and R. B. Kaner, "Honeycomb Carbon: A Review of Graphene," Chem. Rev. **110**, 132-145 (2009).

3. S. D. Sarma, S. Adam, E. Hwang, and E. Rossi, "Electronic transport in two-dimensional graphene," Rev. Mod. Phys. **83**, 407 (2011).

4. M. S. Fuhrer, C. N. Lau, and A. H. MacDonald, "Graphene: materially better carbon," MRS Bull. **35**, 289-295 (2010).

5. R. Nair, P. Blake, A. Grigorenko, K. Novoselov, T. Booth, T. Stauber, N. Peres, and A. Geim, "Fine structure constant defines visual transparency of graphene," Science **320**, 1308-1308 (2008).

6. Z. Li, E. Henriksen, Z. Jiang, Z. Hao, M. Martin, P. Kim, H. Stormer, and D. N. Basov, "Dirac charge dynamics in graphene by infrared spectroscopy," Nat. Phys. **4**, 532-535 (2008).

7. K. F. Mak, J. Shan, and T. F. Heinz, "Seeing many-body effects in single-and few-layer graphene: Observation of two-dimensional saddle-point excitons," Phys. Rev. Lett. **106**, 46401 (2011).

8. V. Kravets, A. Grigorenko, R. Nair, P. Blake, S. Anissimova, K. Novoselov, and A. Geim, "Spectroscopic ellipsometry of graphene and an exciton-shifted van Hove peak in absorption," Phys. Rev. B **81**, 155413 (2010).

9. L. Yang, J. Deslippe, C.-H. Park, M. L. Cohen, and S. G. Louie, “Excitonic Effects on the Optical Response of Graphene and Bilayer Graphene,” Phys. Rev. Lett. **103**, 186802 (2009)

10. R. A. Barton, I. Storch, V. P. Adiga, R. Sakakibara, B. R. Cipriany, R. Ilic, S. P. Wang, P. Ong, P. L. McEuen, and J. M. Parpia, "Photothermal Self-Oscillation and Laser Cooling of Graphene Optomechanical Systems," Nano Lett. **12**, 4681-4686 (2012).

11. L. Ju, B. Geng, J. Horng, C. Girit, M. Martin, Z. Hao, H. A. Bechtel, X. Liang, A. Zettl, and Y. R. Shen, "Graphene plasmonics for tunable terahertz metamaterials," Nat. Nanotechnol. **6**, 630-634 (2011).

12. H. Yan, X. Li, B. Chandra, G. Tulevski, Y. Wu, M. Freitag, W. Zhu, P. Avouris, and F. Xia, "Tunable infrared plasmonic devices using graphene/insulator stacks," Nat. Nanotechnol. **7**, 330-334 (2012).

13. M. Bruna and S. Borini, "Optical constants of graphene layers in the visible range," Appl. Phys. Lett. **94**, 031901 **94**, 031901 (2009).

14. J. Weber, V. Calado, and M. Van de Sanden, "Optical constants of graphene measured by spectroscopic ellipsometry," Appl. Phys. Lett. **97**, 091904 (2010).

15. A. Matković, U. Ralević, G. Isić, M. Jakovljević, B. Vasić, I. Milošević, D. Marković, and R. Gajić, "Spectroscopic ellipsometry and the Fano resonance modeling of graphene optical parameters," Phys. Scr. **2012**, 014069 (2012).

16. C. H. Lui, K. F. Mak, J. Shan, and T. F. Heinz, "Ultrafast photoluminescence from graphene," Phys. Rev. Lett. **105**, 127404 (2010).

17. R. J. Stöhr, R. Kolesov, J. Pflaum, and J. Wrachtrup, "Fluorescence of laser-created electron-hole plasma in graphene," Phys. Rev. B **82**, 121408 (2010).

18. W.-T. Liu, S. Wu, P. Schuck, M. Salmeron, Y. Shen, and F. Wang, "Nonlinear broadband photoluminescence of graphene induced by femtosecond laser irradiation," Phys. Rev. B **82**, 81408 (2010).

19. K. L. Ishikawa, "Nonlinear optical response of graphene in time domain," Phys. Rev. B **82**, 201402 (2010).

20. S. Jafari, "Nonlinear optical response in gapped graphene," J. Phys.: Condens. Matter **24**, 205802 (2012).

21. H. Avetissian, A. Avetissian, G. Mkrtchian, and K. V. Sedrakian, "Creation of particle-hole superposition states in graphene at multiphoton resonant excitation by laser radiation," Phys. Rev. B **85**, 115443 (2012).

22. J. J. Dean and H. M. van Driel, "Graphene and few-layer graphite probed by second-harmonic generation: Theory and experiment," Phys. Rev. B **82**, 125411 (2010).

23. S. Mikhailov, "Theory of the giant plasmon-enhanced second-harmonic generation in graphene and semiconductor two-dimensional electron systems," Phys. Rev. B **84**, 045432 (2011).

24. M. Glazov, "Second harmonic generation in graphene," JETP letters **93**, 366-371 (2011).

25. S. Wu, L. Mao, A. M. Jones, W. Yao, C. Zhang, and X. Xu, "Quantum-Enhanced Tunable Second-Order Optical Nonlinearity in Bilayer Graphene," Nano Lett. **12**, 2032-2036 (2012).

26. J. J. Dean and H. M. van Driel, "Second harmonic generation from graphene and graphitic films," Appl. Phys. Lett. **95**, 261910 (2009).

27. Q. Bao, H. Zhang, Y. Wang, Z. Ni, Y. Yan, Z. X. Shen, K. P. Loh, and D. Y. Tang, "Atomic-Layer Graphene as a Saturable Absorber for Ultrafast Pulsed Lasers," Adv. Funct. Mater. **19**, 3077-3083 (2009).

28. W. B. Cho, J. W. Kim, H. W. Lee, S. Bae, B. H. Hong, S. Y. Choi, I. H. Baek, K. Kim, D.-I. Yeom, and F. Rotermund, "High-quality, large-area monolayer graphene for efficient bulk laser mode-locking near 1.25 μm," Opt. Lett. **36**, 4089-4091 (2011).

29. D. Popa, Z. Sun, F. Torrisi, T. Hasan, F. Wang, and A. Ferrari, "Sub 200 fs pulse generation from a graphene mode-locked fiber laser," Appl. Phys. Lett. **97**, 203106 (2010).

30. Y.-W. Song, S.-Y. Jang, W.-S. Han, and M.-K. Bae, "Graphene mode-lockers for fiber lasers functioned with evanescent field interaction," Appl. Phys. Lett. **96**, 051122 (2010).

31. W. Tan, C. Su, R. Knize, G. Xie, L. Li, and D. Tang, "Mode locking of ceramic Nd: yttrium aluminum garnet with graphene as a saturable absorber," Appl. Phys. Lett. **96**, 031106 (2010).

32. J.-L. Xu, X.-L. Li, Y.-Z. Wu, X.-P. Hao, J.-L. He, and K.-J. Yang, "Graphene saturable absorber mirror for ultra-fast-pulse solid-state laser," Opt. Lett. **36**, 1948-1950 (2011).

33. J. Wang, Y. Hernandez, M. Lotya, J. N. Coleman, and W. J. Blau, "Broadband nonlinear optical response of graphene dispersions," Adv. Mater. **21**, 2430-2435 (2009).

34. M. Feng, H. Zhan, and Y. Chen, "Nonlinear optical and optical limiting properties of graphene families," Appl. Phys. Lett. **96**, 033107 (2010).

35. H. Yang, X. Feng, Q. Wang, H. Huang, W. Chen, A. T. Wee, and W. Ji, "Giant Two-Photon Absorption in Bilayer Graphene," Nano Lett. **11**, 2622-2627 (2011).

36. E. Hendry, P. Hale, J. Moger, A. Savchenko, and S. Mikhailov, "Coherent nonlinear optical response of graphene," Phys. Rev. Lett. **105**, 97401 (2010).

37. T. Gu, N. Petrone, J. McMillan, A. van der Zande, M. Yu, G.-Q. Lo, D.-L. Kwong, J. Hone, and C. W. Wong, "Regenerative oscillation and four-wave mixing in graphene optoelectronics," Nat. Photonics **6**, 554–559 (2012).

38. A. Y. Bykov, T. V. Murzina, M. G. Rybin, and E. D. Obraztsova, "Second harmonic generation in multilayer graphene induced by direct electric current," Phys. Rev. B **85**, 121413 (2012).

39. Y. Barad, H. Eisenberg, M. Horowitz, and Y. Silberberg, "Nonlinear scanning laser microscopy by third harmonic generation," Appl. Phys. Lett. **70**, 922-924 (1997).

40. N. Kumar, J. Kumar, C. Gerstenkorn, R. Wang, H.-Y. Chiu, A. L. Smirl, and H. Zhao, “Third harmonic generation in graphene and few-layer graphite films,” Phys. Rev. B 87, 121406(R) (2013).

41. P. Blake, E. Hill, A. Castro Neto, K. Novoselov, D. Jiang, R. Yang, T. Booth, and A. Geim, "Making graphene visible," Appl. Phys. Lett. **91**, 063124 (2007).

42. M. A. Fanton, J. A. Robinson, C. Puls, Y. Liu, M. J. Hollander, B. E. Weiland, M. LaBella, K. Trumbull, R. Kasarda, C. Howsare, J. Stitt, and D. W. Snyder, “Characterization of Graphene Films and Transistors Grown on Sapphire by Metal-Free Chemical Vapor Deposition,” *ACS Nano* **5**, 8062–8069 (2011) .

43. Y. Wu, Y.-M. Lin, A. A. Bol, K. A. Jenkins, F. Xia, D. B. Farmer, Y. Zhu, and P. Avouris, “High-frequency, scaled graphene transistors on diamond-like carbon, Nature, vol. 472, 74-78 (2011).

44. C. R. Dean, A. F. Young, I. Meric, C. Lee, L. Wang, S. Sorgenfrei, K. Watanabe, T. Taniguchi, P. Kim, K. L. Shepard, and J. Hone, "Boron nitride substrates for high quality graphene electronics," Nat. Nanotechnol. 5, 722-726 (2010)

45. X. Li, Y. Zhu, W. Cai, M. Borysiak, B. Han, D. Chen, R. D. Piner, L. Colombo, and R. S. Ruoff, “Transfer of Large-Area Graphene Films for High-Performance Transparent Conductive Electrodes” *Nano Lett.*, 9, 4359–4363 (2009)

46. Jongho Lee, Li Tao, Yufeng Hao, Rodney S. Ruoff, and Deji Akinwande Embedded-gate graphene transistors for high-mobility detachable flexible Nanoelectronics, Appl. Phys. Lett. 100, 152104 (2012)

47. N. Petrone, I. Meric, J. Hone, and K. L. Shepard, “Graphene Field-Effect Transistors with Gigahertz-Frequency Power Gain on Flexible Substrates,” Nano Lett. 13, 121−125, (2013).

48. S. Bae, H. Kim, Y. Lee, X. Xu, J.-S. Park, Y. Zheng, J. Balakrishnan, T. Lei, H. R.Kim, Y. I. Song, Y.-J. Kim, K. S. Kim, B. Özyilmaz, J.-H. Ahn, B. H. Hong and S. Iijima, “Roll-to-

roll production of 30-inch graphene films for transparent electrodes," Nature Nanotechnology 5, 574–578 (2010).

49. S.-K. Lee, B. J. Kim, H. Jang, S. C. Yoon, C. Lee , B. H. Hong , J. A. Rogers, J. H. Cho, and J.-H. Ahn, "Stretchable Graphene Transistors with Printed Dielectrics and Gate Electrodes," Nano Lett., 11, 4642–4646 (2011).

50. N. Bloembergen and P. Pershan, "Light waves at the boundary of nonlinear media," Phys. Rev. **128**, 606 (1962).

51. K. Pedersen and T. G. Pedersen, "Spectroscopic second-harmonic generation from silicon-on-insulator wafers," J. Opt. Soc. Am. B **26**, 917-922 (2009).

52. Robert Boyd, *Nonlinear Optics*, 3rd ed. (Academic, New York, 2008); p. 54.

53. N. Petrone, C. R. Dean, I. Meric, A. M. van der Zande, P. Y. Huang, L. Wang, D. Muller, K. L. Shepard, and J. Hone, "Chemical Vapor Deposition-Derived Graphene with Electrical Performance of Exfoliated Graphene," Nano Lett. **12**, 2751-2756 (2012).

54. X. Li, C. W. Magnuson, A. Venugopal, R. M. Tromp, J. B. Hannon, E. M. Vogel, L. Colombo, and R. S. Ruoff, "Large-area graphene single crystals grown by low-pressure chemical vapor deposition of methane on copper," J. Am. Chem. Soc. **133**, 2816 (2011)

55. A. Ferrari, J. Meyer, V. Scardaci, C. Casiraghi, M. Lazzeri, F. Mauri, S. Piscanec, D. Jiang, K. Novoselov, and S. Roth, "Raman spectrum of graphene and graphene layers," Phys. Rev. Lett. **97**, 187401 (2006).

56. C. H. Lui, Z. Li, Z. Chen, P. V. Klimov, L. E. Brus, and T. F. Heinz, "Imaging Stacking Order in Few-Layer Graphene," Nano Lett. **11**, 164-169 (2010).

57. S. Nie, W. Wu, S. Xing, Q. Yu, J. Bao, S.-S. Pei, and K. F. McCarty, "Growth from below: bilayer graphene on copper by chemical vapor deposition," New J. Phys. **14**, 093028 (2012).

58. A. C. Ferrari, "Raman spectroscopy of graphene and graphite: Disorder, electron–phonon coupling, doping and nonadiabatic effects," Solid State Communications **143**, 47–57 (2007).

59. W. Zhu, T. Low, V. Perebeinos, A. A. Bol, Y. Zhu, H. Yan, J. Tersoff, and P. Avouris, "Structure and electronic transport in graphene wrinkles," Nano Lett. **12**, 3431-3436 (2012).

60. P. B. Johnson and R. Christy, "Optical constants of the noble metals," Phys. Rev. B **6**, 4370 (1972).

Chapter 7

Summary and Future Directions

7.1 Summary

Thin-film technology based on inorganic materials has been used in a wide range of application including optical coating, semiconductor electronic devices, and surface protection. Recent progress in organic film and newly-developed two dimensional materials has shown a strong potential to revolutionize the current technologies. However, the technological revolution requires the solid understanding of physical and chemical processes in the materials. For this dissertation, the electronic structure and nonlinear optical properties of three different ultrathin film systems were investigated using muti-photon spectroscopic techniques.

The two systems investigated in this dissertation are categorized into molecule/metal interfaces. In order to study their interfacial electronic structures, two-photon photoemission experiments were carried out. The multi-photon ionization nature of this technique allows probing of both occupied and unoccupied states. With this photoemission probe, we studied surface states including the Shockley state and the image potential states in the presence of molecular adsorbates. In addition, the shift in the work function as a function of coverage was investigated.

In order to study molecule/metal interfaces, we needed to deposit molecules on a metal surface with a precise control. A UHV-compatible molecular gas doser was built to deposit a low-vapor-pressure molecules, thiophenol and *p*-fluorothiophenol. An organic evaporator was also built to deposit an organic semiconductor material, hexa-*cata*-hexabenzocoronene (HBC).

These instruments facilitated the study of the effect of molecular coverage on the interfacial electronic structure. All the TPPE experiments were conducted under UHV conditions.

Thiophenol and *p*-fluorothiophenol are simple aromatic thiols, which can form a self-assembled monolayer (SAM) on a noble metal. The substitution of para-position with an electronegative element (*e.g.*, fluorine) in thiophenol made a significant difference in the intrinsic dipole moment. Our coverage-dependent TPPE measurements for both thiol species revealed how the orientation of molecule and its intrinsic dipole play a role in surface polarization and how molecular assemblies cause quantum confinement of surface electrons.

HBC is a non-planar organic semiconductor material, which has been studied for photovoltaic applications. We used TPPE to investigate the interfacial electronic structure of HBC on Cu(111) as a function of coverage. Based on our polarization- and momentum-resolved TPPE, we concluded that the porous structure of HBC film causes a strong localization of image electrons at 0-1ML coverage. The local film structure transformed from porous to smooth by increasing the HBC coverage. As a result, a highly dispersive image state on 2ML HBC islands became predominant.

The third system we investigated in this dissertation is graphene on glass substrate. Graphene is a single sheet of sp_2-bonded carbons with excellent optical and electrical properties. Based on the broad-band resonance and full π-conjugation, the strong nonlinear optical response of graphene was expected.

In order to investigate the third order nonlinear optical properties of graphene, we built nonlinear optical scanning microscope and developed a software program to fully automate the function of scanning and data collection. With the precise control of polarization and sample orientation, this microscope facilitated high-quality THG imaging of graphene and characterization of its anisotropy.

Our analysis of THG signals were based on Bloembergen's nonlinear optics theory. Our theoretical prediction agreed very well with the experimental results. The THG of a monolayer graphene showed in-plane isotropy and out-of-plane anisotropy. The coherent nature of THG gave near-quadratic dependence of THG signals on the layer number of graphene which were observed in our experiments. However, more accurate treatment based on the nonlinear optical slab model showed a large deviation from a quadratic dependence at thicker graphene film. We also observed that the third harmonic susceptibility of graphene is more than 2 order of magnitude stronger than that of SiO_2-type materials.

7.2 Future Directions

Although each system was thoroughly investigated by TPPE and THG techniques, our understanding is still far from the complete. For thiophenol and *p*-fluorothiophenol studies, unoccupied electronic states were neither fully characterized nor understood. Our preliminary data showed that the n=1 image state survived when the Cu substrate was fully covered by face-down thiols. However, its effective mass and binding energy were not characterized. Also for the unoccupied electronic structure of a fully monolayer, thiophenol and *p*-fluorothiophenol showed a marked difference. Thus future studies should include clarification of the effects of fluorine substitution on the interfacial electronic structure. One suggestion is to carry out TPPE studies on thiols on other substrates such as Au and Ag as well as with other tail groups on thiol such as Cl and Br.

Better understanding of HBC interfaces would be possible with the structural characterization of 1-2ML HBC/Cu(111) using surface diffraction techniques and STM. The previous STM studies of HBC/Cu(111) was limited to sub-monolayer coverage and the data of monolayer and multilayer structures are missing. In addition, TPPE studies on other similar organic semiconductors such as hexa-*peri*-hexabenzocoronene (flat-HBC) or other coronene-type molecules would be necessary to understand the effect of the contorted geometry of HBC on the interfacial electronic structure.

For THG studies of graphene, the in-plane symmetry of bi- and multi-layer graphene has not been clarified in this dissertation. Although a monolayer of graphene has a six-fold symmetry, multilayer graphene may have a different symmetry. Our preliminary second harmonic generation (SHG) studies showed a three-fold symmetry from multilayer graphene samples. A similar anisotropy could be observed for the THG measurements. In addition, it would be valuable to study THG of graphene with a series of different wavelengths of fundamental light. From the band structure of graphene, strong wavelength dependence of THG intensity was predicted.